

**WCDMA CAPACITY ANALYSIS FOR MIXED DATA
SERVICES USING MRC AND IRC SMART ANTENNAS**

by

PATRICK SHANG-NENG WU

Bachelor of Applied Science, University of British Columbia, 1999

**A THESIS SUBMITTED IN PARTIAL FULFILLMENT OF
THE REQUIREMENTS FOR THE DEGREE OF
MASTER OF APPLIED SCIENCE**

in

**THE FACULTY OF GRADUATE STUDIES
DEPARTMENT OF ELECTRICAL AND COMPUTER ENGINEERING**

**We accept this thesis as conforming
to the required standard**

The University of British Columbia

April 2004

©Patrick Shang-Neng Wu, 2004

Library Authorization

In presenting this thesis in partial fulfillment of the requirements for an advanced degree at the University of British Columbia, I agree that the Library shall make it freely available for reference and study. I further agree that permission for extensive copying of this thesis for scholarly purposes may be granted by the head of my department or by his or her representatives. It is understood that copying or publication of this thesis for financial gain shall not be allowed without my written permission.

PATRICK SHANG-NENG WU

Name of Author (please print)

April 23, 2004

Date (dd/mm/yyyy)

Title of Thesis: WCDMA CAPACITY ANALYSIS FOR
MIXED DATA SERVICES USING MRC AND
IRC SMART ANTENNAS

Degree: MASTER OF APPLIED SCIENCE Year: 2004

Department of ELECTRICAL AND COMPUTER ENGINEERING
The University of British Columbia
Vancouver, BC Canada

Abstract

In this thesis, the effects of the Maximum Ratio Combining (MRC) and Interference Rejection Combining (IRC) smart antennas on the capacity of the 3rd Generation (3G) Wideband Code Division Multiple Access (WCDMA) cellular systems are investigated. By exploiting the signal characteristics in the spatial dimension, the MRC and IRC antennas are designed to receive signals in selective directions and reduce interferences in certain areas respectively. When these smart antennas are used along with the Rake receiver that extracts the useful information of signals in the temporal domain and the WCDMA technology, the system capacity can be increased significantly.

In order to estimate and compare the system capacity improvements these techniques offer, a software platform was designed to simulate the interference limited uplink direction of a WCDMA system at the chip level. In this simulation platform, the logical channel structure of the WCDMA air interface and a flexible antenna model that can be easily configured were implemented in detail to accurately obtain capacity results. In addition, realistic system conditions were emulated by considering practical channel models, a multiple-cell configuration, the user voice activity factor and tight power control.

Based on the simulated results, the advantages of using the IRC antennas, as compared to the MRC antennas, are presented in terms of improvements in system capacities. It is shown that the MRC and IRC smart antennas have their own advantages under different multipath channel environments. Furthermore, the performance evaluation results have indicated that turbo codes provide the most significant improvement over the convolutional codes when used for the high rate multimedia users.

The relationship between the numbers of low rate and high rate users a system can accommodate concurrently is also established from the results.

Table of Contents

Abstract	ii
List of Tables	viii
List of Figures	ix
List of Abbreviations	xi
List of Symbols	xiv
Acknowledgement	xx
Chapter 1 INTRODUCTION	1
1.1 The Evolution of Wireless Communication Systems	1
1.2 Advancements in the Antenna Systems	2
1.3 Past Research in 3G System Capacities and the Main Contributions of this Thesis.....	4
1.4 Organization of this Thesis	6
Chapter 2 TRANSPORT NETWORK AND PHYSICAL LAYERS OF WCDMA	9
2.1 Introduction	9
2.2 Transport Channels and Channel Coding Operations of the Transport Network Layer	10
2.2.1 Transport Channel Types	10
2.2.2 Convolutional Encoding and Decoding	11
2.2.3 Turbo Encoding and Decoding	13
2.2.3.1 Turbo Code Encoder	13
2.2.3.2 Turbo Code Iterative Decoder	15
2.3 Spreading and Scrambling Codes at the Physical Layer	18

2.3.1	Spread Spectrum Technique in WCDMA Systems	19
2.3.2	Spreading Codes at the Physical Layer	20
2.3.3	Scrambling Codes at the Physical Layer	24
2.4	Transmission Path Overview	26
2.4.1	Transmission Path Model	26
2.4.2	A Numerical Example of the Multi-rate Services	29
2.5	Conclusions	30
Chapter 3	THE CELLULAR STRUCTURE AND TRANSMISSION CHANNEL MODELLING	31
3.1	Introduction	31
3.2	The Cellular Concept	32
3.3	Large Scale Propagation Models	33
3.3.1	Scattering Model	33
3.3.2	Outdoor Propagation PL – Extended Hata Model	35
3.4	Small Scale Propagation Models	37
3.4.1	Fading Due to Time Dispersion	37
3.4.2	Fading Due to Frequency Dispersion	38
3.5	Frequency Selective, Slow Fading Channel Model with PL	39
3.5.1	Frequency Selective, Hashemi Radio Propagation Model	40
3.5.2	Slow Rayleigh Fading Model.....	43
3.5.3	Tapped-Delay-Line Channel Model	44
3.6	Conclusions	46
Chapter 4	ANTENNA STRUCTURES AND TECHNOLOGIES	47
4.1	Introduction	47

4.2	Fundamental Antenna Concepts	47
4.3	Spatial and Temporal Processing Concepts	49
4.3.1	Antenna Arrays and Wave Fronts Arrivals	50
4.3.2	Antenna Patterns of Linear Antenna Arrays	53
4.3.3	Temporal Processing with Rake Receivers and Two Dimensional Receivers.....	56
4.4	Smart Antennas Technologies	58
4.4.1	Weight Vector Assignment	58
4.4.2	Equal Gain Combining and Maximal Ratio Combining Antennas.....	60
4.4.3	Inference Rejection Combining Antennas.....	63
4.4.4	Parameter Estimation for MRC and IRC Demodulators	65
4.5	Conclusions	68
Chapter 5	THE WCDMA SYSTEM SIMULATOR	69
5.1	Introduction	69
5.2	The Overall Uplink Path Modeling	69
5.2.1	Uplink Transmitter Model	69
5.2.2	Uplink Transmission Channel Model	71
5.2.3	Uplink Receiver Model	74
5.3	System Methodology	77
5.3.1	Pre-run Setup Stage	78
5.3.2	Power Control	79
5.3.3	Capacity Simulation Run	83
5.4	Conclusions	86

Chapter 6	UPLINK WCDMA CAPACITY SIMULATION RESULTS AND DISCUSSIONS	87
6.1	Introduction	87
6.2	Computer Simulation Methodologies and Simulation Parameters	88
6.3	Single Path Results	89
6.4	Multipath Results	98
6.5	Further Discussions and Comparisons with Other Publications	108
6.6	Conclusions	113
Chapter 7	CONCLUSIONS AND RECOMMENDATIONS	115
7.1	Conclusions	115
7.1.1	Analysis of the MRC and IRC Smart Antennas Performances	115
7.1.2	Investigation of the Mixed Data Traffic Scenarios	116
7.1.3	System Capacity Analysis and Comparisons	117
7.2	Recommendations for Further Work.....	117
Bibliography	121

List of Tables

Table 6.1	System Parameter Values Assumed in Capacity Simulations	89
Table 6.2	Simulation Results in Figure 6.1 and the Average Cell Capacity	91
Table 6.3	Simulation Results in Figure 6.2 and the Average Cell Capacity	93
Table 6.4	Turbo Code Improvement over Convolutional Code with Varied Traffic Mixes	93
Table 6.5	Simulation Results in Figure 6.3 and the Average Cell Capacity	95
Table 6.6	4-element Array Improvement over 2-element Array with Varied Traffic Mixes	95
Table 6.7	Simulation Results in Figure 6.4 and the Average Cell Capacity	97
Table 6.8	Simulation Results in Figure 6.6 and the Average Cell Capacity	100
Table 6.9	Simulation Results in Figure 6.7 and the Average Cell Capacity	101
Table 6.10	Simulation Results in Figure 6.8 and the Average Cell Capacity	103
Table 6.11	Simulation Results in Figure 6.9 and the Average Cell Capacity	104
Table 6.12	5-finger Performance Gain over the 3-finger Case	104
Table 6.13	Simulation Results in Figure 6.10 and the Average Cell Capacity	107
Table 6.14	IRC Antenna Performance Gain over MRC Antenna	111

List of Figures

Figure 2.1	Convolutional Encoder with $r_{conv} = 1/3$ and $K_{conv} = 9$	12
Figure 2.2	A Typical Turbo Code Encoder with Two RSC's	13
Figure 2.3	Configuration of the RSC Generator with $(G_1, G_2) = (31, 27)$	14
Figure 2.4	Iterative Turbo Code Decoder with Two MAP Decoders	17
Figure 2.5	An OVSF Code Tree with 3 Layers Shown	21
Figure 2.6	The Algorithm for Generating an OVSF Code Tree	22
Figure 2.7	A Sample of OVSF Code Assignment Based on Orthogonality	22
Figure 2.8	The Scrambling Code Generator	26
Figure 2.9	A Path Model Showing the Data Operations	27
Figure 2.10	QPSK Modulations for the Complex-valued Signals	28
Figure 3.1	Geometrically Based Circular Model	35
Figure 3.2	Impulse Response of a Multipath Power Profile	43
Figure 3.3	Tapped-delay-line Model with K Taps	46
Figure 4.1	(a) Configuration and (b) Antenna Pattern of a Half Wave Dipole Antenna	49
Figure 4.2	A Linear Equally Spaced Array of M Elements Receiving a Plane of Wave Fronts from Direction $\theta_k(t)$	52
Figure 4.3	Antenna Patterns of Antenna Arrays with (a) 4 Antenna Elements Spaced at $\lambda/2$ apart, (b) 4 Antenna Elements Spaced at λ apart, (c) 7 Antenna Elements Spaced at $\lambda/2$ apart, and (d) 7 Electronically Steered Antenna Elements Spaced at $\lambda/2$ apart.....	55
Figure 4.4	An One Element Tapped Delay Line Rake Receiver Model	57
Figure 4.5	A 2D $M \times Y$ Antenna Array Model with Weight Assignments	60
Figure 5.1	Encoding and Modulating Process before Transmission	70

Figure 5.2	The 2D Receiver Model with Signal Processors	74
Figure 5.3	Data Formation Processes	76
Figure 5.4	Structure of the 3-tier, 19-cell System	78
Figure 5.5	Capacity Simulation Flow Diagram	85
Figure 6.1	Uplink Capacity Results of a Single Path System with the Convolutional Encoder, and a 2-element MRC Omnidirectional Antenna Array	90
Figure 6.2	Uplink Capacity Results of a Single Path System with the Turbo Encoder, and a 2-element MRC Omnidirectional Antenna Array	92
Figure 6.3	Uplink Capacity Results of a Single Path System with the Turbo Encoder, and a 4-element MRC Omnidirectional Antenna Array	94
Figure 6.4	Capacity Results for an All Multimedia Traffic User Single Path System with a 2, 4, and 6 - element MRC Smart Antenna Array, and the Turbo Encoding Algorithm	96
Figure 6.5	Simulation Results from Tables 6.2 and 6.3 with Different Percentages of Traffic Mix, Presented as Multimedia Users VS Voice Users Per Cell	97
Figure 6.6	Uplink Capacity Results of a Multipath Residential Berkeley System with the Turbo Encoder and 3-finger MRC Smart Antenna	99
Figure 6.7	Uplink Capacity Results of a Multipath Downtown Oakland System with the Turbo encoder and 2-element 4-finger MRC Smart Antenna	101
Figure 6.8	Uplink Capacity Results of a Multipath Downtown San Francisco System with the Turbo Encoder and 2-element 3-finger MRC Smart Antenna ..	102
Figure 6.9	Uplink Capacity Results of a Multipath Downtown San Francisco System with the Turbo Encoder and 2-element 5-finger MRC Smart Antenna ..	103
Figure 6.10	Uplink Capacity Results of a Multipath Downtown San Francisco System with the Turbo Encoder and 2-element 5-finger IRC Smart Antenna ...	106
Figure 6.11	Simulation Results from Tables 6.8, 6.9, 6.11 and 6.13 with Different Traffic Mixes, Presented as Multimedia VS Voice Users Per Cell	108

List of Abbreviations

2D	2 Dimensional
3D	3 Dimensional
2G	2 nd Generation
3G	3 rd Generation
4G	4 th Generation
3GPP	3G Partnership Project
AMPS	Advanced Mobile Phone Services
AOA	Angle of Arrival
ARQ	Automatic Repeat Request
AWGN	Additive White Gaussian Noise
BER	Bit Error Rate
BPSK	Binary Phase Shift Keying
BS	Base Station
CDF	Cumulative Probability Density
CDMA	Code Division Multiple Access
COST	Co-operative for Scientific and Technical
CRC	Cyclic Redundancy Code
D1, D2	Turbo Decoder Number 1 and 2
DCH	Dedicated Channel
DPDCH	Dedicated Physical Data Channel
DPCCH	Dedicated Physical Control Channel
FDMA	Frequency Division Multiple Access
FIR	Finite Impulse Response

GBCM	Geometrically Based Circular Model
GSM	Global System for Mobile Communications
ISI	Inter-symbol Interference
IRC	Interference Rejection Combining
JTACS	Japanese Total Access Communication System
LLR	Log Likelihood Ratio
LOS	Line of Sight
MAI	Multiple Access Interference
MAP	Maximum A Posteriori
ML	Maximum Likelihood
MRC	Maximum Ratio Combining
MS	Mobile Station
OVSF	Orthogonal Variable Spreading Factor
PDF	Probability Density Function
PG	Processing Gain
PL	Path Loss
PN	Pseudo Noise
QOS	Quality of Service
QPSK	Quarternary Phase-Shift Keying
RF	Radio Frequency
RSC	Recursive Systematic Encoder
SDMA	Spatial Division Multiple Access
SF	Spread Factor
SINR	Signal to Interference Plus Noise Ratio

SNR	Signal to Noise Ratio
SSMA	Spread Spectrum Multiple Access
TACS	Total Access Communication System
TDMA	Time Division Multiple Access
TTI	Transmission Time Interval
WCDMA	Wideband Code Division Multiple Access
W-OFDM	Wideband Orthogonal Frequency Division Multiplexing

List of Symbols

r_{conv}	Convolutional Encoder Rate
K_{conv}	Convolutional Encoder Constraint Length
N_{data}	Raw Data Bit Length
G_n	Generator Sequence for the Channel Encoder
v	Received Sequence to Be Decoded by the Channel Decoder
u_k	Channel Decoder Output
x_s	Input to the Turbo Encoder
x_p	Outputs of the Turbo Encoder
$\Lambda(\alpha)$	A Posteriori LLR
s_k	Decoder State
$\frac{E_c}{N_o}$	SNR Per Channel Bit
$C_{ch,SF,k}$	Spreading Code Set Identification Number
$C_{long,n}$	Scrambling Code Set Identification Number
$Z_n(i)$	Binary Gold Sequence for Generating Scrambling Codes
N_c	Number of Cells in a Cluster
g_c	Number of Frequency Channels Assigned to Each Cell
Q_c	Total Number of Channels Available for the System

M_c	Number of Clusters Replicated to Cover the Entire System
C_{sys}	Capacity of the System
P_t	Power Level of a Transmitting Antenna
d_{txrx}	Distance Separating the Transmitting and Receiving Antennas
G_t	Transmitting Antenna Gain
P_r	Received Power at the Receiving Antenna
G_r	Receiving Antenna Gain
L_{path}	Path Loss
r_s	Scattering Circle Radius
f_c	Carrier Frequency
h_{te}	Effective Transmitting Antenna Height
h_{re}	Effective Receiving Antenna Height
$q(h_{re})$	Correction Factor for the Receiving Antenna Height
C_M	Correction Factor for City Sizes
f_d	Doppler Shift
c_l	Speed of Light
T_{coh}	Coherence Time
θ_d	Angle between Transmitter and Receiver

v_{MS}	MS Velocity
ψ_{A_i}	Probability of Path Occurrences with an Empirical Path Occurrence Probability
P_{A_i}	Probability of Having a Path Arrival in Bin i
r_{ocr_i}	Empirical Path Occurrence Probability for Bin i
k, K	Label for the k^{th} Multipath Component, Total Number of Resolvable Multipath Components
P_{level_k}	Power Level of the k^{th} Multipath Component
a_{k+z_b}	Amplitude of the Path Arrival of Each Bin
θ_{k+z_b}	Phase of the Path Arrival of Each Bin
Z_b	Total Number of Bins in Each Multipath Component
$\tau_k(t)$	Path Delay in Chips
$h(t)$	Impulse Response of the Hashemi Multipath Model
σ	Rms Value of the Received Signal
σ^2	Time Average Power of the Received Signal
r_e	Signal Envelope Amplitude
$p_{\text{Rayleigh, Gaussian, uniform}}$	PDF of Rayleigh, Gaussian, and Uniform Distribution
β	Random Rayleigh Fading Envelope
$s(t)$	The Original Transmitted Bit before Channel Modulation

$r_{m,k}(t)$	Radio Channel Output by the FIR Filter at the m^{th} Antenna Element from the k^{th} Multipath Component
$\mathbf{N}(t)$	AWGN
$\phi_k(t)$	Rayleigh Fading Phase
$L_k(t)$	Overall Channel Impulse Response due to PL, Multipath Fading, and Rayleigh Fading for the k^{th} Multipath Component
$a_k(t)$	Overall Amplitude of the k^{th} Multipath Component
$e^{j\phi_k}$	Overall Phase of the k^{th} Multipath Component
T_{chip}	One Chip Duration
A_r	Effective Aperture of an Antenna
λ	Wavelength of the Transmitted Signal
Θ_B	-3dB Width of the Antenna Pattern
D_{ant}	Antenna Diameter
m, M	Label for the m^{th} Antenna Element, Total Number of Antenna Elements in an Antenna Array
$FR_{m,k}(t)$	Wave Front of the k^{th} Multipath Component in the Frequency Band Intercepted by the m^{th} Antenna Element of the Antenna Array
$\eta_{m,k}(t)$	Relative Signal Phase Encountered by the m^{th} Antenna Element from the k^{th} Multipath Component
$d_{m,k}$	Distance between the m^{th} Antenna Element and the Wave Front Encroaching Element 0 for the k^{th} Multipath Component

y, Y	Label for the y^{th} Rake Finger, Total Number of Rake Fingers in an Antenna Element
\mathbf{w}_y	Weight Vector for the y^{th} Finger
z_y	Sum of the Weighted Signals of the y^{th} Finger
\mathbf{H}	Hermitian Transpose
\mathbf{u}_y	Additive Multiple Access Interferences from Other Users and Self-ISI Plus Noise
\mathbf{R}_{rr_y}	Spatial Covariance Matrix
$E[\cdot]$	Statistical Expectation
$\text{diag}(\cdot)$	Diagonal Matrix
$LH(\mathbf{r}, s)$	Log Likelihood Function
$\det[\cdot]$	Determinant of a Matrix
$\hat{\mathbf{R}}_{uu}$	Estimate of \mathbf{R}_{uu}
$\hat{\mathbf{L}}$	Estimate of \mathbf{L}
$\hat{\mathbf{X}}_{sr}$	Cross Correlation Function between the Antenna Signal Vector $\mathbf{r}(b)$ and the Pilot Signals $\mathbf{s}(b)$
$\ell_1^{(n)}(t), \ell_Q^{(n)}(t)$	Output after the Transport Channel Coding, Spreading, and Scrambling Operations
$g_r(t)$	Impulse Response of the Pulse Shaping Filter
P_{tx}	Average Transmitted Power

E_b	Bit Energy
T_b	Bit Duration
n, N	Label for the n^{th} Mobile Phone User, Total Number of Users in the System
$DS_{1m,y}^{(x)}(t)$	In-phase Component of the Desired Signal
$US_{1m,y}^{(x)}(t)$	In-phase Component of the Undesired Self-interference
$UM_{1m,y}^{(x)}(t)$	In-phase Component of the Undesired MAI
I_o	Interference Power Density
$\Delta Gain$	Difference in Processing Gain
P_{t-m}	Transmitting Power for the Multimedia Group
$N_{result}(x)$	Number of Capacity Results Less than or Equal to x
N_{Total}	Total Number of Simulation Runs
I_o / N_o	Total Interference Power with Respect to the Power Spectral Density of Thermal Noise
SF_m	Spread Factor for the Multimedia User Group
SF_v	Spread Factor for the Voice User Group

Acknowledgement

I would like to take this moment to thank my supervisor Professor P. Takis Mathiopoulos for his continuous technical guidance and support throughout my research. The research work done by Mr. D. Chiu and Mr. L. Chan on the IS-95 system has benefited my research, so I would like to express my appreciation towards them. Last and most importantly, I have received tremendous encouragement and backing from my family that have allowed me to concentrate on my work. I am grateful to my parents and my siblings for their endless cheers, and to my beloved wife for all the joy and the wonderful moments she has brought me.

Chapter 1 INTRODUCTION

1.1 The Evolution of Wireless Communication Systems

For the past 30 years, cellular telecommunication systems have evolved tremendously, utilizing different multiple access techniques to allow the limited transmitting radio spectrum to be shared among users. The traditional multiple access techniques include the Frequency Division Multiple Access (FDMA) and Time Division Multiple Access (TDMA) [1][2]. As their names suggest, the users of a FDMA system are differentiated by transmission frequencies whereas a TDMA system by transmission time slots. The emergence of the Spread Spectrum Multiple Access (SSMA) makes happen the idea of transmitting signals at a transmission bandwidth that is several magnitudes greater than the dedicated Radio Frequency (RF) bandwidth [3]. Wireless systems can be categorized into several different generations based on the multiple access techniques, the signal representations, and the bandwidth for transmission employed in the systems.

The first generation analog systems in the mid 1980's, such as the American Advanced Mobile Phone Services (AMPS), the European Total Access Communication System (TACS), and the Japanese Total Access Communication System (JTACS), employed the FDMA method that assigned users different frequency channels to accommodate their subscribers [4]. When the number of mobile phone users soared as the technology became affordable to the general public, the traditional means of shrinking cell size and adding cell sites used to increase the system capacity could not keep up with the rate of increase of the number of their customers anymore. Therefore, the 2nd

Generation (2G) systems that offer digital voice and low rate data communications, including the Global System for Mobile communications (GSM) and IS-95, started to gain momentum since the mid 1990's. In GSM systems, the TDMA method is employed so that different users will share the same bandwidth but transmit on different time slots. The IS-95 standard uses the Code Division Multiple Access (CDMA) technique where a Pseudo Noise (PN) sequence is used to convert a narrowband signal to a wideband noise like signal before transmission [3][5]. Multiple users have access to the same channel bandwidth, carrier frequencies and time slots, and each user is distinguished by its own PN sequence that is approximately orthogonal to all other users' sequences. The 3rd Generation (3G) system concept was first conceived in 1998 to further increase the number of system users and the transmission rates using a wider bandwidth at 5 MHz comparing to the 1.25 MHz in CDMA systems. The 3G systems, which also use the CDMA technology, are designed for multi-level services including speech and multimedia high rate data up to 2 Mb/s [6][7]. There are several existing proposals for 3G system standards that are being developed and implemented concurrently by different standard bodies, such as the European and Japanese Wideband Code Division Multiple Access (WCDMA) systems, and the American CDMA2000 system [5].

1.2 Advancements in the Antenna Systems

In addition to the evolution of the multiple access techniques, there are also significant advancements in the antenna technology. Specifically, the Spatial Division Multiple Access (SDMA) technique exploits the multiplicity of spatial channels based on the fact that each user occupies a unique spatial location [2]. There are a number of

methods to achieve this, from simple sectorization schemes to complex adaptive antenna algorithms. Their ultimate goal is to reduce the interference according to the Angles of Arrival (AOA's) and therefore maintain the Signal to Noise Ratio (SNR) and / or the Signal to Interference plus Noise Ratio (SINR) of the received signals at an acceptable level [3][8]. The traditional sectorization method utilizes several directional antennas at an antenna site with each directional antenna covering a specific region. By limiting the service regions of the antennas, it can effectively reduce the interferences coming from other sectors.

On the other hand, the recently developed adaptive antenna algorithms allow the manipulation of the antenna directivity by generating desired antenna patterns and adaptively controlling the patterns using software. For the fact that these adaptive antenna algorithms can adjust the antenna patterns at runtime according to the channel conditions, signal levels and user locations to maintain the Quality of Service (QOS), they are also referred to as the smart antennas [3][8][9]. Furthermore, since signal distortions and delays could cause the desired signals to arrive in multipaths in the temporal domain, the Rake receiver with time matching fingers has been designed to pick up signals with temporal delays [10]. Hashemi, based on experimental data, designed a multipath model for different types of urban environments to generate user power profiles emulating realistic multipath scenarios that can be used in computer simulations [11].

The adaptive antenna algorithms that control antenna patterns are designed to handle signals in the space domain while the Rake receiver is intended to deal with signals in the temporal domain. Past research based on AOA estimation in the space domain includes the MEM, MUSIC, and ESPRIT, where the receivers continually monitor the desired

signals, multipaths, and interfering signals while estimating the AOA's at the same time [2][9][12]. Using the obtained information, it is possible to steer the main beam of the antenna to the direction of the desired user in order to eliminate the undesired interferences. This smart antenna technique is called the Maximum Ratio Combining (MRC). Another smart antenna technique is the Interference Rejection Combining (IRC) in which nulls take place towards the interfering signals while the main lobe of the antenna pattern enhances the desired signal [13][14]. To take advantage of the space-temporal characteristics of the channel, a 2 Dimensional (2D) antenna array system with spatial and temporal processing capabilities is implemented for simulations in this thesis.

1.3 Past Research in 3G System Capacities and the Main Contributions of this Thesis

Due to the interests in the 3G systems, several recent technical publications have dealt with the performance of the WCDMA physical and transport network layers or the so-called radio interface. In [5][6], the physical and transport network layers of the WCDMA are described in detail and the Bit Error Rate (BER) performance of the physical layer against different SNR's was examined. Some other papers in the literature determined the WCDMA system capacity based on simplified analytical models. Pinto *et al.* in [15] used analytical approaches to model the multi-cell and multiple services environments, but have not addressed issues in antenna types or the transmission channel. In [16], Laiho-Steffens *et al.* have designed analytical models to compute the user transmit powers and the carrier-to-interference-ratios in order to simulate the WCDMA capacity under different antenna configurations. Jones and Owen in [17]

proposed a Monte Carlo simulator for determining capacity and RF system design using fixed multipath power profiles and an identical antenna orientation. In [13][14], different configurations of the MRC and IRC smart antennas have been compared for SINR gains of the WCDMA system, although their effects on the system capacity have not been mentioned.

Inspired by the recent research work done for the 3G systems, this thesis presents a comprehensive investigation of the performances in terms of system capacities in a practical WCDMA system under various system configurations. To achieve this goal, a generic software platform that simulates the WCDMA system to determine the interference limited system capacity is developed. The approaches and methodologies used in this software platform are adapted from Chiu [18] and Chan [19], who have done their research in the performances of the IS-95 CDMA system with the smart antennas. In order to accurately estimate the capacity, the WCDMA simulator is realized with a realistic physical layer model, a practical multipath channel model as well as an antenna model that are flexible to emulate urban channel environments and various antenna configurations for the 2D antenna array system. Specifically, the main research contributions of this thesis are summarized as follows:

- The interference mitigation performance of the IRC antenna in the WCDMA system is compared in terms of system capacity results with that of the MRC antenna. The proposed smart antenna model makes use of the pilot signals to estimate parameters required in both IRC and MRC antennas to mimic realistic transmission circumstances.

- By proposing the use of a WCDMA physical layer model with actual coding and decoding operations instead of an analytical model, the system performances are investigated for realistic mixed traffic scenarios with voice and multimedia user groups transmitting at different data rates.
- Accurate system capacities of the WCDMA system have been obtained for the interference limited uplink direction using the multipath channel model previously mentioned for different geographical environments. Capacity improvements are compared against varying numbers of antenna elements and Rake fingers as well as between single path and multipath conditions.
- The system performances of the turbo codes and the traditional convolutional codes, the two possible transport channel coding mechanisms for the transport network layer, are compared.

1.4 Organization of this Thesis

This thesis consists of seven chapters. After this introductory chapter, the organization of the thesis is as follows.

Chapter 2 presents an overview of the transport network and physical layers model of the WCDMA simulator. This model is composed of several sub-systems, namely the transport channel encoder, the spreading encoder, the scrambling encoder, and their corresponding decoders [6]. Also included in this chapter is the overall transmission path model that illustrates the data flow operations before radio transmission.

In Chapter 3, the WCDMA channel model that is used in the simulator is presented.

The chapter begins with the introduction of the large scale and small scale propagation models. The large scale propagation model describes the propagation loss and signal scattering in the outdoor, urban environment, whereas the small scale propagation model briefly touches upon the time and frequency dispersions. What follows is a frequency selective, slow fading channel model that is implemented in the WCDMA simulator. This channel model consists of the Hashemi multipath power profile model, the Rayleigh fading model, a tapped-delay-line channel model, as well as the large scale propagation model.

Chapter 4 introduces the various antenna technologies considered in this thesis. The physical features that are emulated in the WCDMA simulator include antenna arrays, Rake receivers, and the combination of the spatial and temporal receivers. The software implemented smart antenna technologies employed in the simulator include the MRC and IRC methods. The parameter estimations based on pilot signals for these two methods are also presented.

The first part of Chapter 5 gives an overview of the WCDMA uplink path model, including the transmitter, channel, and receiver sub-systems that incorporate and integrate the various models introduced in the previous chapters. The second part of this chapter describes the system methodology explaining the sequence of the pre-run setup steps for the simulator, the mechanisms for the open loop and closed loop power controls, and the processes involved in the actual capacity simulation runs [20].

In Chapter 6, the WCDMA system capacity simulation results are presented. To start with, the parameters necessary for the simulation runs are defined. This is followed by the system capacity simulation results which are illustrated in terms of

Cumulative Probability Density Function (CDF) graphs as well as tabulated in tables [19]. The capacity results are obtained for various antenna configurations, mixed data traffics, and multipath environments. Also included are discussions of the results as well as comparisons of these results with those in other publications.

Chapter 7 presents the conclusion of the thesis and suggestions for future research.

Chapter 2 TRANSPORT NETWORK AND PHYSICAL LAYERS OF WCDMA

2.1 Introduction

The transport network and physical layers of the 3G system are implemented as the foundation for the WCDMA smart antenna simulator. The transport network layer is mainly responsible for data formatting and error checking, whereas the physical layer plays a major role in accommodating the multi-rate services according to the various user needs [21]. It is important to note that there are several proposals for the 3G system standards such as the WCDMA and CDMA2000 systems. They have some key properties in common, including coherent uplink transmission using pilot signals, fast power control, multi-rate services, and improved performance over the 2G systems. However, they operate on different parameters, such as chip rate, frame length, power control loop frequency, *etc.* The software simulator designed for this thesis has its main focus on the data transmission of the transport network and physical layers and closely follows the WCDMA standard adapted in the 3G Partnership Project (3GPP) [22].

This chapter is organized as follows. Section 2.2 discusses the transport channel types and the channel coding operations that take place at the transport network layer. Section 2.3 describes the physical layer encoding and decoding operations required before radio transmission. Section 2.4 includes the transmission path model which recapitulates the data operations performed before radio transmission and a numerical example of the data operations. Finally, the conclusions of the chapter are presented in Section 2.5.

2.2 Transport Channels and Channel Coding Operations of the Transport Network Layer

In the WCDMA system, the data generated at higher layers are channel coded, multiplexed, and then sent from the transport channels of the transport network layer to the physical channels at the physical layer. This section will describe the transport channel types and the two channel coding mechanisms that are used in the transport network layer.

2.2.1 Transport Channel Types

There are two types of transport channels, the common channels and the dedicated channels. A common channel is utilized by all or a group of users in a cell, sharing its resources, and a dedicated channel, on the other hand, is identified by a specific code and frequency and set aside for a single user only. To reduce the complexity of the simulation software, however, these common channels are beyond the scope of this thesis. Instead, only the dedicated transport channel will be explored. The only dedicated transport channel is the Dedicated Channel (DCH), which is used to transmit user-specific data or control information coming from the higher layers [23].

The user-specific data and control information transmitted through DCH will be encoded and multiplexed before being sent to the physical layer as described below. Transport block sets arrive from higher layers to the coding and multiplexing units of the transport channels once every Transmission Time Interval (TTI). They are encoded and multiplexed in order to provide error detection, error correction, rate matching, and interleaving. These operations include the Cyclic Redundancy Code (CRC) attachments,

block concatenation or segmentation, transport channel coding, frame equalization and segmentation, first and second level interleaving, and channel multiplexing [20]. For the purpose of software simulation for this thesis, only the transport channel coding operation will be considered at this stage. As defined in the 3GPP WCDMA standard, there are two possible encoding methods for the transport channel coding process, namely, the convolutional coding and turbo coding. These two coding methods are discussed in the following sub-sections.

After the transport channel coding, the transport DCH will be mapped onto two physical channels, with the Dedicated Physical Data Channel (DPDCH) carrying user data and the Dedicated Physical Control Channel (DPCCH) carrying the control information. These two physical channels at the physical layer will carry out the necessary preparations and operations before radio transmission.

2.2.2 Convolutional Encoding and Decoding

One of the two possible transport channel coding methods is convolutional encoding. This coding method, which provides error control and improvements in signal quality through redundancy of data and the use of a linear register, yields on average arbitrarily high levels of reliability. It is performed over an entire data stream regardless of the length. The convolutional encoder implemented for this thesis has a rate of $r_{conv} = 1/3$ and a constraint length of $K_{conv} = 9$ as shown in Figure 2.1. Each input data bits of length N_{data} will be encoded into a data word of length $3N_{data}$. The rate r_{conv} is determined by the number of output bits generated per input bit. In this case, every input bit produces 3 output bits, i.e. $r_{conv} = 1/3$. As illustrated in Figure 2.1, each output

bit, Output 0, Output 1, and Output 2, is a linear combination of the input bit. The three generator sequences used to produce the three outputs are

$$\begin{aligned} G_0 &= (101101111) \text{ binary} = (557) \text{ octal} , \\ G_1 &= (110110011) \text{ binary} = (663) \text{ octal} , \text{ and} \\ G_2 &= (111001001) \text{ binary} = (711) \text{ octal} \end{aligned} \quad (2.1)$$

where G_n with the subscript $n = 0, 1$, and 2 denotes the generator sequence.

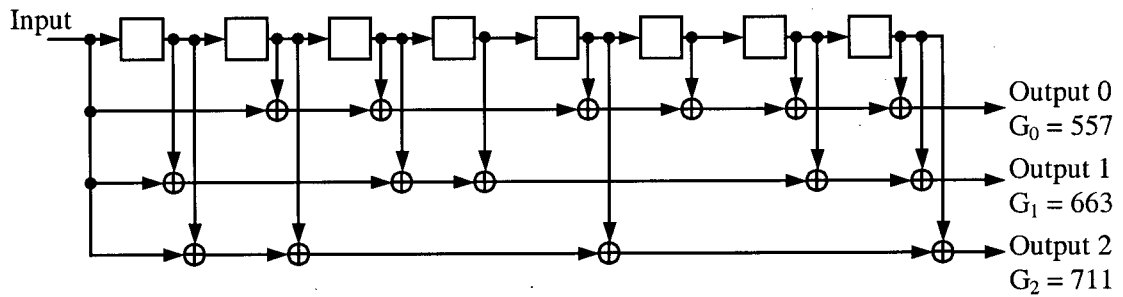


Figure 2.1 Convolutional Encoder with $r_{conv} = 1/3$ and $K_{conv} = 9$

Let the received noisy sequence at the convolutional decoder be denoted as \mathbf{v}_{conv} and the convolutional decoded output be \mathbf{u}_k . Regardless of the code structure, for a data word of length $3N_{data}$, a simple Maximum Likelihood (ML) decoder, which selects the output that maximizes $p(\mathbf{v}_{conv} | \mathbf{u}_k)$, would have to correlate $2^{3N_{data}}$ code sequences to the noisy received sequence and choose the codeword with the best correlation metric as the decoded output [24]. This brute force approach is never utilized in practice due to its exorbitant computational complexity. Instead, the hard decision Viterbi algorithm is employed to decode the convolutional encoded data at the receiver.

2.2.3 Turbo Encoding and Decoding

The other possible transport channel coding method is turbo coding. Turbo codes were first presented in 1993 with the decoding capability that approaches the Shannon limit [25]. The coding community widely believes that turbo codes are a very significant advancement since the introduction of Ungerboeck's trellis codes in 1982 [26]. The near capacity performance of turbo codes has since led to an enormous amount of research in iterative decoding algorithms as well as recursive encoders. The features of turbo codes include a parallel-concatenated encoder, a PN interleaver, and an iterative decoder composed of two Maximum a Posteriori (MAP) decoders.

2.2.3.1 Turbo Code Encoder

A standard turbo code encoder consists of two 1/2 rate convolutional encoders separated by an interleaver and an optional puncturer [25]. The diagram of a turbo code encoder is shown in Figure 2.2.

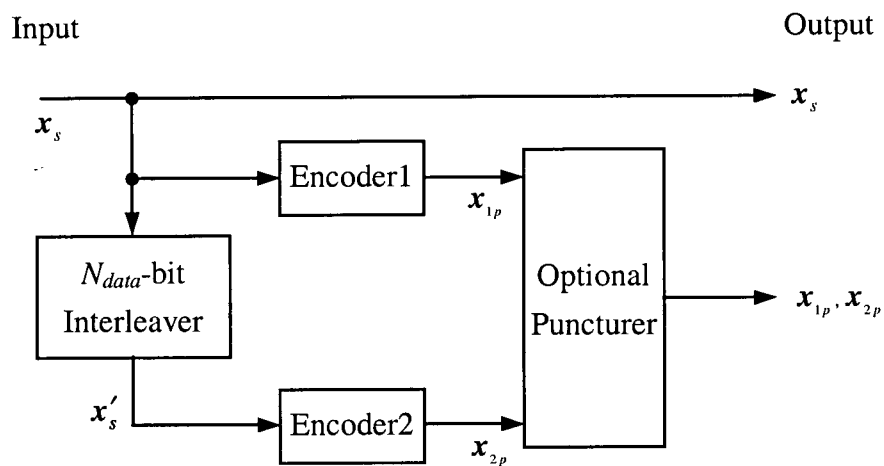


Figure 2.2 A Typical Turbo Code Encoder with Two RSC's

In this figure, the input codeword to the encoder is an N_{data} -bit word denoted as x_s , the output words by the first and second encoders are of size N_{data} and denoted as x_{1p} and x_{2p} respectively, and the output by the interleaver is x'_s . Without the optional puncturer, the turbo code encoder has a encoding rate of $r_{turbo} = 1/3$, mapping N_{data} data bits into $3N_{data}$ code bits arranged in parallel concatenation as $v_{turbo} = [x_s, x_{1p}, x_{2p}]$ for the turbo encoder output. The two convolutional encoders are two identical Recursive Systematic Coders (RSC's) with the generator matrix

$$G_R(D) = \begin{bmatrix} 1 & \frac{G_2(D)}{G_1(D)} \end{bmatrix} \quad (2.2)$$

where $G_1(D)$ and $G_2(D)$ are generator polynomials. In this thesis, the RSC generator matrix is implemented with $(G_1, G_2) = (31, 27)$ in the octal form [26] as illustrated in Figure 2.3.

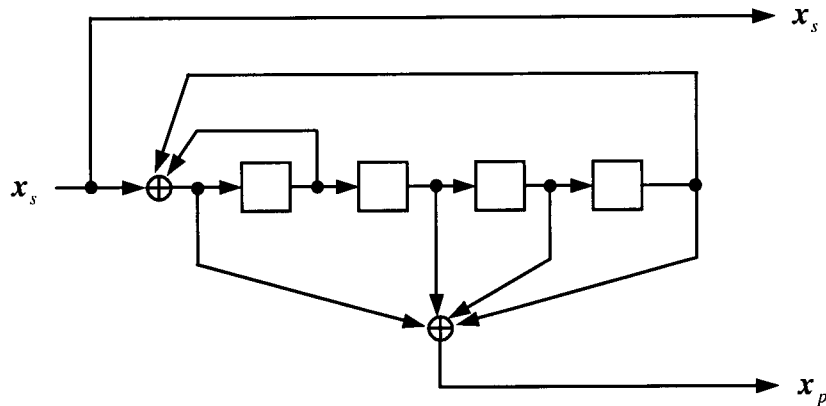


Figure 2.3 Configuration of the RSC Generator with $(G_1, G_2) = (31, 27)$

In Figure 2.2, an interleaver is placed between the first and the second convolutional

encoders to permute the input data before feeding it to the second encoder. This interleaver serves as a critical component of a turbo code encoder in achieving good performance. Unlike classical interleavers which rearrange bits in a systematic manner, the interleaver for turbo codes will reshuffle input bits in a PN fashion that lacks any apparent order. By setting the interleaving frame length to one thousand symbols or greater, the performance of the PN interleaver could approach that of random codes [26]. Furthermore, the turbo code interleaver could contribute to the iterative decoding process by decorrelating the Log Likelihood Ratios (LLR's) of the input symbols to be decoded.

2.2.3.2 Turbo Code Iterative Decoder

As described in Section 2.1.2, the Viterbi algorithm for decoding convolutional encoded messages offers a systematic method of eliminating possible candidate code sequences, making the decoding process a problem of logarithmic complexity rather than exponential. For turbo codes, however, the decoding process is much more complex due to the presence of an interleaver in the encoder that complicates the turbo code trellis. To decode turbo codes, a more sophisticated algorithm is used.

In a symbol-by-symbol MAP decoder, the decoder determines the decoded message to be $u_k = 0$ if $P(u_k = 0 | v) > P(u_k = 1 | v)$, and $u_k = 1$ otherwise, where v is the noisy received codeword. Since the turbo code decoder involves iterative decoding, the a priori and channel information are also required in the decoding process. Thus, the decoded message \hat{u}_k is determined by

$$\hat{u}_k = \text{sign} [\Lambda_{DEC}(u_k)] \quad (2.3)$$

where

$$\Lambda_{DEC}(u_k) = \Lambda_{k,c} + \Lambda_a(u_k) + \Lambda_{k,e}(u_k), \quad (2.4)$$

is the combined LLR of the channel LLR $\Lambda_{k,c}$, a priori LLR $\Lambda_a(u_k)$, and the extrinsic LLR $\Lambda_{k,e}(u_k)$. In Bayes' rule [26], the channel LLR $\Lambda_{k,c}$ is given by

$$\Lambda_{k,c} = \frac{4E_c}{N_o} v_k \quad (2.5)$$

for an AWGN channel with the variance $\sigma_n^2 = N_o/2$ where $E_c = rE_b$ is the energy per channel bit and v_k is the received noisy codeword. The a priori LLR $\Lambda_a(u_k)$ for the first iteration is expressed as

$$\Lambda_a(u_k) = \log \left(\frac{P(u_k = +1)}{P(u_k = -1)} \right). \quad (2.6)$$

The extrinsic LLR $\Lambda_{k,e}(u_k)$ is defined in the BCJR algorithm [27] as

$$\Lambda_{k,e}(u_k) = \log \left(\frac{\sum_{s^+} \tilde{\alpha}_{k-1}(s') \gamma_k(s', s) \tilde{\beta}_k(s)}{\sum_{s^-} \tilde{\alpha}_{k-1}(s') \gamma_k(s', s) \tilde{\beta}_k(s)} \right), \quad (2.7)$$

where $s_k \in S$ is the state of the encoder at time k , S^+ is the set of ordered pairs (s', s) corresponding to all state transitions $(s_{k-1} = s') \rightarrow (s_k = s)$ caused by data input $u_k = +1$, and S^- is the same for $u_k = -1$. In Equation 2.7,

$$\begin{aligned} \tilde{\alpha}_k(s) &= \alpha_k(s) / p(v_1^k) \\ &= \sum_{s' \in S} \alpha_{k-1}(s') \gamma_k(s', s) / p(v_1^k), \end{aligned} \quad (2.8)$$

$$\begin{aligned}\gamma_k(s', s) &= P(s | s') p(v_k | s', s) \\ &= P(s' \rightarrow s) p(v_k | s' \rightarrow s),\end{aligned}\quad (2.9)$$

$$\begin{aligned}\tilde{\beta}_k(s) &= \beta_k(s) / p(v_{k+1}^N | v_1^k) \\ &= \sum_{s \in S} \beta_{k+1}(s) \gamma_{k+1}(s', s).\end{aligned}\quad (2.10)$$

where $p(v) / p(v_k) = p(v_1^{k-1}) p(v_{k+1}^N | v_1^k)$.

The iterative decoding of turbo codes employs two MAP-BCJR decoders as depicted in Figure 2.4.

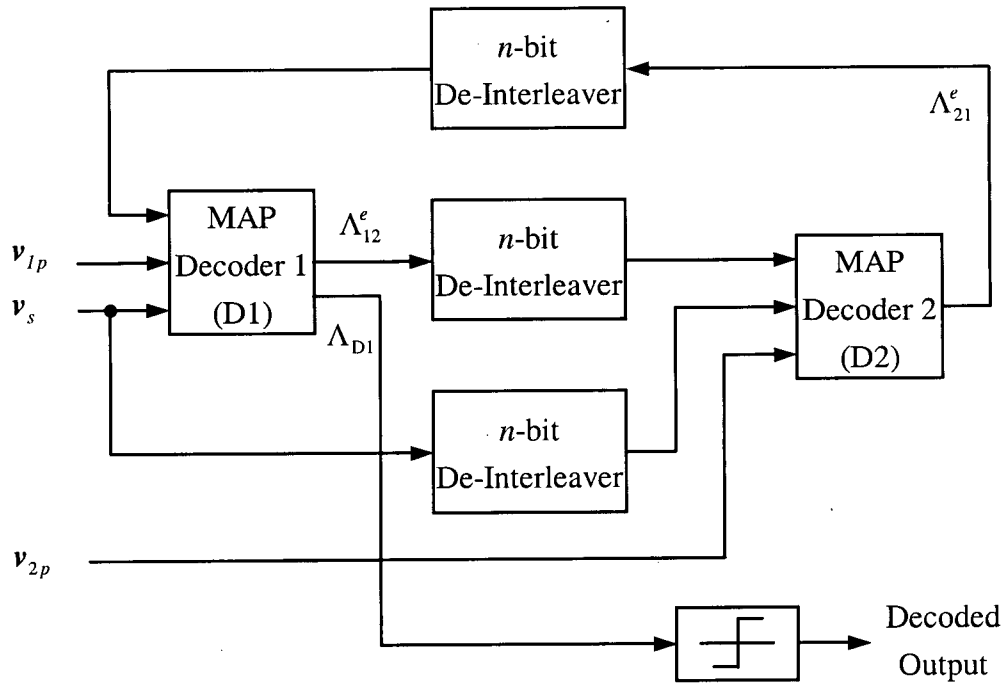


Figure 2.4 Iterative Turbo Code Decoder with Two MAP Decoders

Each decoding iteration involves two stages of decoding, one for Decoder 1 (D1) and the other for Decoder 2 (D2). In iterative decoding, the a priori LLR $\Lambda_a(u_k)$ of a decoder becomes the extrinsic information passed from the previous decoder, and the

extrinsic LLR $\Lambda_{k,e}(u_k)$ of a decoder will be passed to the next decoder as the a priori information. In other words, the output for D1 is determined by

$$\begin{aligned}\Lambda_{D1}(u_k) &= \Lambda_{k,c}^{D1} + \Lambda_a^{D1}(u_k) + \Lambda_{k,e}^{D1}(u_k) \\ &= \Lambda_{k,c}^{D1} + \Lambda_{21}^e(u_k) + \Lambda_{12}^e(u_k).\end{aligned}\tag{2.11}$$

The channel LLR, a priori LLR, and the extrinsic LLR for D2 are denoted as $\Lambda_{k,c}^{D2}(u_k)$, $\Lambda_a^{D2}(u_k)$, and $\Lambda_{k,e}^{D2}(u_k)$ respectively. For D1, the a priori LLR $\Lambda_a^{D1}(u_k) = \Lambda_{21}^e(u_k)$ in Equation 2.11 is the extrinsic information $\Lambda_{k,e}^{D2}(u_k)$ computed by D2 and passed from D2 to D1 as illustrated in Figure 2.4. Also, the extrinsic LLR $\Lambda_{k,e}^{D1}(u_k) = \Lambda_{12}^e(u_k)$ computed by D1 will become the a priori LLR $\Lambda_a^{D2}(u_k)$ for D2. After a specific number of iterations of computations between D1 and D2, the outcome generated by D1, $\Lambda_{D1}(u_k)$, will be used to estimate the value of u_k as the output of the turbo decoder [25].

2.3 Spreading and Scrambling Codes at the Physical Layer

After the transport channel encoding, data symbols arrive at the physical layer for further processing. At the physical layer, the major processes are encoding data symbols with spreading codes and scrambling codes and Quarternary Phase-Shift Keying (QPSK) modulating the encoded chips before radio transmission. This section will describe the basic concepts of spread spectrum CDMA systems, the spreading operation, and the scrambling operation.

2.3.1 Spread Spectrum Technique in WCDMA Systems

This section will provide a basic understanding of the spread spectrum technique that is applied in CDMA and WCDMA systems. Under the spread spectrum scheme, the narrowband data message of each user is multiplied by its own wideband PN codeword, which is also called the spreading code. The user message at the data rate is multiplied with the spreading code and converted to a set of chips to be transmitted at the chip rate. The spreading code size, also known as the Spreading Factor (SF), is the order of magnitude that a chip rate has over the message data rate, or simply,

$$SF = \frac{\text{Chip Rate}}{\text{Data Rate}} \quad (2.12)$$

The spreading operation corresponds to a widening of the transmission spectrum by SF, and thus the name spread spectrum technique.

The advantages of the spread spectrum technique are more apparent in the despreading operation as described here. Only the intended receiver will successfully decode the message by multiplying the received wideband chips with the same spreading code that has been used to spread the original message and then by integrating each set of the resulting chips to generate the narrowband user message. The integration process will produce a Processing Gain (PG) of SF in the signal level which is useful in suppressing interferences.

The WCDMA wideband nature yields the following system properties from its spreading and despreading operations.

- The spreading and despreading operations themselves do not improve the received

signal level for a user. The PG is at the expense of the increased transmission bandwidth, as granted by spreading the transmission spectrum.

- The variable data rate nature of a WCDMA system means that there are variable PG's for different types of users. According to Equation 2.12, within a fixed chip rate, lower data rate users would have a higher PG and whereas high data rate users would have a lower PG.
- The sharing of the same frequency for transmission by many users would average out the Multiple Access Interference (MAI) which would improve the system performance.

2.3.2 Spreading Codes at the Physical Layer

Spreading codes in the WCDMA system are used to separate transmissions from a single station or source. For example, a mobile station can be transmitting up to six parallel DPDCH's and one DPCCH at the same time in uplink transmissions, with each channel encoded by a different spreading code. In downlink, a base station makes connections to its subscribed mobile stations through various physical channels encoded by distinct spreading codes [20].

The SF of each user is determined by the user's data rate in a data transmission. The WCDMA system allows users to transmit at variable data rates according to the type of services required by the users. Therefore, SF has to be variable in order to be paired up with users' data rate for the fixed chip size. The spreading codes used in the WCDMA system are based on the Orthogonal Variable Spreading Factor (OVSF) technique [28]. OVSF codes preserve the orthogonality between a station's different

physical channels and allow the SF of a spreading code to be varied. The codes are picked from the code tree shown in Figure 2.5, according to the size of the SF needed by the particular transmission [29]. Each spreading code in Figure 2.5 is described by $C_{ch,SF,k}$, where k represents the k th number of the code set with the size SF for $0 \leq k \leq SF-1$. The layer number is represented as n in the figure, for $SF = 2^{(n+1)}$. $C_{ch,1,0}$ is the root of the code tree and the extensions from the root are its leaves. The leaves at the n th layer spanned from the $(n-1)$ th layer are considered the descendant codes, whereas the codes at the $(n-1)$ th layer are the mother codes of the leaves at the n th layer.

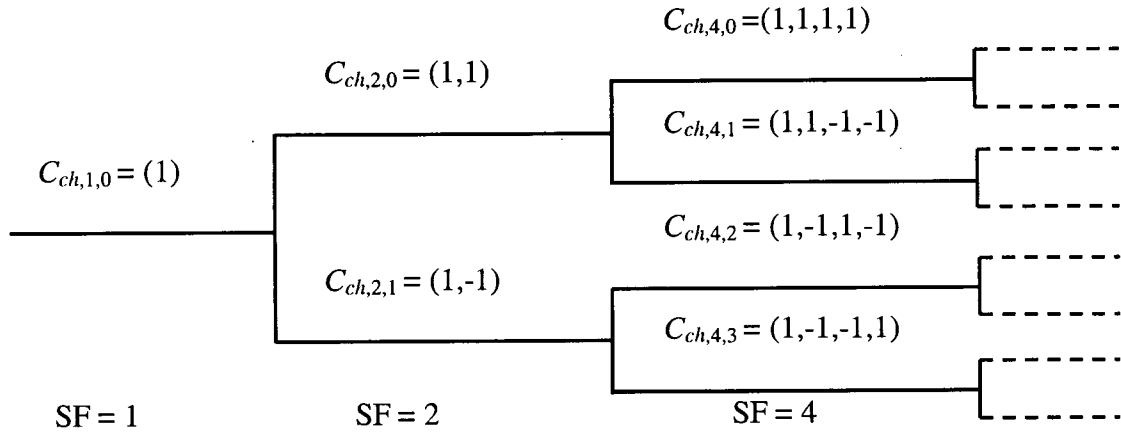


Figure 2.5 An OVSF Code Tree with 3 Layers Shown

The method for generating the code tree is illustrated in Figure 2.6. Each set of $2^{(n+1)}$ spreading codes is generated at the n th layer by the mother codes at the $(n-1)$ th layer that originated from the root $C_{ch,1,0}$. From the code structure shown in Figure 2.6, it can be understood that the generated OVSF codes of the same layer constitute a set of Walsh functions and they are orthogonal to each other [30]. Furthermore, any two codes from different layers are orthogonal to each other except when one of the two codes is the mother code of the other. Figure 2.7 is an example showing the orthogonal

characteristics of the OVSF codes and the code assignment rules that must be followed to ensure the orthogonality of the code set.

$$C_{ch,1,0} = 1$$

$$\begin{bmatrix} C_{ch,2,0} \\ C_{ch,2,1} \end{bmatrix} = \begin{bmatrix} C_{ch,1,0} & C_{ch,1,0} \\ C_{ch,1,0} & -C_{ch,1,0} \end{bmatrix} = \begin{bmatrix} 1 & 1 \\ 1 & -1 \end{bmatrix}$$

$$\begin{bmatrix} C_{ch,2^{(n+1)},0} \\ C_{ch,2^{(n+1)},1} \\ C_{ch,2^{(n+1)},2} \\ C_{ch,2^{(n+1)},3} \\ \vdots \\ C_{ch,2^{(n+1)},2^{(n+1)}-2} \\ C_{ch,2^{(n+1)},2^{(n+1)}-1} \end{bmatrix} = \begin{bmatrix} C_{ch,2^n,0} & C_{ch,2^n,0} \\ C_{ch,2^n,0} & -C_{ch,2^n,0} \\ C_{ch,2^n,1} & C_{ch,2^n,1} \\ C_{ch,2^n,1} & -C_{ch,2^n,1} \\ \vdots & \vdots \\ C_{ch,2^n,2^n-1} & C_{ch,2^n,2^n-1} \\ C_{ch,2^n,2^n-1} & -C_{ch,2^n,2^n-1} \end{bmatrix}$$

Figure 2.6 The Algorithm for Generating an OVSF Code Tree

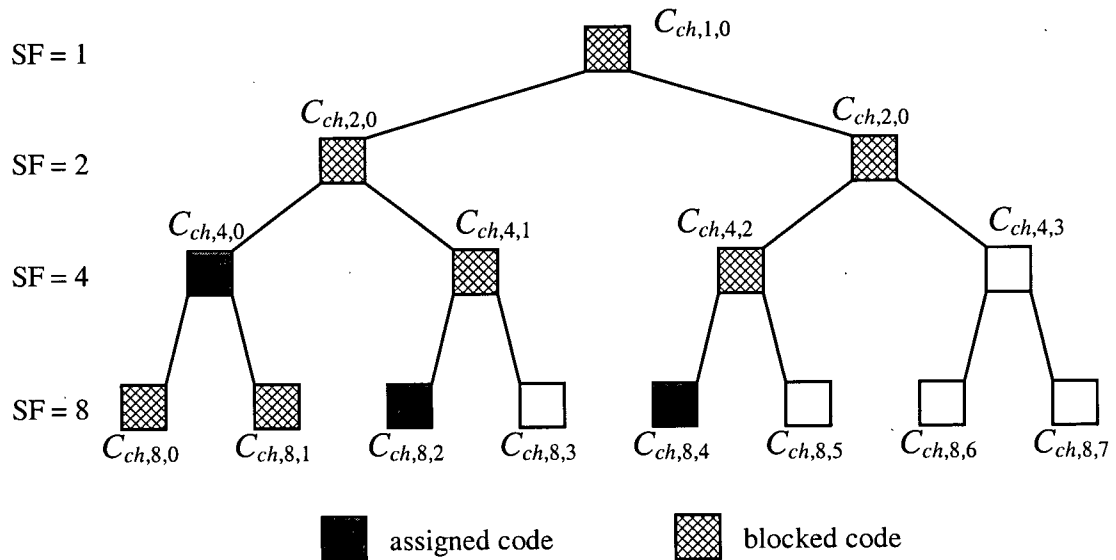


Figure 2.7 A Sample of OVSF Code Assignment Based on Orthogonality

In Figure 2.7, there are 3 OVSF codes that have already been assigned, $C_{ch,4,0}$, $C_{ch,8,2}$, and $C_{ch,8,4}$. Codes $C_{ch,1,0}$, $C_{ch,2,0}$, $C_{ch,2,1}$, $C_{ch,4,1}$, and $C_{ch,4,2}$ are blocked by their descendant codes and codes $C_{ch,8,0}$ and $C_{ch,8,1}$ are blocked by their mother code $C_{ch,4,0}$. $C_{ch,4,3}$, $C_{ch,8,3}$, $C_{ch,8,5}$, $C_{ch,8,6}$, and $C_{ch,8,7}$ are free to be assigned for new call requests. As a result, new requests can be blocked due to no spreading code available even though there are still unassigned codes in the code tree. Furthermore, it is possible to combine several OVSF codes of large sizes to support a call request for a small sized OVSF code. In the example, if a new call with a data transmission rate at 1/2 of the chip rate is to be set up, an OVSF code with a SF of 2 will have to be allocated for the request. However, there is no code with a SF of 2 available since $C_{ch,2,0}$ and $C_{ch,2,1}$ have been blocked. To still fulfill the call request, four codes $C_{ch,8,3}$, $C_{ch,8,5}$, $C_{ch,8,6}$, and $C_{ch,8,7}$ each with a SF of 8 and a data rate of 1/8 of the chip rate, can be assigned for four data channels [31]. By transmitting with these four codes, one for each of the four data channels, a total data rate of 1/2 of the chip rate is achieved.

As pointed out at the beginning of this section, spreading codes are used to separate channels from a source. For the uplink direction, they separate the DPDCH's and DPCCH's of the same mobile station. The rules for allocating spreading codes include the following. The uplink DPCCH is always coded by code $C_{ch,256,0}$. If there is only one DPDCH, it is spread by $C_{ch,SF,k}$ for k equals SF / 4.

The spreading factor on the DPDCH may vary on a frame-by-frame basis depending on the data rate information provided by the mobile station through the DPDCH. For downlink, with the same OVSF code tree structure, spreading codes separate the connections to different mobile stations from a base station within one cell or sector.

However, the dedicated channel SF is not allowed to vary on a frame-by-frame basis as in the uplink direction [5]. The data rate variation is taken care of by a rate matching operation or a discontinuous transmission at the transport network layer. There will be a numerical example demonstrating how the variable spreading code adjusts itself to accommodate different user data rates in Section 2.4.2 after all the components of the physical layer are introduced.

2.3.3 Scrambling Codes at the Physical Layer

The scrambling operation in the WCDMA system is used on top of the spreading operation to allow transmissions from different sources separable from each other. Unlike spreading, scrambling codes do not change the signal bandwidth, and therefore signals before and after the scrambling operation are both at the chip rate. By applying the scrambling codes, signals coming from different transmitting stations can still be distinguished even if they are coded with the same spreading code [20]. Each station will use a complex-valued scrambling code to scramble signals produced by the spreading operation for every radio frame. Thus, scrambling codes have the chip size of a radio frame.

The construction method of the scrambling sequences is as follows. The n th set of the complex scrambling sequence $C_{long,n}$ is constructed by two real value sequences. These two real value sequences are generated from the position wise modulo 2 sum of the radio frame chips segments of two binary sequences, which are created by two generator polynomials of degree 25. Let the two binary sequences to be x and y , and they are created by the primitive polynomials $X^{25} + X^3 + 1$ and $X^{25} + X^3 + X^2 + X + 1$

respectively over the Galois Fields GF(2) [22]. Thus x and y constitute segments of a set of Gold sequence. Let $x_n(i)$ and $y_n(i)$ denote the i th bit of the x_n and y_n sequences with $i = 0$ being the least significant bit. The subsequent bits are defined by the following recursive equations:

$$x_n(i + 25) = x_n(i + 3) + x_n(i) \text{ modulo } 2, \text{ and} \quad (2.13)$$

$$y_n(i + 25) = y_n(i + 3) + y_n(i + 2) + y_n(i + 1) + y_n(i) \text{ modulo } 2 \quad (2.14)$$

for $i = 0, \dots, 2^{25}-27$. The binary Gold sequence Z_n generated from the two sequences is

$$Z_n(i) = x_n(i) + y_n(i) \quad (2.15)$$

for $i = 0, \dots, 2^{25}-2$. With the binary to real value operation, Z_n is then converted to a real value sequence. Two real value scrambling sequences are defined as the following

$$C_{long,1,n}(i) = Z_n(i), \text{ and} \quad (2.16)$$

$$C_{long,2,n}(i) = Z_n [(i + 16777232) \text{ modulo } (2^{25} - 1)] \quad (2.17)$$

for $i = 0, 1, 2, \dots, 2^{25} - 2$. The complex-valued scrambling sequence $C_{long,n}$ is created by

$$C_{long,n}(i) = C_{long,1,n}(i) [1 + j(-1)^i C_{long,2,n}(2 \lfloor i/2 \rfloor)] \quad (2.18)$$

where $i = 0, 1, \dots, 2^{25} - 2$ and $\lfloor \cdot \rfloor$ denotes rounding to nearest lower integer. The configuration of the code generator is shown in Figure 2.8.

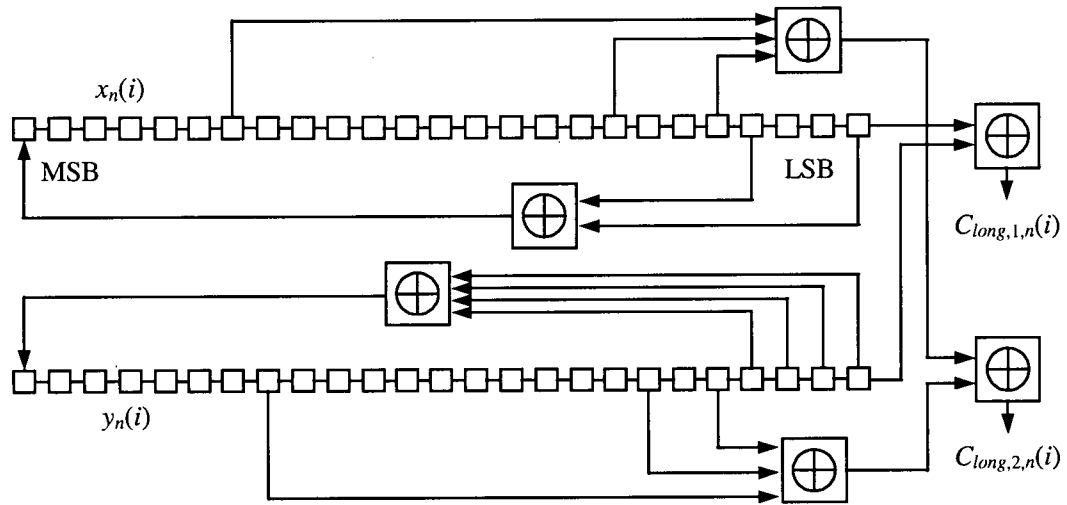


Figure 2.8 The Scrambling Code Generator

2.4 Transmission Path Overview

From the transport network layer to the radio transmission of the air interface, the transmission path of user data can be divided into several segments. These segments include coding and multiplexing at the transport channels, grouping the data into In-phase (I) and Quadrature (Q) channels [23], spreading and scrambling at the physical layer, and modulating signals for dual-channel radio transmission.

2.4.1 Transmission Path Model

Figure 2.9 shows the path model of the operations performed before radio transmission. In the figure, the data modulating operations are indicated above the arrows, and the data characteristics after each operation are illustrated in the rectangular blocks. A binary to real conversion of the data will take place between the transport network layer and the physical layer before further operations.

In the transmission path, raw data at a rate of N_{data} kbps are generated and sent to the multiplexing and coding unit at the transport network layer. The first operation to the raw data is either the convolutional encoding or the turbo encoding. The data rate of the convolutional or turbo encoded data is extended from N_{data} kbps to $3N_{data}$ kbps by the channel encoder with the rate of $1/3$. Encoded data are transferred to the physical channels at the physical layer mapped from the transport channels, and are further mapped to I and Q branches according to the physical channel types.

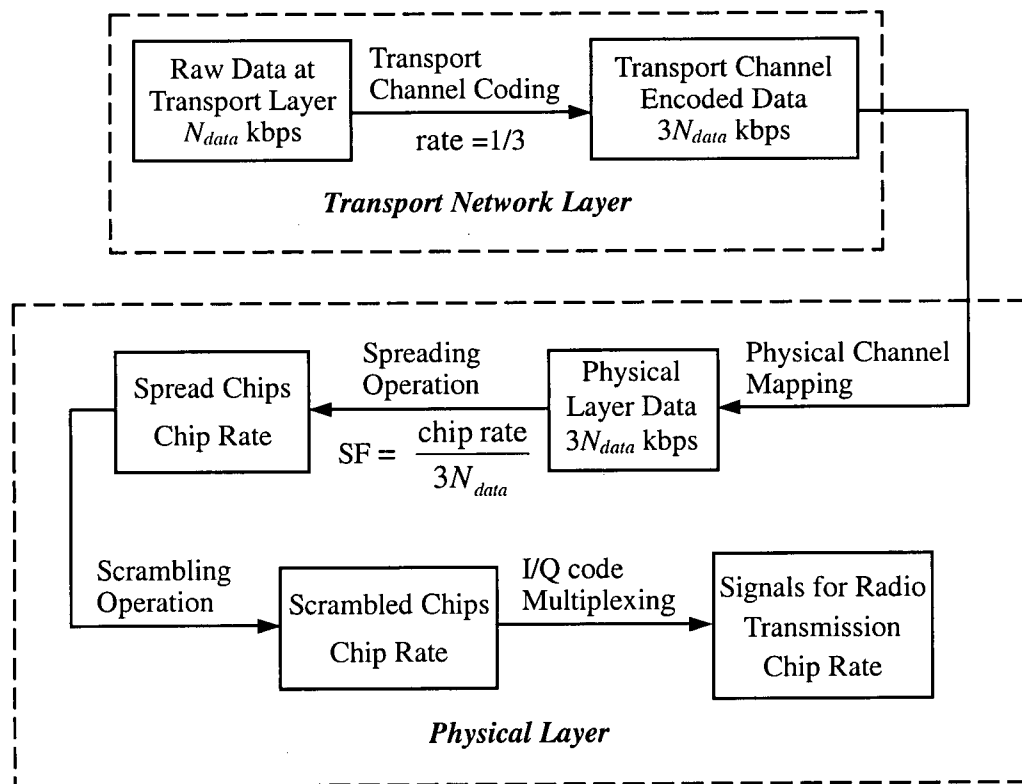


Figure 2.9 A Path Model Showing the Data Operations

Before any further coding and multiplexing operation, the convolutional or turbo encoded binary data are converted to real-valued data. The data with a rate of $3N_{data}$

kbps on each channel are spread to the chip rate by the spreading code with a SF of size $\text{Chip Rate} / 3N_{data}$. Then the channels on the I branch and the Q branch are combined together to produce a set of complex-valued sequence $I + jQ$. In the scrambling operation following the spreading operation, the complex-valued set of spread chips is complex multiplied with a set of scrambling code $C_{long,n}$. The resultant of the complex multiplication is also a set of complex sequences with the I and Q components having the chip size of a radio frame.

Before radio transmission, the complex-valued scrambled chips are modulated for digital passband transmission. Namely, the dual channel QPSK technique is used to modulate the data on the I and Q branches. As the name suggests, information carried by the transmitted signal at a carrier frequency is contained in the phase of the signal in QPSK. A QPSK signal is characterized by having a two-dimensional signal constellation and four message points with each message point corresponding to a unique pair of bits called a dibit. The scrambled complex-valued chips generated from the scrambling operation are QPSK modulated, filtered by a pulse shaping filter and then transmitted at the carrier frequency as shown in Figure 2.10. The pulse shaping filter in the figure is a root-raised cosine with the roll-off 0.22 in the frequency domain.

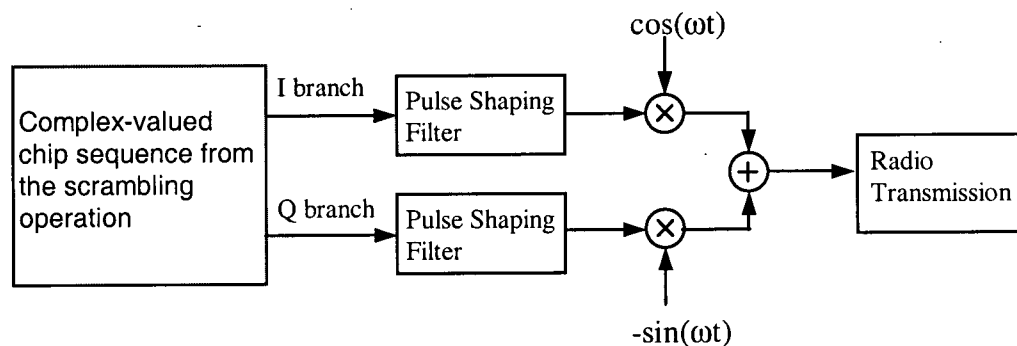


Figure 2.10 QPSK Modulations for the Complex-valued Signals

2.4.2 A Numerical Example of the Multi-rate Services

The following is an example to put the SF assignment in relations with variable data rate transmissions in the WCDMA system. In the WCDMA air interface specified by 3GPP, the chip size of one radio frame is specified to be 38400, with each radio frame being 10ms long for a chip rate of 3.84Mcps. For the simplicity of implementing the software simulator for this thesis, however, each radio frame is of 10ms long and contains 36864 chips, meaning that the chip rate of the transmission is at 3.6864Mcps.

Now, assume there are only two types of data allowed to be transmitted in the system, one being the voice data traffic at the rate of 19.2 kbps and the other the multimedia traffic at the rate of 76.8 kbps. Further assume that both the real and imaginary channels carry user data and that pilot bits are considered as data when making the calculations for the data rate. Then the single channel data rate would be 9.6 kbps for voice traffic and 38.4 kbps for multimedia traffic. Since the transport channel coding, being either the convolutional or turbo coding, would increase the signal rate by 3 times, the signal rate after the channel coding would then be 28.8 and 115.2 kilo-symbol-per-second for voice and multimedia data. Transport channel encoded data are then sent to the spreading encoder. The OVSF code of the spreading encoder will have to spread the current symbol rate to the chip rate before sending the signals to the scrambling encoder. Therefore, the SF for voice data can be calculated as

$$(3.6864 \times 10^6) / (28.8 \times 10^3) = 128 \quad (2.19)$$

and the SF for multimedia data would be

$$(3.6864 \times 10^6) / (115.2 \times 10^3) = 32. \quad (2.20)$$

The scrambling encoder will then process the spread signals at the chip rate and will not have any effect on the transmission rate of data.

2.5 Conclusions

In this chapter, the transport network layer and the physical layer of the WCDMA system have been introduced. Section 2.2 explains that the WCDMA software simulator for this thesis will focus on the user-specific dedicated channels performing data transmissions. The encoding and decoding algorithms of the two transport channel coding mechanisms – convolutional coding and turbo coding – have also been described in this section. In Section 2.3, the basic concept of spread spectrum has been presented, and the spreading and scrambling operations that modulate signals at the physical layer have been explained. Section 2.4 gives an overview of the transmission path model that includes all the data operations executed from the transport network layer to the physical layer, and provides a numerical example to illustrate how multi-rate services are realized through the use of the OVSF codes.

Chapter 3 THE CELLULAR STRUCTURE AND TRANSMISSION CHANNEL MODELLING

3.1 Introduction

WCDMA systems maximize the use of the available transmitting bandwidth by allowing multiple users simultaneously accessing the wireless network while each user is distinguished via an assigned codeword. System subscribers must be able to connect to the network in the system coverage area, which is often a large geographic area that cannot be covered with a single transmitter. Service providers therefore have to utilize the cellular concept to offer as much coverage as deemed necessary to satisfy their customers as well as increase the number of users in the system [4]. Furthermore, radio waves are the means of transmitting signals for WCDMA systems. Depending on the environment, the wireless signals will experience interferences from the surrounding objects that could change the characteristics and quality of the received signals. These effects on signal receptions due to the surrounding environment have been studied by researchers and categorized according to the characteristics of the wireless system parameters and the atmosphere variables. To simulate the effects that the surroundings have on the transmitted radio waves, transmission channel models are developed and implemented to reflect the signal variations.

This chapter is organized as follows. Section 3.2 describes the cellular concept that is widely used by wireless systems for the optimal coverage and services. Section 3.3 touches upon the effects the environment has on radio waves when transmitting over a large propagation distance, while Section 3.4 specifies those when transmitting for small

scale situations. Section 3.5 portrays the overall transmission channel model that is suitable for simulating the propagation effects of a WCDMA system. Finally, the conclusions of the chapter are presented in Section 3.6.

3.2 The Cellular Concept

This section is to provide an understanding of the cellular concept employed in mobile radio system designs. In the early era, the main design goal of a system was to provide good coverage for mobile stations while the cost of constructing Base Stations (BS's) was being minimized. As the number of users increased, the limited bandwidth of allocated frequency for personal use became a major challenge. The cellular concept offers increased capacity within a limited spectrum resource by reusing the allocated frequency efficiently. In the cellular model, each high power transmitter covering a large area are replaced by many low power transmitters with each providing services to a small hexagonal portion, also known as a cell, of the total service area. Frequency channel assignment is done in such a way that all the available channels are assigned to a cluster of cells so that the same frequency channels can be reused in different clusters and inter-cell interferences are minimized.

Let N_c be the number of cells in a cluster, g_c be the number of frequency channels assigned to each cell, and $Q_c = g_c N_c$ be the total number of channels available for the system. With a fixed cell size, the number of times that a cluster is replicated to cover the entire system, M_c , is inversely proportional to N_c . The capacity of the system, which can be measured by the total duplex channels available, is

$$C_{sys} = M_c g_c N_c = M_c Q_c. \quad (3.1)$$

Assuming the total bandwidth Q_c is constant, C_{sys} is directly proportional to M_c . By choosing the smallest possible value of N_c in the design, M_c and C_{sys} would be maximized in the equation. Therefore, the greater the frequency reuse factor $1/N_c$ is, the better the frequency usage efficiency, and the greater system capacity [4].

In the WCDMA system, all of the available bandwidth is reused in every cell, making $N_c = 1$ and the frequency reuse factor to be 1. Instead of dividing the total bandwidth into frequency channels to separate cells from each other, each transmitting source is identified by its own identification code. The identification codes, also known as the scrambling codes introduced in Chapter 2, are used to distinguish the signals of one user from those of another in a multi-user system.

3.3 Large Scale Propagation Models

In urban environments, often there is no direct Line Of Sight (LOS) between the source and destination, meaning that signals between the two cannot take a straight-line path. Signals undergo scattering by or around the objects in the transmission paths before being intercepted by the receivers. This section will introduce the scattering model and the Path Loss (PL) model that are utilized in this thesis.

3.3.1 Scattering Model

Scattering occurs when radio waves impinge upon a rough reflective surface, such as lamp posts or trees. When scattering occurs, the reflected energy of the radio waves is spread out or diffused in all directions, and a portion of the energy would travel in the direction of the receiver and become useful signal being picked up by the receiver.

Under the BS to Mobile Station (MS) transmission scenario in macro-cells, BS's are usually situated at high, obstruction-free locations such as high rise buildings or towers, and hence are free of scattering objects. On the other hand, MS's are very likely to be surrounded by a number of scatterers in all bearings. Based on this notion, Gans [49] in 1972 made the assumptions that the AOA's of the multipath signals arriving at the MS's is uniformly distributed over $[0, 2\pi)$ and that the signals arriving at the BS's would be restricted to a small angular region. Gans' proposed model has led to the development of the Geometrically Based Circular Model (GBCM). The GBCM, as shown in Figure 3.1, is utilized as the scattering model in this thesis.

In GBCM, the multipaths arriving at the BS's are confined to a small angular spread since there are no scatterers around the BS's. For transmissions from BS's to MS's, the GBCM assumes that all the scatterers for a particular MS are constrained to a scattering circle having the MS as its centre and a radius of r_s . The idea of a circular region of scatterers was originally proposed by Jakes [49]. The requirement that the separation distance between the BS and MS is larger than r_s is imposed in this model. r_s can be approximated by equating the angular spread of the signals arriving at the BS's predicted by the model. And based on the geometry, the angular spread is inversely proportional to the distance separating the BS and MS. Since scattered signals would arrive at the receivers of MS's from all directions after bouncing off from the surrounding scatterers once with the assumption of a single-bounce model, it is reasonable to assume that the AOA's at the MS's is uniformly distributed over $[0, 2\pi)$ for implementation simplicity in this thesis.

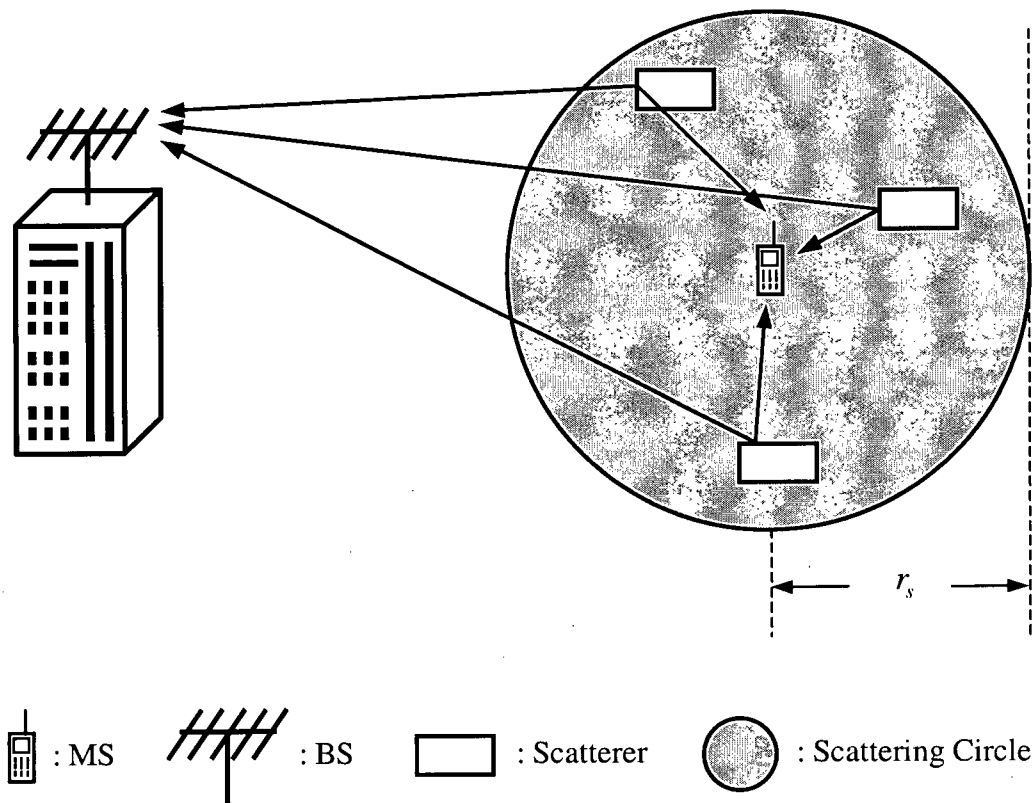


Figure 3.1 Geometrically Based Circular Model

3.3.2 Outdoor Propagation PL – Extended Hata Model

Okumura developed a model that is widely used for outdoor signal propagation prediction in urban areas and is applicable for a frequency range between 150 and 1920 MHz [4]. In the model, the median attenuation in an urban area over a quasi-smooth terrain relative to free space is indicated by a set of curves plotted by Okumura. These curves are obtained from measurements using omni-directional antennas with a BS antenna height of 200 metres and a MS antenna height of 3 metres. To determine the path loss between two points using the Okumura model, the free space PL has to be calculated first. Then the median attenuation due to the urban environment is read from

the Okumura curves according to the carrier frequency and the separating distance, and is added to the free space PL to produce the predicted PL for transmissions in urban cities.

From Okumura's model, an empirical formulation of the graphical PL curves is developed by Hata, and is valid for a frequency range between 150 and 1500 MHz. Hata presented a standard formula and correction equations with different situations for the urban area PL. Later, the European Co-operative for Scientific and Technical (COST) research developed an extension to the Hata model to expand the valid frequency range to 2 GHz [4]. This is the model that is implemented in this thesis to determine the PL between BS's and MS's. The proposed extended model for PL is

$$L_{path,50} (urban) (dB) = 46.3 + 33.9 \log f_c - 13.82 \log h_{te} - q(h_{re}) \\ + (44.9 - 6.55 \log h_{te}) \log d_{txrx} + C_M. \quad (3.2)$$

In Equation 3.2, $L_{path,50}$ is the 50th percentile value of PL, f_c is the carrier frequency in MHz valid from 1500 to 2000 MHz, h_{te} is the effective transmitting antenna height in metres ranging from 30 to 200 metres, h_{re} is the effective receiving antenna height ranging from 1 to 10 metres, and d_{txrx} is the distance in question and valid from 1 to 20 km. $q(h_{re})$ is the correction factor for the receiving antenna height and is defined by

$$q(h_{re}) (dB) = (1.1 \log f_c - 0.7) h_{re} - (1.56 \log f_c - 0.8) \quad (3.3)$$

for a small to medium sized city, and

$$q(h_{re}) (dB) = 3.2 (\log 11.75 h_{re})^2 - 4.97 \quad (3.4)$$

for a large city. In Equation 3.2, C_M is a correction factor for city sizes taking two values: 0 dB for a medium sized city and suburban areas, and 3 dB for metropolitan centres. Furthermore, for suburban areas the PL Equation 3.2 is modified as

$$L_{path,50} (\text{suburban}) \text{ (dB)} = PL_{50} (\text{urban}) - 2 [\log (f_c / 28)]^2 - 5.4 \quad (3.5)$$

and for open rural areas

$$L_{path,50} (\text{rural}) \text{ (dB)} = PL_{50} (\text{urban}) - 4.78 (\log f_c)^2 + 18.33 \log f_c - 40.94. \quad (3.6)$$

3.4 Small Scale Propagation Models

Small scale propagation models are used to estimate the rapid fluctuations of the received signals over very short travel distances, within a few wavelengths or short time durations on the order of seconds. The signal at the receiving antenna is the sum of several paths of the transmitted signal coming from random directions and angles as defined by the GBCM. Depending on the signal phases, these multipath components when summed together could cause either constructive or destructive interferences and hence the rapid fluctuations of the received signal, giving rise to the small scale fading. Small scale propagation models can be categorized based on the time and frequency dispersions, and the appropriate models are chosen for implementation in the WCDMA system in this thesis according to the nature of the transmitting signals and traffic channel parameters.

3.4.1 Fading Due to Time Dispersion

Based on the multipath time delay spread, small scale fading can be separated into flat fading and frequency selective fading. In flat fading where the channel coherence bandwidth is greater than the signal bandwidth, all the frequency components of the signal transmission undergo the same attenuation and phase shift through the channel. In frequency selective fading where the signal bandwidth is greater than the channel

coherence bandwidth, the multipath delay spread is greater than the chip period and the received signal includes multiple versions of the transmitted signal. Due to the time dispersion of the transmitted chips, Inter Symbol Interference (ISI) is induced, making certain frequency components of the received signal spectrum having greater gains than other frequency components.

The transmission channel of a WCDMA system will undergo the frequency selective fading for its signal bandwidth is greater than the channel coherence bandwidth [32]. Therefore, a frequency selective fading model, which is discussed in Section 3.5, is implemented in this thesis where multipath delays will cause ISI that could potentially downgrade the overall system performance.

3.4.2 Fading Due to Frequency Dispersion

By comparing the rates of change between the transmitted baseband signal and the channel, a channel can be categorized into a slow or fast fading channel. Movements of MS's or objects in the channel would cause the apparent received frequency of the transmitted signal to change.

Doppler shift, f_d , is used to describe this change in frequency induced by the motion of the receiver and is calculated by

$$f_d = \frac{v_{MS} f_c}{c_l} \cos \theta_d \quad (3.7)$$

where v_{MS} is the MS velocity, c_l is the speed of light at 3×10^8 m/s, and θ_d is the angle between the transmitter and the receiver [4]. Doppler spread is defined as the measure of the spectral broadening caused by the time rate of change of the mobile radio channel

and is assumed to be the maximum Doppler shift $v_{MS} f_c / c_l$. Coherence time T_{coh} , an inverse proportion of the Doppler spread, is used to characterize the time varying nature of the frequency dispersion of the channel in the time domain, and is defined as a statistical measure of the time duration over which the channel impulse response is invariant [3].

In fast fading, the channel impulse response changes rapidly within a chip duration, making the coherence time T_{coh} smaller than the chip period. Under this type of fading, the signal distortion caused by frequency dispersion increases with the increase of Doppler spread relative to the bandwidth of the transmitted signal. For slow fading, the chip duration is smaller than T_{coh} so that the channel attenuation and phase shift are essentially fixed for the duration of at least one chip interval. Under this type of fading, the Doppler spread of the channel is much less than the bandwidth of the baseband signal as the channel impulse response changes slower than the transmitted baseband signal. The transmitting chip duration for a WCDMA system is relatively small when compared to the coherence time of the transmission channel, which identifies it to be the slow fading category [33]. The slow fading model implemented in this thesis is discussed in Section 3.5.

3.5 Frequency Selective, Slow Fading Channel Model with PL

In order to realize a WCDMA transmission channel model that is comprised of the frequency selective slow fading characteristics and incorporated with the large scale propagation models described in Section 3.3, several smaller models have been implemented for this thesis. In these models, the directional considerations are

restricted to the horizontal plane, i.e. azimuth, without the loss of generality.

3.5.1 Frequency Selective, Hashemi Radio Propagation Model

The multipath delay profile for radio propagation extends typically from 1 to 2 μs in urban and suburban areas. For the WCDMA system considered for this thesis with a chip rate of 3.6864 Mcps, the chip duration is 0.27 μs . The WCDMA receivers will be able to separate the multipath components in a frequency selective channel by monitoring the delay of each path, measured by chips, as long as the time difference between the first path and the subsequent ones is at least 0.27 μs . Any two paths with a time difference less than this time will not be resolvable. Furthermore, the minimal 0.27 μs path difference in time for clearly distinguishable multipath components can be transformed to difference in length by multiplying the chip duration with the speed of light, which yields 81.4 metres [20]. A minimal path length difference of 81.4 m means that it is possible to obtain multipath components even for small scattering circles of the GBCM model for WCDMA systems when compared to the 244-metre path difference required for IS-95 systems at 1.2288 Mcps. This frequency selectivity will be combined with the multipath Hashemi model described as follows.

To study the multipath effects, Hashemi developed an outdoor propagation model based on measurements [11]. In the experiment, short pulses of half power width 100ns were transmitted at a fixed location and received by an antenna placed on a mobile vehicle. Hashemi conducted his research of radio propagation behaviours on urban environments such as downtown San Francisco, downtown Oakland, downtown Berkeley, and residential Berkeley, which represent a large city, a medium sized city, a suburban

region, and an open rural area respectively.

Under Hashemi's model, the time axis of arrival times is divided into intervals of durations of 100ns, which are also known as bins of arrival, with the origin of the axis being the first arriving path. P_{A_i} , the probability of having a path arrival in bin i , is described by $P_{A_i} = \psi_{A_i}$ if there is no path arrival in the $(i-1)$ bin, and $P_{A_i} = Q_{arr}\psi_{A_i}$ if there is a path arrival in the $(i-1)$ bin. ψ_{A_i} is the probability of path occurrences with an empirical path occurrence probability of r_{ocri} and is given by

$$\begin{aligned}\psi_{A_1} &= r_{ocri} & (i=1) \\ \psi_{A_i} &= \frac{r_{ocri}}{(Q_{arr}-1)r_{ocri-1}+1} & (i>1) .\end{aligned}\tag{3.8}$$

Q_{arr} is determined by minimizing the mean square error between experimental measurements and theoretical probability model as described above, and is set to a value greater than 1 due to the fact that it is more likely to have a path in the current bin if there is a path in the previous bin than if no path in the previous bin. It is assumed that there is only one arrival in the same bin [19].

The amplitude of each path is generated with a log-normal distribution. According to the mean and variance of the empirical data, the log amplitude for the first arriving path is generated with a normal distribution. The log amplitude of the next path is created by a conditional normal distribution with a mean and a variance conditional to the amplitude of the previous path. The path phase of each bin is generated with a uniform distribution between 0 and 2π . To allow the multipath components resolvable by chips,

bins are divided evenly into groups with each group having duration of one chip time. The paths of the bins within the same chip time, which cannot be resolved by the receiver, are added vector-wise together so that each group would represent one of the multipath components, numbered by k . The average power level of the k^{th} group is then determined by

$$P_{level_k} = |a_{k+1} \exp(\theta_{k+1}) + a_{k+2} \exp(\theta_{k+2}) + \dots + a_{k+Z_b} \exp(\theta_{k+Z_b})|^2 \quad (3.9)$$

where a_{k+Z_b} and θ_{k+Z_b} are the amplitude and phase of the path arrival of each bin [19]. Z_b represents the total number of bins in each multipath component. The path delay of the k^{th} multipath component $\tau_k(t)$ is one chip time more than $\tau_{k-1}(t)$, the path delay of the $(k-1)^{\text{th}}$ multipath component.

The multipath propagation channel can then be described by a linear Finite Impulse Response (FIR) filter [34] and described by

$$h(t, \tau) = \sum_{k=0}^{K-1} \alpha_k(t) \delta[t - \tau_k(t)] \exp[j\zeta_k(t)] \quad (3.10)$$

where $h(t)$ is the impulse response, $\alpha_k(t)$, $\zeta_k(t)$, and $\tau_k(t)$ are the k^{th} path amplitude, phase, and relative delay with respect to the first arriving multipath component determined by Hashemi model, and $\alpha_k(t)$ is defined as the square root of the average power of the multipath components derived from P_{level_k} in Equation 3.9. The total number of resolvable multipath components is denoted by K . Figure 3.2 illustrates the impulse response model.

Each impulse response model is considered as a multipath power profile that

describes the amplitudes, phases, and delays of the multipath components to be received by one antenna element. The power values of the multipath components in each profile are normalized so that their sum will be equal to unity. Consequently, the power value of every multipath component in a profile corresponds to a portion of the total received power by the antenna.

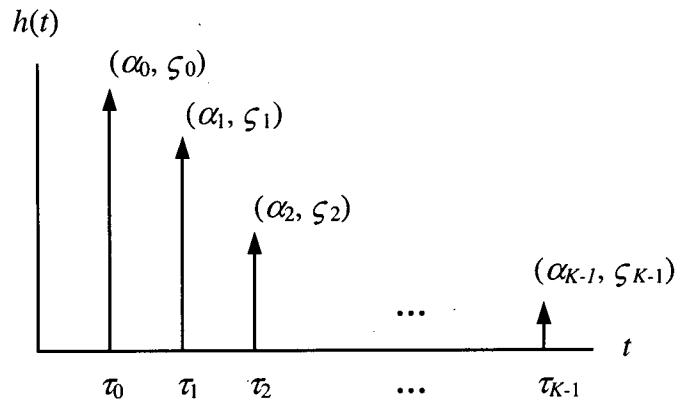


Figure 3.2 Impulse Response of a Multipath Power Profile

3.5.2 Slow Rayleigh Fading Model

The Rayleigh distribution is chosen to model the statistical time varying nature of the envelope of each multipath signal component of a slow fading channel for this thesis.

The Probability Density Function (PDF) of the Rayleigh distribution is described by

$$p_{\text{Rayleigh}}(r_e) = \begin{cases} \frac{r_e}{\sigma^2} \exp\left(-\frac{r_e^2}{2\sigma^2}\right) & (0 \leq r_e \leq \infty) \\ 0 & (r_e < 0) \end{cases} \quad (3.11)$$

where σ is the rms value of the received signal, σ^2 is the time average power of the received signal, and r_e is the signal envelope amplitude.

The envelope of a signal with the Rayleigh distribution is represented by the sum of two quadrature Gaussian noise signals. The random Rayleigh fading envelope is

$$\beta = \sqrt{\aleph_1(0, \sigma)^2 + \aleph_2(0, \sigma)^2} \quad (3.12)$$

where $\aleph_1(0, \sigma)$ and $\aleph_2(0, \sigma)$ are Gaussian distributions with a zero mean, and σ is the standard deviation. The Gaussian PDF with a zero mean is expressed as

$$p_{\text{Gaussian}}(r_e) = \frac{\exp[-r_e^2 / 2\sigma^2]}{\sqrt{2\pi}\sigma} \quad (3.13)$$

The phase due to Rayleigh fading, φ , is randomly generated with a uniform distribution between 0 and 2π with the PDF given by

$$p_{\text{uniform}}(r_e) = \begin{cases} 1/2\pi & (0 \leq r_e \leq 2\pi) \\ 0 & \text{elsewhere} \end{cases} \quad (3.14)$$

3.5.3 Tapped-Delay-Line Channel Model

To implement the frequency selective model combined with the Hashemi multipath model and Rayleigh fading model, a tapped-delay-line model is employed [9][35]. As mentioned previously, the multipath channel can be described by a FIR filter with a impulse response $h(t)$. Let $r(t)$ denote the output of such a FIR filter in response to the transmitted bit $s(t)$ as follows:

$$r(t) = \int h(t)s[t - \tau(\tau)]d\tau \quad (3.15)$$

Since the impulse response of the filter is a group of taps as seen in Figure 3.2, the integral in Equation 3.15, after substituted $h(t)$ with Equation 3.10, can be rewritten as the

convolutional sum

$$r(t) = \sum_{k=0}^{K-1} \alpha_k(t) \exp[j\zeta_k(t)] s[t - \tau_k(t)]. \quad (3.16)$$

Incorporating the large scale propagation loss L_{path} , Rayleigh fading model, and Additive White Gaussian Noise (AWGN) $\mathfrak{N}(t)$ with Equation 3.16, the received signal becomes

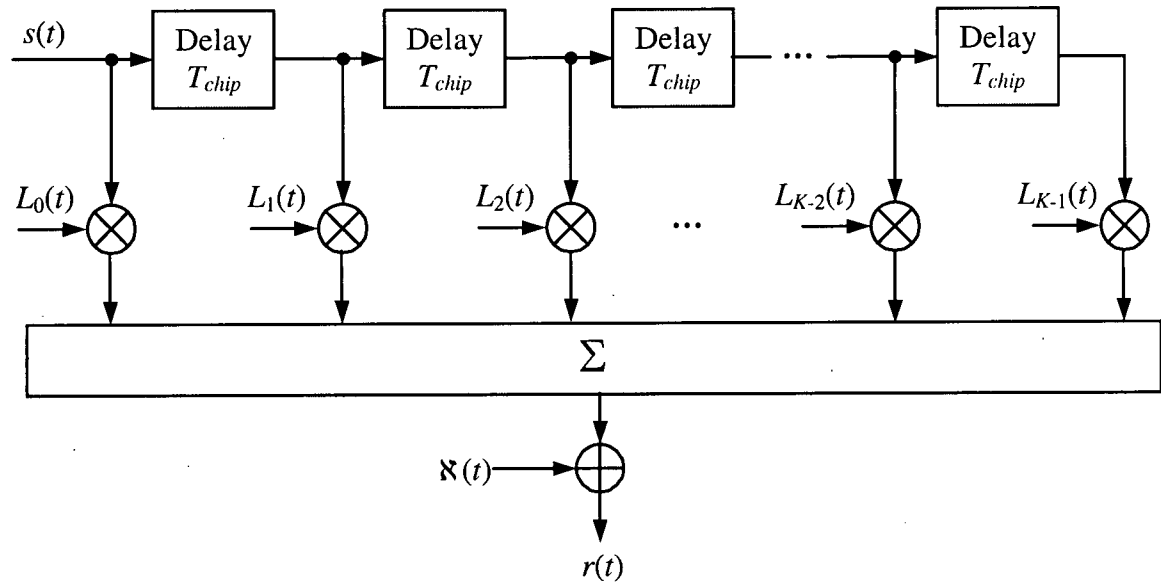
$$r(t) = L_{path} \sum_{k=0}^{K-1} \alpha_k(t) \beta_k(t) \exp[j\zeta_k(t)] \exp[j\phi_k(t)] s[t - \tau_k(t)] + \mathfrak{N}(t) \quad (3.17)$$

where $\beta_k(t)$ and $\phi_k(t)$ are the Rayleigh fading amplitude and phase. Let

$$\begin{aligned} L_k(t) &= L_{path} \alpha_k(t) \beta_k(t) \exp[j\zeta_k(t)] \exp[j\phi_k(t)] \\ &= a_k(t) \exp[j\phi_k(t)] \end{aligned} \quad (3.18)$$

so that $L_k(t)$ is the overall channel impulse response due to path loss, multipath fading, and Rayleigh fading for the k^{th} multipath component, and $a_k(t)$ and $\exp[j\phi_k(t)]$ are the amplitude and phase of the k^{th} multipath component where $a_k(t) = L_{path} \alpha_k(t) \beta_k(t)$ and $\phi_k(t) = \zeta_k(t) + \varphi_k(t)$.

To make the multipath components resolvable by chips, the resolution of the multipath profile is defined to be one chip duration T_{chip} for the tapped-delay-line model [33]. The number of multipath components K is one plus the result of dividing the multipath spread by the chip time T_{chip} . The tapped-delay-line model is depicted in the Figure 3.3. The model consists of a set of delay elements with each producing a delay of T_{chip} , a multiplier connected to the delay-line taps, a corresponding set of channel taps $L_k(t)$ applied to the multipliers, a summer adding the multiplier outputs, and an adder adding the summed output with the AWGN $\mathfrak{N}(t)$.

Figure 3.3 Tapped-delay-line Model with K Taps

3.6 Conclusions

In this chapter, the radio transmission channel for a WCDMA system has been introduced. Section 3.2 explains the principles of dividing a coverage area into cells as well as the frequency reuse technique used to increase the number of MS's that a system could accommodate. Then, the large scale propagation mechanisms, including the free space transmission sub-model for LOS transmissions, the GBCM sub-model that describes the scattering effects, and the Hata outdoor propagation sub-model are presented in Section 3.3. In Section 3.4, it has been determined that a WCDMA system would have a frequency selective, slow fading transmission channel. Section 3.5 gives an overview of the radio transmission model. Namely, the frequency selective Hashemi multipath model, slow Rayleigh fading model, and the tapped-delay-line channel model that incorporates the previous two models have been discussed in this section.

CHAPTER 4 ANTENNA STRUCTURES AND TECHNOLOGIES

4.1 Introduction

The configurations and the number of elements of the antenna set will affect the received signal levels. In addition, smart antenna technologies enable steering the antenna main lobes towards specific directions and rejecting interferences from certain bearings. Through careful design of the antenna system, interferences including ISI and MAI can be successfully suppressed or even turned to useful information to raise the SNR or SINR of the received signals at the receiver which in turn will increase the overall system capacity.

This chapter is organized as follows. In Section 4.2, the basic antenna concepts including antenna characteristics and antenna patterns are discussed. Section 4.3 gives an overview of the spatial-temporal antenna array system that is implemented in the thesis. The wave fronts arriving at an antenna array, the antenna patterns of linear antenna arrays, and the antenna Rake fingers used in temporal processing are considered in this section. The smart antenna technologies including three types of combining schemes and the estimations of the required parameters in these schemes are covered in Section 4.4. Finally, the conclusions of the chapter are presented in Section 4.5.

4.2 Fundamental Antenna Concepts

A brief overview of the fundamental antenna concepts including the antenna characteristics and the antenna radiation patterns will be covered in this section. The

important characteristics of a receiving antenna are its effective aperture A_r and its gain, and both depend on the wavelength of the radiated power and the physical parameters of the antenna. The gain of an antenna is given in reference to a standard antenna. As a reference, the resonant half-wave dipole antenna is a useful standard for comparing to other antennas at one frequency or over a very narrow band of frequencies. The antenna gain of a receiving antenna G_r can be related to A_r by

$$G_r = \frac{4\pi A_r}{\lambda^2} \quad (4.1)$$

where λ is the wavelength of the transmitted signal.

Another parameter that affects the antenna gain G_r is its beam width. A common definition for the beam width, denoted as Θ_B , is the -3dB width of the antenna pattern [36] and is approximated by

$$\Theta_B = 70(\lambda / D_{ant})^\circ \quad (4.2)$$

The radiation pattern of an antenna shows the relative strength of the radiated field in various directions from the antenna at a fixed or constant distance. Although radiation patterns are 3 Dimensional (3D), it is difficult to display the 3D radiation pattern in a meaningful manner [18]. As a result, radiation patterns here are presented in 2D as a slice of the 3D patterns.

The omni-directional antenna is an all directional antenna that radiates and receives equally well in all horizontal directions, and thus its antenna pattern would be concentric circles as the field strength decays in all directions. Directional antennas, on the other hand, focus energy in certain directions to have stronger fields and better coverage in those directions. A half wave dipole antenna made of wires with the length of one half

wavelength is an example of the directional antennas that is used as the standard for measuring antenna gains. The configuration and radiation pattern of this antenna are shown in Figure 4.1. In Figure 4.1(b), the antenna pattern is shown in bold lines on a field strength grid for all directions of a plane [37]. The concentric circles are the grid lines indicating the level of the normalized field strength at directions specified by diameter lines. The maximum gain of the antenna occurs at 90 and 270 degrees direction and is normalized and set to unity in the figure.

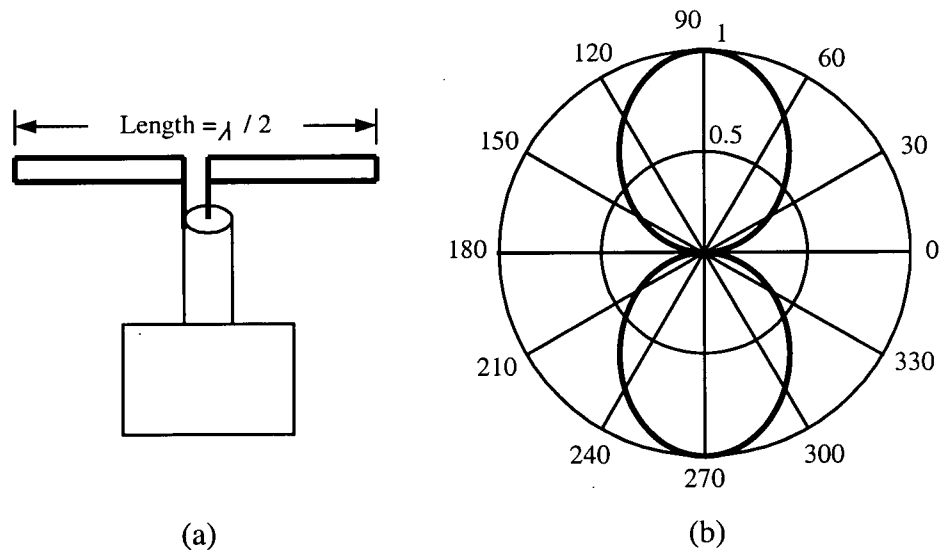


Figure 4.1 (a) Configuration and (b) Antenna Pattern, of a Half Wave Dipole Antenna

4.3 Spatial and Temporal Processing Concepts

The trend of the wireless cellular system evolution is heading for more user channels and higher system capacity. The developments in the antenna technology are essentially aiming for the same ultimate goal: allowing more users to access the wireless networks. The spatial and temporal processing based on the spatial and temporal characteristics of the transmission channel is a significant advancement in the antenna design to improve

the signal quality against interference and noise.

4.3.1 Antenna Arrays and Wave Fronts Arrivals

The concept of antenna arrays is originated from a military context and designed to perform direction finding and to null out enemy interferers for the operation of radar and satellite communication systems. In wireless system applications, antenna arrays are used to reduce transmission errors by maximizing the SINR of the received signals [3][37]. An antenna array consists of a group of spatially distributed omni-directional antenna receivers, whose operation and timing are usually controlled by one central processor. The output of the antenna array is obtained by combining each antenna output with the central processor to extract the desired signal from all received signals even if the same frequency band is occupied by all user signals as in WCDMA.

Antenna arrays can exploit the spatial dynamics of impinging wave fronts to increase the overall gain and make use of the constructive waves of each antenna element to create desired radiation patterns. In theory, the use of an antenna array containing M antenna elements can provide a mean power gain of M over AWGN, but the extent of suppressing MAI's from other users depends on the form of the received data that will be described later in the chapter [37].

Furthermore, the performance enhancement attainable with an antenna array depends heavily on the array geometry and the spatial radio environment. In rural locations received signals have well defined directions of arrival and low angular spreads while urban surroundings are on the contrary. No antenna architecture will provide an optimum solution to all environments and the choice of the antenna topology should

reflect the differences of these ambiances. The linear array geometry, a common configuration with antenna elements linearly spaced along a straight line, is assumed for simulations in this thesis as found in [3][9].

Consider the wave front of the k^{th} multipath component arriving at an angle θ_k at an antenna array of M antenna elements equally spaced at one half wavelengths apart as shown in Figure 4.2. Disregarding the fading effects due to the transmission channel at this stage, the wave front in the carrier frequency band intercepted by the m^{th} antenna of the array in Figure 4.2 can be defined in a complex value as

$$FR_{m,k}(t) = a_k(t) \exp[j(2\pi f_c t + \eta_{m,k}(t))] s(t) \quad (4.3)$$

where $a_k(t)$ is the amplitude of the impinging wave front, $\eta_{m,k}(t)$ is a relative signal phase encountered by the m^{th} antenna due to the impinging angle $\theta_k(t)$ of the k^{th} multipath component, f_c is the carrier frequency, $s(t)$ is the original bit transmitted, and $m = 0, 1, \dots, M-1$ [18]. Assuming perfect carrier recovery, the received signal after removing the carrier and passing through the pulse matching filter becomes

$$r_{m,k}(t) = a_k(t) \exp[j\eta_{m,k}(t)] s(t) . \quad (4.4)$$

As a wave front propagates through the antenna array, each antenna element receives a phase-shifted version of the signal compared to a reference point, antenna element 0 in this case as shown in Figure 4.2. This relative phase shift for the m^{th} antenna element for the k^{th} multipath component can be associated with the distance between the m^{th} sensor and the wave front encroaching antenna element 0, which is described as $d_{m,k}(t)$

in Figure 4.2. From the geometry, $d_{m,k}(t)$ can be mathematically represented as

$$d_{m,k}(t) = [m\lambda \sin \theta_k(t)] / 2 . \quad (4.5)$$

Since a distance of λ corresponds to a phase shift of 2π of the incoming wave, the phase difference, $\eta_{m,k}(t)$, resulted by the path difference between the reference antenna element 0 and the m^{th} antenna for this k^{th} multipath component is

$$\eta_{m,k}(t) = \frac{2\pi d_{m,k}(t)}{\lambda} = m\pi \sin \theta_k(t) \quad (4.6)$$

by substituting $d_{m,k}(t)$ with Equation 4.5. For $\eta_{0,k}(t)$ being the reference point, $\eta_{0,k}(t)$ has a value of 0. After substituting Equation 4.6 into Equation 4.4, the received signal at the m^{th} antenna can be rewritten as

$$r_{m,k}(t) = a_k(t) \exp[jm\pi \sin \theta_k(t)] s(t) . \quad (4.7)$$

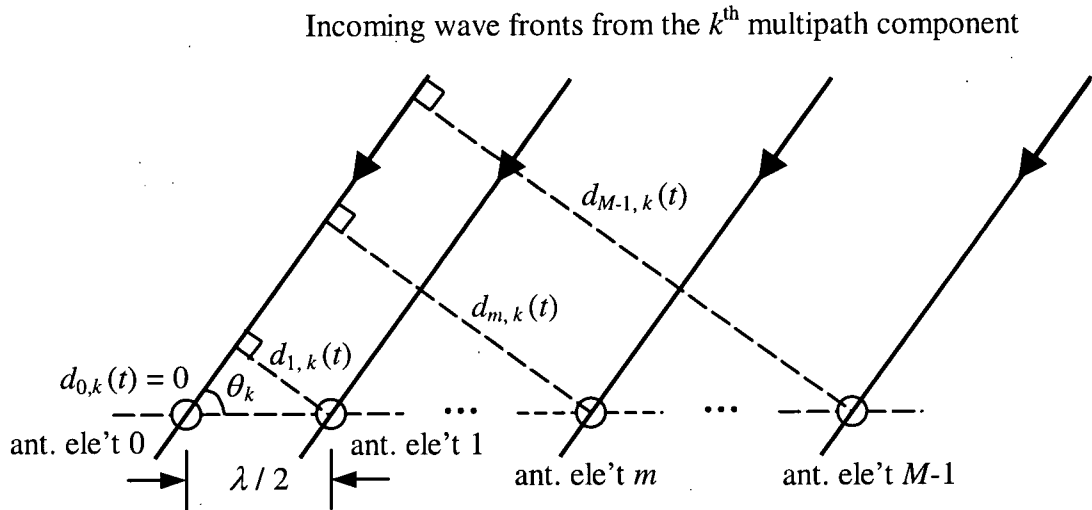


Figure 4.2 A Linear Equally Spaced Antenna Array of M Antenna Elements Receiving a Plane of Wave Fronts of the k^{th} Multipath Component from Direction $\theta_k(t)$

The overall channel impulse response due to path loss, multipath fading, and Rayleigh fading for the k^{th} multipath component, $L_k(t)$, has been previously defined in Equation 3.18. The relative phase variations introduced by the position of the m^{th} antenna element, $\eta_{m,k}(t)$, can be incorporated into the channel impulse response. Therefore, $L_{m,k}(t)$, the channel impulse response observed from the m^{th} antenna element for the k^{th} multipath component can be expressed as

$$\begin{aligned} L_{m,k}(t) &= L_{\text{path}} \alpha_k(t) \beta_k(t) \exp[j\zeta_k(t)] \exp[j\phi_k(t)] \exp[j\eta_{m,k}(t)] \\ &= a_k(t) \exp[j\phi_k(t)] \exp[j\eta_{m,k}(t)] \end{aligned} \quad (4.8)$$

where $a_k(t) = \alpha_k(t) \beta_k(t)$ and $\exp[j\phi_k(t)]$ are the amplitude and phase of the k^{th} multipath component due to path loss, multipath fading, and Rayleigh fading.

4.3.2 Antenna Patterns of Linear Antenna Arrays

As the total width of the linear array increases, the main lobe of the antenna pattern becomes narrower, which can be used to reduce interferers. Furthermore, by increasing the number of antenna elements in the antenna array, the side lobes become smaller. As an example, Figure 4.3 illustrates the antenna patterns of four different configurations of a linear antenna array composed of omni-directional antennas [37]. Figure 4.3(a) shows the antenna pattern of a four-element antenna array spaced at $\lambda/2$ apart for a total array width of $3\lambda/2$. The antenna pattern has a narrow central beam with the highest field strength, which is referred to as the main lobe, and several small beams on either side of the central beam, which are called side lobes. Directions with zero field strength are referred to as nulls.

For comparison, Figures 4.3(b) and 4.3(c) illustrate the antenna patterns of a four-element array spaced at λ apart and a seven-element array spaced at $\lambda/2$ apart for a total width of 3λ for both arrays. In general, the total width of the linear array determines the maximum gain that the array can achieve while the number of antenna elements decides the number of degrees of freedom that one has in designed array patterns. If the antenna element spacing exceeds $\lambda/2$ in a linear array, undesired side lobes will appear as seen in Figure 4.3(b), which in turn will amplify noise or interference.

By changing the signal phases of the antenna elements in the array, the main lobe can be steered towards certain directions as opposed to a fixed direction at ninety degrees when all signal phases are the same. One simple way to vary the signal phases of each antenna element is to change the feed cable length to shift phases by transmission delays but this method would set the antenna array to service a permanent direction. Another technique is to alter the signal phases fed to each antenna element with programmable electronic phase shifters so that the main lobe can be steered dynamically. The controller can decide which direction the antenna will be steered to using the programmable electronic phase shifters. Figure 4.3(d) shows an eight-element linear array spaced at $\lambda/2$ apart with a progress phase shift of 0.7π per antenna element from a phase shift of 0π at antenna element 0 to 4.9π at the eighth antenna element as seen in the figure. The main lobe of the resultant antenna pattern is steered about forty-five degrees to the left compared to the equal phase linear array.

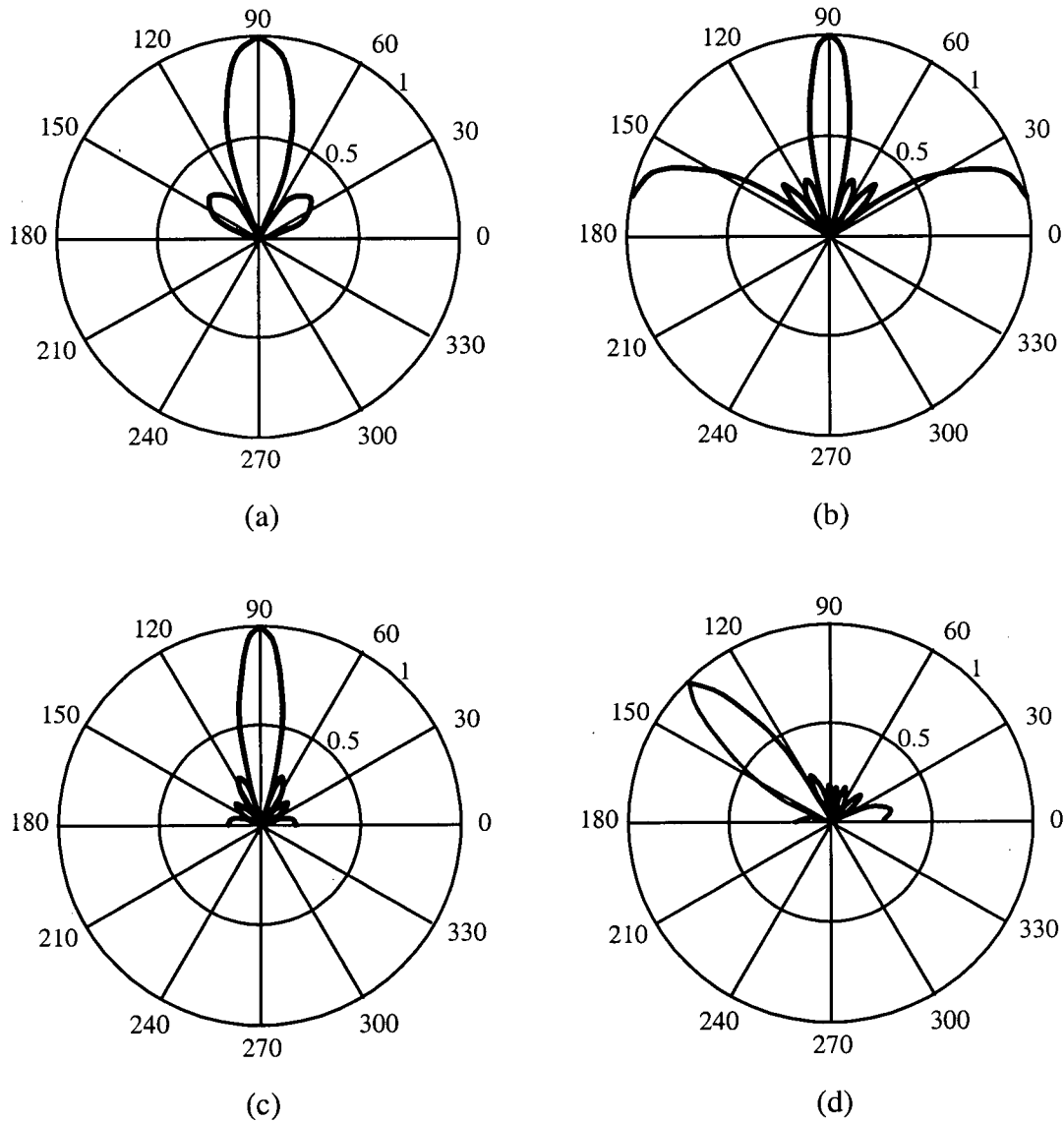


Figure 4.3 Antenna Patterns of Antenna Arrays with (a) 4 Antenna Elements Spaced at $\lambda/2$ apart, (b) 4 Antenna Elements Spaced at λ apart, (c) 7 Antenna Elements Spaced at $\lambda/2$ apart, and (d) 7 Electronically Steered Antenna Elements Spaced at $\lambda/2$ apart

Being able to steer the main lobe of the antenna pattern to a certain direction dynamically is a very significant advancement in antenna array technologies. It allows the antenna array to only receive or transmit in the direction of the desired user, and thus reduces the MAI's generated by other undesired users from other directions. The

technique to steer antenna main lobes by varying the signal phases of each antenna element leads to development of smart antenna arrays which will be described later in this chapter.

4.3.3 Temporal Processing with Rake Fingers and Two Dimensional Receivers

The spatial aspects of wave fronts and antennas have been discussed in the previous sections. The temporal characteristics of the channel can be taken advantage of as well by receiving antennas. The model of a multipath channel has been presented in Section 3.4. Propagation delay spreads in the channel provide multiple versions of the transmitted signal at the receiver, which in turn cause ISI and performance degradation. However, there is useful information in the multipath components that can be extracted by the receiver.

The idea of a Rake receiver was first proposed by Price and Green based on the low autocorrelation properties of a spreading sequence used in spread spectrum systems [24]. The function of the Rake receiver is to collect the time shifted versions of the original signal by providing a separate finger for each of the multipath components. Each finger is locked to a different time delay with a correlator. The time diversity is provided for the fact that the multipath components are uncorrelated to each other when the relative propagation delays exceed a chip period.

A Rake receiver with Y fingers will be able to detect Y strongest multipath components out of the total K components by estimating time delays for each of the fingers. Finger 0 is synchronized to the first arriving multipath component with a delay of τ_0 , and the path with a delay τ_1 is matched in time by finger 1, τ_1 by finger 2, etc.

The delayed signals are multiplied with a weight coefficient. Weight assignments will be discussed in Section 4.4.1. For a conventional receiver with a single correlator, if the output of the correlator is corrupted by fading, the decoded message may have a large bit error rate. With a Rake receiver, the outputs of all of the fingers will be summed together to overcome fading of an individual path [33]. Figure 4.4 shows a tapped delay line Rake receiver model with one antenna element and Y fingers and a weight vector for each finger. The model shown in Figure 4.4 will be incorporated with the data operations of the network transport and physical layers as described in Chapter 5.

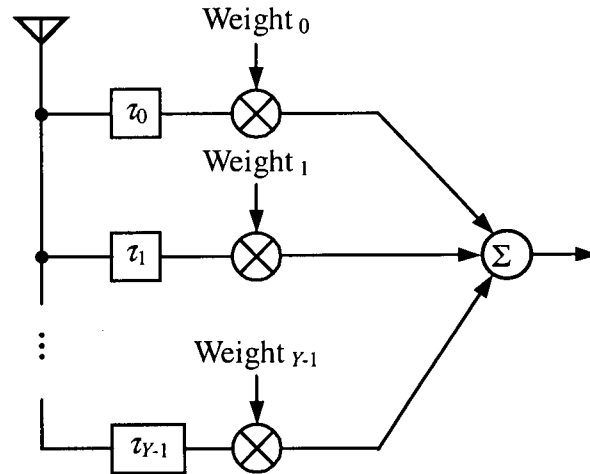


Figure 4.4 An One Antenna Element Tapped Delay Line Rake Receiver Model

By combining the spatial and temporal concepts, a 2D antenna array would be able to make use of the attributes in both the spatial and temporal dimensions that have been discussed previously. The 2D receiver exploits any structure that might be present in the transmission channel such as the AOA's and ISI of the multipath components, their Doppler frequencies, and the MAI's [9]. The diagram of a 2D $M \times Y$ antenna array model along with weight assignments is illustrated in Figure 4.5 in Section 4.4.1.

4.4 Smart Antenna Technologies

The weight vector assignment describes how the 2D signals are combined together to improve signal qualities using various signal processing techniques. Since the radiation patterns of the antenna array can be adaptively controlled with software by the weight vectors to enhance the desired signal strengths or diminish interfering signals, the antenna array system is also referred to as a smart antenna. The use of smart antenna technologies provides enhanced coverage, reduced structural costs, enhanced link performance and increased system capacity. In this section, the smart antenna technologies implemented for the WCDMA simulator will be described in detail.

4.4.1 Weight Vector Assignment

Each weight element in Figure 4.4 has a magnitude and a phase associated with it, and can be represented as a complex number with a real and an imaginary part. For the purpose of displaying the weight elements for an array, it is convenient to show them in vector notation as

$$\mathbf{w}_y = [w_{0,y} \ w_{1,y} \ \dots \ w_{M-1,y}]^T \quad (4.9)$$

where \mathbf{w}_y is the weight vector for the y^{th} finger, $w_{0,y} \ w_{1,y} \ \dots \ w_{M-1,y}$ represent the weights for the M antenna elements of the y^{th} finger, and the superscript T denotes a transposition. The received signal vector of the M -element antenna array for the y^{th} finger is described by

$$\mathbf{r}_y = [r_{0,y} \ r_{1,y} \ \dots \ r_{M-1,y}]^T \quad (4.10)$$

where \mathbf{r}_y is the received signal vector for the y^{th} finger, $r_{0,y} \ r_{1,y} \dots r_{M-1,y}$ represent the received signals for the M antenna elements of the y^{th} finger. The output, z_y , is the sum of the weighted signals of the y^{th} finger and can be expressed by [38]

$$z_y = \mathbf{w}_y^H \mathbf{r}_y \quad (4.11)$$

$$= \begin{bmatrix} w_{0,y}^* & w_{1,y}^* & \dots & w_{M-1,y}^* \end{bmatrix} \begin{bmatrix} r_{0,y} \\ r_{1,y} \\ \vdots \\ r_{M-1,y} \end{bmatrix}$$

where the superscript H denotes the Hermitian transpose, which is a transposition combined with complex conjugation, and $*$ denotes the complex conjugate.

Figure 4.5 illustrates the conceptual block diagram of a 2D antenna array system with each of the antenna elements attached to a tapped delay line Rake receiver model as shown in Figure 4.4. In this system, there are M antenna elements in the antenna array with each having Y fingers. Therefore this system is considered as an $M \times Y$ model and there are $M \times Y$ corresponding weights to process $M \times Y$ space-time separated data samples. This system will be integrated with other data operations in Chapter 5.

The antenna array has to process a number of time delayed versions of the desired signal, each of which is corrupted by undesired MAI's and ISI's from various delays as well as noises. With the use of an antenna array and a weight vector network, it is possible to steer the main lobe of the receiver towards the direction of the transmitter to focus the gain at a desired angle and null interferences in all other directions. However, this approach is hampered by the large number of users in the WCDMA system, which

consequently produces interferences from all angles possibly including the direction of the desired signal [3]. Optimum combining techniques involve weighting each of the $M \times Y$ data samples appropriately and combine them together before making a data decision [9]. The degree of improvement of SINR completely depends on how the weight vector network is manipulated as well as how severely the desired signal is affected by interferers.

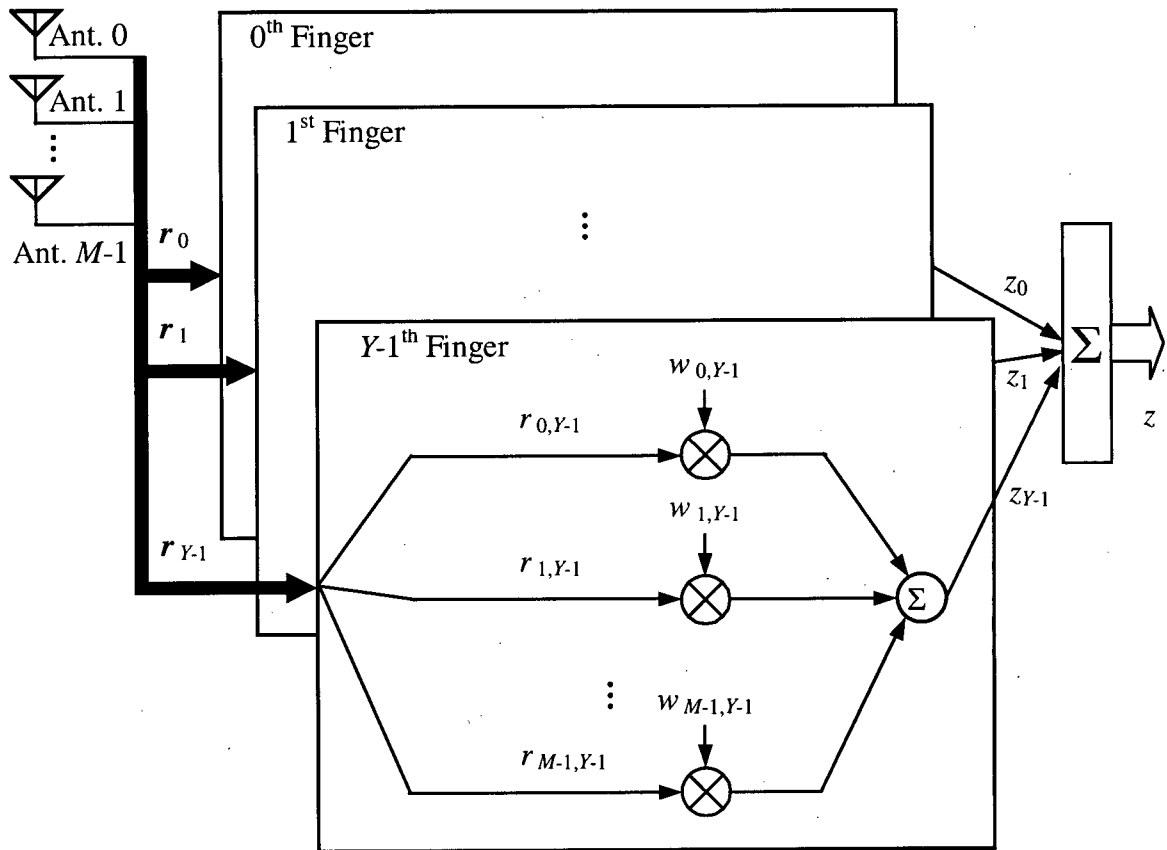


Figure 4.5 A 2D $M \times Y$ Antenna Array Model with Weight Assignments

4.4.2 Equal Gain Combining and Maximal Ratio Combining Antennas

Two smart antenna methods, namely Equal Gain Combining (EGC) and MRC

antennas [14], which would improve the SNR at the receiver, are discussed in this section. These two methods are designed to combine the signals of different antenna branches in antenna arrays by defining the weight vector assignments of the 2D antenna array system. The term “combining” actually represents several operations, including setting up the weight vectors using a particular method, multiplying the received signals with the weights, and summing all the modified signals together.

In the EGC antenna scheme, the weight vector is set to steer the main lobe of the antenna array towards the direction of arrival of the desired signal. Incorporating MAI, ISI and AWGN into the previously defined Equations 4.6 to 4.8, a signal received at the m^{th} antenna element and the y^{th} finger that is matched to the k^{th} multipath component is described by

$$\begin{aligned} r_{m,y}(t) &= a_y(t) \exp[j\phi_y(t)] \exp[j\eta_{m,y}(t)] s(t) + u_{m,y}(t) + \mathbf{N}(t) \\ &= L_{m,y}(t) s(t) + u_{m,y}(t) + \mathbf{N}(t) \end{aligned} \quad (4.12)$$

where $\mathbf{N}(t)$ is the AWGN, and $u_{m,y}(t)$ represents the ISI and MAI in the channel that will be discussed in detail in Section 5.2.2. To employ EGC, the main lobe of the antenna pattern would be steered by multiplying the received signal with $\exp[-j\phi_y(t)] \exp[-j\eta_{m,y}(t)]$ to cancel the phase incurred due to the transmission channel [13]. Thus, based on Equation 4.11, the weight $w_{m,y}$ for the m^{th} antenna element of the y^{th} finger should be set as

$$w_{m,y}(t) \Big|_{\text{EGC}} = \exp[j\phi_y(t)] \exp[j\eta_{m,y}(t)] . \quad (4.13)$$

Multiplying the received signal in Equation 4.12 with the weight in Equation 4.13 would

yield an amplitude of $a_y(t)s(t) + u'_{m,y}(t) + \mathbf{N}(t)$. If the received signal is to be multiplied with another weight with a different phase due to estimation errors, the resulted amplitude would be less than the maximum possible $a_y(t)$. For EGC, the weight is essentially set to the conjugate of the estimate of the channel phase distortion of the signal. The multiplication cancels out the unwanted phase to yield a coherent signal.

For MRC, the channel impulse response including the amplitude and the phase is estimated from the antenna signal. By perfectly estimating the overall impulse response $L_{m,y}(t)$, the phase angle distortions due to the propagation channel can be compensated, and the signal can be weighted proportionally to the SNR of the data sample [14]. According to Equation 4.11, the weight in MRC would be set as

$$\begin{aligned} w_{m,y}(t) \Big|_{\text{MRC}} &= L_{m,y}(t) \\ &= a_y(t) \exp[j\phi_y(t)] \exp[j\eta_{m,y}(t)] \end{aligned} \quad (4.14)$$

which is the complex conjugate of the channel impulse response. By multiplying the weight in Equation 4.14 and the received signal in Equation 4.12, the MRC output becomes $a_y^2(t)s(t) + u'_{m,y}(t) + \mathbf{N}(t)$.

EGC and MRC are based on the matched filter concept for maximizing signal gains. Essentially, these two methods undo the phase rotation of the signals caused by the channel by rotating back the signals to the transmitted phase. For signals with line of sight, EGC and MRC schemes both give the same optimal SNR result if the direction of arrival of the desired signal is known for EGC and the channel impulse response is known for MRC. Both cases depend on the accuracy of estimating the arriving angle

and the channel parameters using pilot signals available. The relative performance between the EGC and MRC schemes changes as the number of antenna elements increases since the MRC scheme suffers from higher estimation errors than the EGC scheme [20].

4.4.3 Inference Rejection Combining Antennas

The two EGC and MRC combining schemes are designed to improve the SNR of the signal reception. However, from the receiver performance and system capacity points of view, WCDMA systems are interference limited. When the number of users in the system is large, raising the SNR of the signals will yield no significant improvement in the BER. Only by increasing the SINR using adaptive antenna algorithms using the IRC antennas as described in this section would improve overall system performance [38].

In the IRC scheme, the computation of a correlation function using the received antenna signal samples is required in order to determine the correcting factors for weight assignments. This correlation function will describe the correlation between the signals received from the M antenna elements, and therefore it is necessary to use the vector notations \mathbf{w}_y and \mathbf{r}_y previously defined in Equations 4.9 and 4.10. Assume that there will be B discrete time samples collected by the antenna to compute the correlation function. The b^{th} discrete time sample received at the y^{th} finger out of the total B samples can then be presented as

$$\begin{aligned} \mathbf{r}_y(b) &= \mathbf{L}_y(b)s(b) + \mathbf{u}_y(b) + \mathbf{\kappa}(b) \\ \mathbf{u}_y(b) &= \mathbf{r}_y(b) - \mathbf{L}_y(b)s(b) - \mathbf{\kappa}(b) \end{aligned} \tag{4.15}$$

where $L_y(b)$ and $u_y(b)$, taking the same format as $r_y(b)$, are vectors of size M of the same symbols defined in Equation 4.12. The spatial covariance matrix R_{r_y} , a measure of the correlation between the antenna elements, is a symmetric matrix of cross correlations and autocorrelations of the received signals. Thus, R_{r_y} represents the spatial covariance matrix between the M antenna elements of the y^{th} multipath component intercepted at the receivers and can be defined as [38]

$$R_{r_y} \triangleq E[r_y(b) r_y^H(b)] \quad (4.16)$$

where $E[\cdot]$ denotes the statistical expectation. Similarly, the spatial covariance matrix of the undesired interferences between the M antenna elements is defined as

$$R_{uu_y} \triangleq E[u_y(b) u_y^H(b)]. \quad (4.17)$$

After defining the spatial covariance matrix of the undesired interference, the IRC weight assignment that produces the optimal weighted output, $z_y(b)$, can be determined by examining the log likelihood function between the received signal r_y and the desired signal s . Assuming that s has equal probability between its possible values, this log likelihood function is presented as [13]

$$\begin{aligned} LH(r_y, s) &= \ln \left\{ \prod_{b=1}^B \frac{1}{\pi^M \det[R_{uu_y}]} \exp[-u_y(b) R_{uu_y}^{-1} u_y^H(b)] \right\} \\ &= - \sum_{b=1}^B [r_y(b) - L_y(b)s(b)]^H R_{uu_y}^{-1} [r_y(b) - L_y(b)s(b)] + \text{const} \end{aligned} \quad (4.18)$$

where $\det[\cdot]$ indicates the determinant of the matrix. In Equation 4.18, the

interferences have been assumed to be Gaussian distributed, which is valid for spread spectrum signals that have a SF of 20 or more in the spreading code [13][36], i.e. the voice, low-rate, and medium-rate data users. Since the users chosen for this thesis would have SF's of 32 and 128, this would be a suitable assumption here.

By making another assumption that all possible values of s have equal energy, Equation 4.18 can be reduced to

$$\begin{aligned}
 LH[\mathbf{r}_y, s] &= \sum_{b=1}^B 2 \operatorname{Re} [\mathbf{r}_y^H(b) \mathbf{R}_{uu_y}^{-1} \mathbf{L}_y(b) s(b)] + \text{const} \\
 &= 2 \operatorname{Re} \sum_{b=1}^B \{ [\mathbf{r}_y(b) \mathbf{w}_y^H(b)] s^*(b) \} + \text{const} \\
 &= 2 \operatorname{Re} \sum_{b=1}^B [z_y(b) s^*(b)]
 \end{aligned} \tag{4.19}$$

where the optimal output $z_y(b) = \mathbf{r}_y(b) \mathbf{w}_y^H(b)$ of the likelihood function is obtained by setting the weight vector $\mathbf{w}_y(b)$ of the IRC antenna to be [38]

$$\mathbf{w}_y(b) \Big|_{\text{IRC}} = \mathbf{R}_{uu_y}^{-1} \mathbf{L}_y(b) \quad . \tag{4.20}$$

as demonstrated in Equation 4.19. By comparing the MRC scheme derived in Equation 4.14 with the IRC weight function shown in Equation 4.18, it is evident that the MRC receiver is a special case of the IRC receiver given by replacing the spatial covariance matrix \mathbf{R}_{uu_y} , the correcting factor in Equation 4.18, with an identity matrix.

4.4.4 Parameter Estimation for MRC and IRC Demodulators

With the pilot signals provided in WCDMA systems, it is possible to estimate the

parameters including the channel state $L_y(b)$ and the spatial covariance matrix R_{uu_y} that are required in the MRC and IRC algorithms for computing the corresponding weight vectors $w_y(b)$. Thus, in this thesis, these two parameters $L_y(b)$ and R_{uu_y} are estimated by the receiver using the pilot signals rather than made known to the receiver, to reflect the real situation in wireless transmissions.

Assuming that there is no a priori information about the spatial structure of $L_y(b)$ and R_{uu_y} , these two parameters are estimated from B samples of the pilot signals $s(b)$ and the received signals $r_y(b)$. It is also assumed that the channel state does not change during the estimation period. The ML estimates of $[\hat{L}_y, \hat{R}_{uu_y}]$ is the joint minimum of the log likelihood function

$$\begin{aligned}
 LH[r_y; L_y, R_{uu_y}] &= \ln \left\{ \prod_{b=1}^B \frac{1}{\pi^M \det[R_{uu_y}]} \right. \\
 &\quad \left. \exp \left\{ -[r_y(b) - L_y(b)s(b)] R_{uu_y}^{-1} [r_y(b) - L_y(b)s(b)]^H \right\} \right\} \quad (4.21) \\
 &= -\ln \left\{ \det[R_{uu_y}^{-1}] \right\} - \text{trace} \left\{ R_{uu_y} \frac{1}{B} \sum_{b=1}^B [r_y(b) - L_y(b)s(b)] \right\} + \text{const}.
 \end{aligned}$$

Consider the first estimate of \hat{R}_{uu_y} and the unstructured estimate of \hat{L}_y , \hat{R}_{uu_y} is obtained by [11] as

$$\hat{R}_{uu_y} = \frac{1}{B} \sum_{b=1}^B [r_y(b) - L_y(b)s(b)][r_y(b) - L_y(b)s(b)]^H. \quad (4.22)$$

Then \hat{L}_y can be obtained by minimizing the cost function

$$F_{\text{cost}} = \det \left\{ \frac{1}{B} \sum_{b=1}^B [\mathbf{r}_y(b) - \mathbf{L}_y(b)s(b)][\mathbf{r}_y(b) - \mathbf{L}_y(b)s(b)]^H \right\}. \quad (4.23)$$

which is accomplished by minimizing the function inside the determinant. Let

$F_{\text{cost}} = \det[\mathbf{G}_{\text{cost}}]$ so that \mathbf{G}_{cost} becomes [13]

$$\begin{aligned} \mathbf{G}_{\text{cost}} &= \frac{1}{B} \sum_{b=1}^B [\mathbf{r}_y(b) - \mathbf{L}_y(b)s(b)][\mathbf{r}_y(b) - \mathbf{L}_y(b)s(b)]^H \\ &= \hat{\mathbf{R}}_{\mathbf{r}_y} + \mathbf{L}_y(b)\mathbf{L}_y^H(b) - \mathbf{L}_y(b)\hat{\mathbf{X}}_{s\mathbf{r}_y} - \mathbf{L}_y^H(b)\hat{\mathbf{X}}_{s\mathbf{r}_y}^H \\ &= \mathbf{L}_y(b)\mathbf{L}_y^H(b) - \mathbf{L}_y(b)\hat{\mathbf{X}}_{s\mathbf{r}_y} - \mathbf{L}_y^H(b)\hat{\mathbf{X}}_{s\mathbf{r}_y}^H + \hat{\mathbf{X}}_{s\mathbf{r}_y}^H \hat{\mathbf{X}}_{s\mathbf{r}_y} + \hat{\mathbf{R}}_{\mathbf{r}_y} - \hat{\mathbf{X}}_{s\mathbf{r}_y}^H \hat{\mathbf{X}}_{s\mathbf{r}_y} \\ &= [\mathbf{L}_y(b) - \hat{\mathbf{X}}_{s\mathbf{r}_y}^H][\mathbf{L}_y(b) - \hat{\mathbf{X}}_{s\mathbf{r}_y}^H]^H + \hat{\mathbf{R}}_{\mathbf{r}_y} - \hat{\mathbf{X}}_{s\mathbf{r}_y}^H \hat{\mathbf{X}}_{s\mathbf{r}_y} \end{aligned} \quad (4.24)$$

where $\hat{\mathbf{X}}_{s\mathbf{r}_y}$ is the cross correlation function between the antenna signal vector $\mathbf{r}_y(b)$ and the pilot signals $s(b)$ and is given by

$$\hat{\mathbf{X}}_{s\mathbf{r}_y} = \frac{1}{B} \sum_{b=1}^B s^*(b)\mathbf{r}_y(b). \quad (4.25)$$

Also, $\hat{\mathbf{R}}_{\mathbf{r}_y}$ can be mathematically expressed as

$$\hat{\mathbf{R}}_{\mathbf{r}_y} = \frac{1}{B} \sum_{b=1}^B \mathbf{r}_y(b)\mathbf{r}_y^H(b). \quad (4.26)$$

Since the second and third terms in Equation 4.24 do not depend on $\hat{\mathbf{L}}_y$, the cost function

\mathbf{G}_{cost} is minimized by choosing $\hat{\mathbf{L}}_y$ to be

$$\begin{aligned} \hat{\mathbf{L}}_y &= \hat{\mathbf{X}}_{s\mathbf{r}_y}^H \\ &= \frac{1}{B} \sum_{b=1}^B s(b)\mathbf{r}_y^H(b). \end{aligned} \quad (4.27)$$

Because the whole sample covariance matrix \mathbf{G}_{cost} is minimized by choosing $\hat{\mathbf{L}}_y$ in

Equation 4.29, this estimate of $\hat{\mathbf{L}}_y$ will minimize any non-decreasing function of G_{cost} . A function $f(G_{cost})$ is non-decreasing of positive definite G_{cost} if for any non-negative definite ΔG_{cost} , $f(G_{cost} + \Delta G_{cost}) \geq f(G_{cost})$, and the equality holds only for $\Delta G_{cost} = 0$ [11]. Therefore the determinant of G_{cost} , which is F_{cost} as defined in Equation 4.25 and a non-decreasing function of G_{cost} , is minimized by $\hat{\mathbf{L}}_y$. Therefore, the weights defined in Equations 4.14 and 4.20 for the MRC and IRC schemes can be estimated based on the $\hat{\mathbf{L}}_y$ and $\hat{\mathbf{R}}_{uu_y}$ defined in Equations 4.27 and 4.22 calculated from the pilot signals and received signals.

4.5 Conclusions

In this chapter, the antenna technologies implemented for the software simulator for this thesis have been introduced. Section 4.2 discusses the basic concepts of antenna characteristics and antenna radiation patterns. In Section 4.3, the spatial and temporal processing taking place at an antenna array has been explained. For the spatial processing, the forms of the wave fronts arriving at an array of antenna elements are defined, and the effects that the different configurations of an antenna array have on the radiation patterns are described. For temporal processing, a Rake receiver that is capable of capturing multipath signals with various delays as well as a 2D receiver model have been presented. Section 4.4 describes the smart antenna algorithms used to compute the antenna weights. Specifically, the MRC and IRC schemes have been discussed, and the algorithms for estimating the parameters required based on the received pilot signals have also been explained.

CHAPTER 5 THE WCDMA SYSTEM SIMULATOR

5.1 Introduction

The major components of the WCDMA transmission simulator have been laid out in detail in the previous chapters. By interconnecting each of these components, a chip level WCDMA transmission simulator is formed. The WCDMA transmission simulator implemented for the research in this thesis is designed to investigate how the overall system performance and capacity will be affected by various system parameters, as it will be shown in Chapter 6. Since the WCDMA system capacity is interference-limited by the uplink traffic as concluded in [39][40][41], only the uplink path traffic will be considered for simulations in this thesis. This chapter is organized as follows. Section 5.2 presents the overall uplink path model that includes the transmitter, transmission channel, and receiver sub-models. Section 5.3 describes the system methodology including the preliminary set up stage, power control steps, and simulation run stage. Finally, the conclusions of the chapter are presented in Section 5.4.

5.2 The Overall Uplink Path Modeling

The WCDMA simulator is composed of the WCDMA physical layer model, the transmission channel model, and the antenna model. These models are merged together to construct the transmitter and receiver models for the uplink direction.

5.2.1 Uplink Transmitter Model

Data encoding and modulating operations for the transport network layer and the

physical layer are described in Chapter 2. The data operation at the transport network layer is simplified to comprise only the transport channel encoder, which could be either the convolutional encoder or the turbo encoder. The data formation for the physical layer is composed of the spreading and scrambling operations. The data encoding and modulating processes at the transmitter end are shown in Figure 5.1.

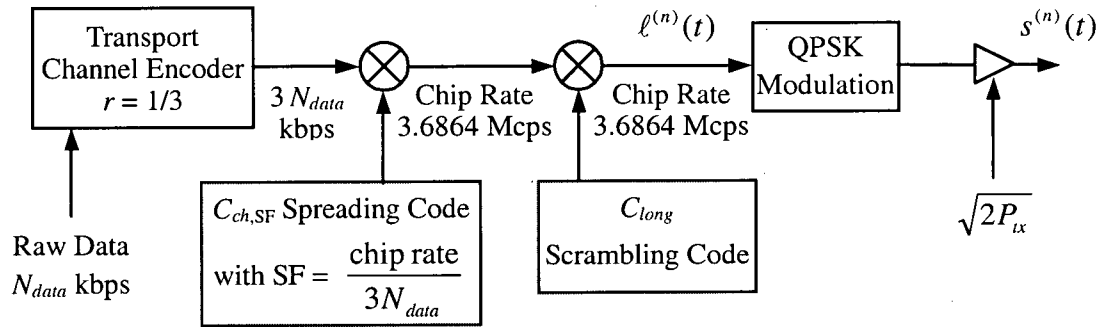


Figure 5.1 Encoding and Modulating Processes before Transmission

$s^{(n)}(t)$ in Figure 5.1 is the transmitted RF signals for the n^{th} user, and it can be represented by $s^{(n)}(t) = s_I^{(n)}(t) - s_Q^{(n)}(t)$ where

$$\begin{aligned} s_I^{(n)}(t) &= \sqrt{2P_{tx}} \sum_{i=-\infty}^{\infty} \ell_I^{(n)}(t) g_r(t - iT_{chip}) \cos(2\pi f_c t) \\ s_Q^{(n)}(t) &= \sqrt{2P_{tx}} \sum_{i=-\infty}^{\infty} \ell_Q^{(n)}(t) g_r(t - iT_{chip}) \sin(2\pi f_c t) \end{aligned} \quad (5.1)$$

In Equation 5.1, the superscript (n) means the n^{th} user, $s_I^{(n)}(t)$ and $s_Q^{(n)}(t)$ indicate the in-phase and quadrature components of $s^{(n)}(t)$, $\ell^{(n)}(t) = \ell_I^{(n)}(t) + j\ell_Q^{(n)}(t)$ are the in-phase and quadrature components of the outputs after the transport channel coding, spreading and scrambling operations, $g_r(t)$ is the impulse response of the pulse shaping

filter, and T_{chip} is the chip duration. P_{tx} is the average transmitted power and can be expressed by

$$P_{tx} = \frac{E_b}{T_b} \quad (5.2)$$

where E_b is the bit energy and T_b is the bit duration. The transmitted signals in Equation 5.1 are then sent to the uplink transmission channel model described in Section 5.2.2 where they will be further processed.

5.2.2 Uplink Transmission Channel Model

The transmission channel model illustrates the effects on the transmitted signals due to radio wave propagation environments. Thus the received signals at the receiver end are replicated with the transmitted signals multiplied by the variables in the transmission channel model. These variables include the Hata fading parameter due to large scale propagation, and the Rayleigh fading and multipath fading parameters due to small scale propagation from a frequency selective slow fading environment. Moreover, with the implementation of antenna arrays at the receiver end, the received signals at each of the antenna elements are subject to further phase variations. This transmission channel model is devised based on a receiver array with M elements and Y Rake fingers to exploit the spatial and temporal diversities of the channel. The multipath environment is simulated with the Hashemi model described in Section 3.5.1.

Since only the baseband is considered for this thesis, the analog RF part will be omitted in the equations of the signals hereafter, and the signals will be assumed to be downconverted to the baseband with the effect of receiver filters disregarded. For

multipath uplink transmission, the transmitter is the MS antenna, and the receiver would be the antenna structured on top of the BS's. With the two-dimensional spatial-temporal receiver structure, an equivalent complex baseband representation of the received signals at the m^{th} antenna element with K multipaths and a total of N users in the system can be modeled as

$$r_m(t) = \sum_{n=0}^{N-1} \sum_{k=0}^{K-1} L_{m,k}^{(n)}[t - \tau_k^{(n)}(t)] \ell^{(n)}[t - \tau_k^{(n)}(t)] \exp\{j\psi_{m,k}^{(n)}[t - \tau_k^{(n)}(t)]\} + \mathfrak{N}(t) \quad (5.3)$$

where $L_{m,k}^{(n)}[t - \tau_k^{(n)}(t)]$ is the overall impulse response of the transmission channel defined in Equation 4.8, $\exp\{j\psi_{m,k}^{(n)}[t - \tau_k^{(n)}(t)]\}$ is the carrier phase offset, and both are offset by the multipath delay $\tau_k^{(n)}(t)$ as described in Section 3.5.1 [42]. Equation 5.3 represents the received signal as the sum of signals coming from N users with each user having K multipaths.

When calculating the antenna weights using the smart antenna algorithms, the received signals will be modeled in two parts: the desired signals and the undesired signals. The desired signals are the signals coming from the desired user on the path of the multipaths being considered. The undesired signals can be further separated into the ISI's which are the self-interference due to the undesired multipaths of the desired user, the MAI's due to the multipaths of the undesired users, and AWGN in the channel. Therefore by examining the sum of signals defined in Equation 5.3 individually, the received signals for the x^{th} desired user at the m^{th} antenna element and the y^{th} finger, which is time matched to the k^{th} multipath component, could also be written as

$$r_{m,y}^{(x)}(t) = DS_{m,y}^{(x)}(t) + US_{m,y}^{(x)}(t) + UM_{m,y}^{(x)}(t) + \mathfrak{N}(t) \quad (5.4)$$

where $DS_{m,y}^{(x)}(t)$, $US_{m,y}^{(x)}(t)$, and $UM_{m,y}^{(x)}(t)$ represents the desired signals, the undesired ISI's, and the undesired MAI's, respectively. $DS_{m,y}^{(x)}(t)$ for the y^{th} finger of the x^{th} desired user received at the m^{th} antenna element would then be mathematically expressed by

$$DS_{m,y}^{(x)}(t) = L_{m,y}^{(x)}(t) \ell^{(x)}(t) \exp[j\psi_{m,y}^{(x)}(t)]. \quad (5.5)$$

$US_{m,y}^{(x)}(t)$ for the y^{th} finger of the x^{th} desired user received at the m^{th} antenna element describes the ISI's coming from signals of the desired x^{th} user at different delays other than the one time-locked by the y^{th} finger. It is defined as

$$US_{m,y}^{(x)}(t) = \sum_{\substack{k=0 \\ k \neq y}}^{K-1} L_{m,k}^{(x)}[t - \tau_{k,y}^{(x)}(t)] \ell^{(x)}[t - \tau_{k,y}^{(x)}(t)] \exp\{j\psi_{m,k}^{(x)}[t - \tau_{k,y}^{(x)}(t)]\}. \quad (5.6)$$

$UM_{m,y}^{(x)}(t)$ for the y^{th} finger of the x^{th} desired user received at the m^{th} antenna element is the unwanted signals generated by all but the x^{th} user in the system including all the multipath components, and is expressed as

$$UM_{m,y}^{(x)}(t) = \sum_{\substack{n=0 \\ n \neq x}}^{N-1} \sum_{k=0}^{K-1} L_{m,k}^{(n)}[t - \tau_{k,y}^{(n)}(t)] \ell^{(n)}[t - \tau_{k,y}^{(n)}(t)] \exp\{j\psi_{m,k}^{(n)}[t - \tau_{k,y}^{(n)}(t)]\}. \quad (5.7)$$

To model the single path case, the general structure of the transmission channel model would be the same. However, in this case, there would be only one finger needed to capture the single path, making $K = 1$ and $Y = 1$, and the time delay $\tau_{k,y}^{(n)}(t)$ would disappear from Equations 5.6 and 5.7.

5.2.3 Uplink Receiver Model

The received baseband signals at the receiver will undergo the time alignment process as needed for the multipath case, the decoding process involving the descrambling and despreading operations, and the smart antenna adjustment process steering the antenna system towards certain directions. The receiver model for the uplink path is composed of an antenna array with M elements and Y Rake fingers in a 2D manner and is depicted in Figure 5.2.

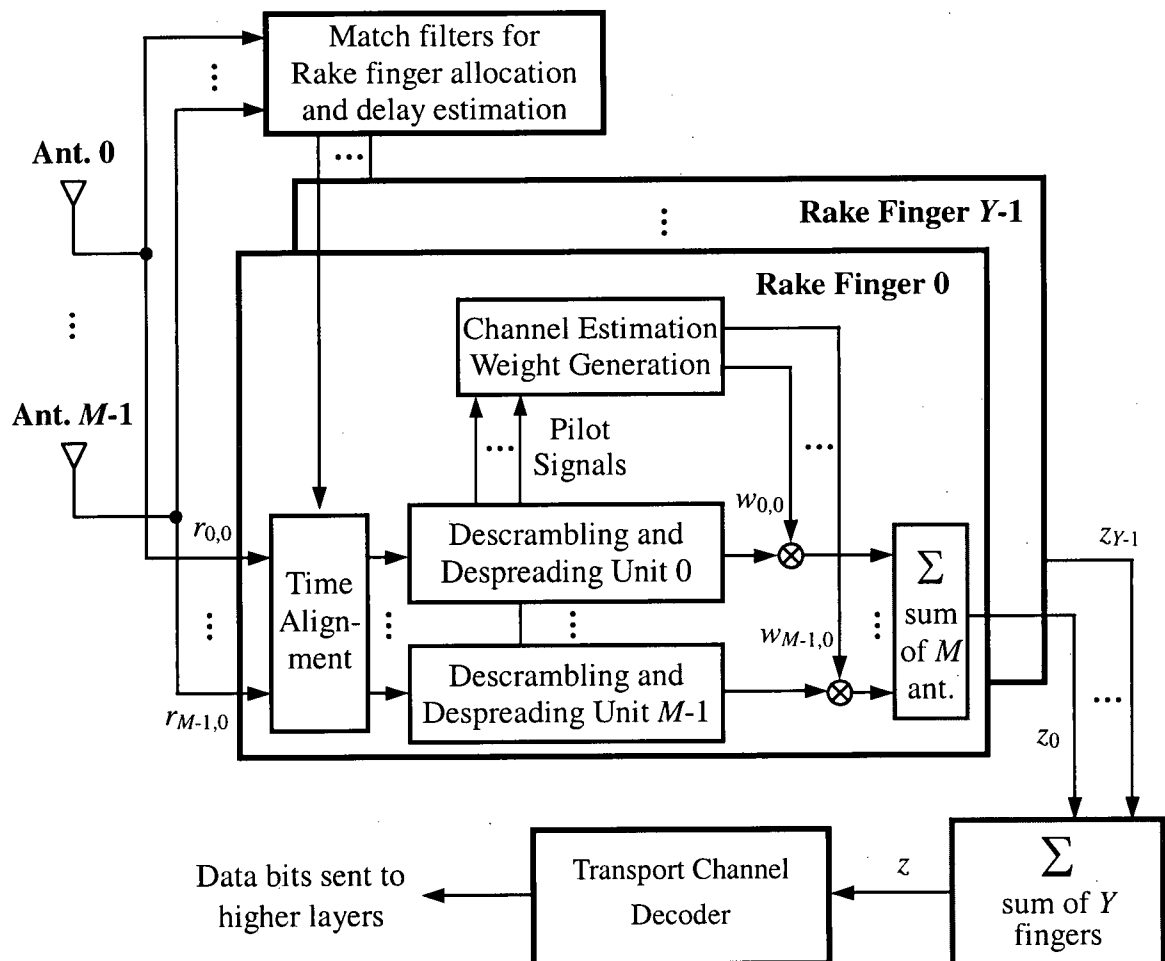


Figure 5.2 The 2D Receiver Model with Signal Processors

The received signals at the m^{th} antenna element include several multipath components as shown in Equation 5.3. As illustrated in Figure 5.2, the stream of operations of the antenna receivers begins with the delay estimation process according to the received signals. To recover and make use of the path diversity of multipath signals, the received signals are passed through matched filters to measure and determine the delays of the multipath components with the help of pilot signals. Based on these estimated delays, each Rake finger, as described in Section 4.3.3, is assigned to process the signals of one of the multipaths with specified delay information. With the delay information, the time alignment process of each finger aligns the multipath delayed signals so that the chips in a frame will be properly positioned before the decoding process. The received signals at the y^{th} finger of the m^{th} antenna element of the x^{th} desired user would have a delay $\tau_{k,y}^{(x)}$ and can be time aligned by

$$r_{m,y}^{(x)}(t) = r_{m,y}^{(x)}[t - \tau_{k,y}^{(x)}(t)]. \quad (5.8)$$

Through time alignment, the delay is compensated for the difference in the arrival times of the signals in each finger so that the starting and ending chip positions within a frame would match those of the decoding chips.

The next process is the decoding process. The decoding process is essentially the reverse of the encoding process as depicted in Figure 5.1 and will convert the received signals chips into data bits according to the encoding information. This stage includes three decoding sub-processes, namely the descrambling, despreading, and transport channel decoders. Since signals from all antenna elements can be multiplied by a scalar value without distorting the spatial characteristics of the received data vector, it is

possible to interchange the processing order between the descrambling and despreading sub-processes and the smart antenna adjustment process. The operation flow chosen for this thesis, as shown in Figure 5.2, assumes that the descrambling and despreading sub-processes at the chip rate are performed first before weight adjustments. The data symbol level processing, including the channel estimation, weight multiplication, combiner, and transport channel decoder, are dealt with afterwards. Figure 5.3 shows the flow of these sub-processes as well as the processed data formats for a single antenna element.

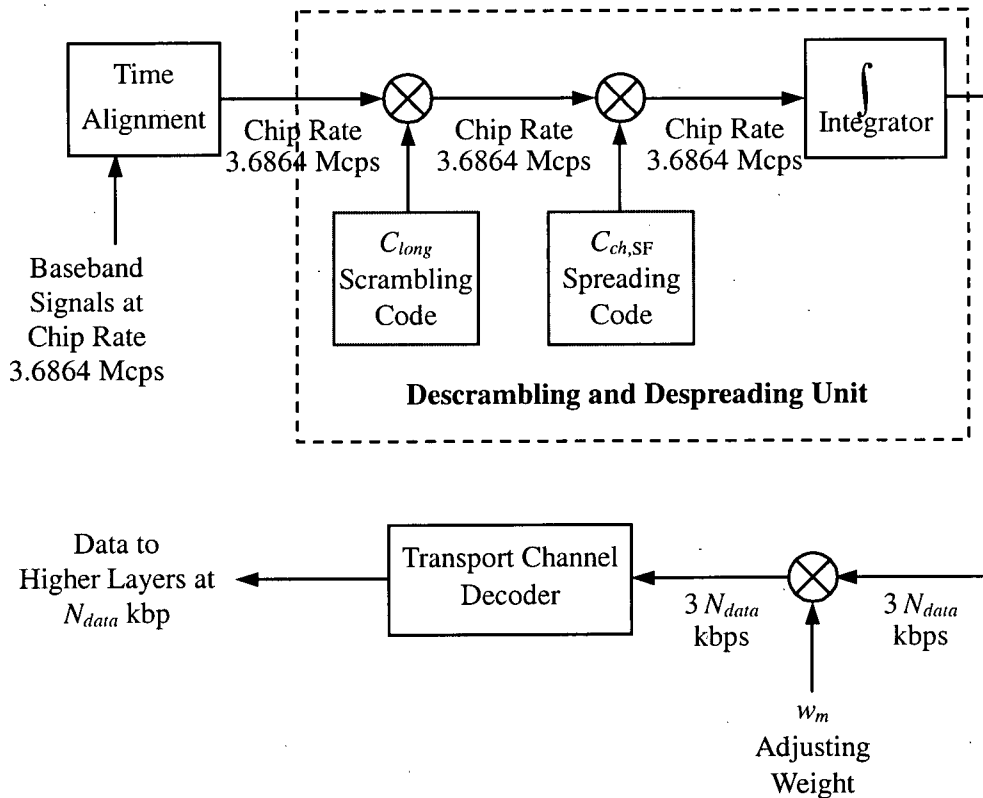


Figure 5.3 Data Formation Processes

As illustrated in Figure 5.3, after the time alignment sub-process, the time aligned

signals are descrambled with the same scrambling code that is used to encode signals in the transmitter model. Similarly, the subsequent despreading sub-process involves the same spreading code that has been used in the transmitter model. The integrator integrates the despread signals over every window with the size of the SF to complete the despreading sub-process.

Meanwhile, the descrambled and despread pilot signals are sent to the channel estimator sub-process to approximate the channel state. Depending on the smart antenna technology used for simulation, the MRC or IRC scheme as described in Section 4.4, the appropriate weight vectors will be generated accordingly. At the weight multiplier, the generated weights are multiplied with the integrated symbols. Before sending the symbols to the transport channel decoding process, each symbol will undergo the real to binary conversion. The Viterbi decoder or turbo decoder, as explained in Section 2.2, is used to decode the symbols that have been encoded by the respective transport channel encoder before sending the data bits to the higher layers.

For the single path case, the general receiver model would be the same as for the multipath case. However, in this case, there is no time alignment process required, and there would only be one finger in the receiver, making $Y = 1$ in Figure 5.2.

5.3 System Methodology

With the overall transmission path described in Section 5.2, this section will explain the design of the computer simulation process. Each run of the simulation is composed of two stages. The first stage is the pre-run set up where the system and user parameters will be estimated. The second stage is the capacity estimation stage. Power control for

estimating the necessary transmitting power for each user will be approximated at the first stage and adjusted at the second.

5.3.1 Pre-run Setup Stage

To run the simulation efficiently, it is necessary to generate the system and user profiles before the actual run for determining the capacity. The system under consideration is assumed to be a multi-cell system servicing a 19-cell region with one BS being responsible for each cell as shown in Figure 5.4. This 19-cell model consists of 3 tiers, with cell 0 as the first tier, cells 1 to 6 as the second tier and cells 7 to 18 as its third tier [18][19]. Each hexagon has a radius of 4 kilometers for macro-cell environments.

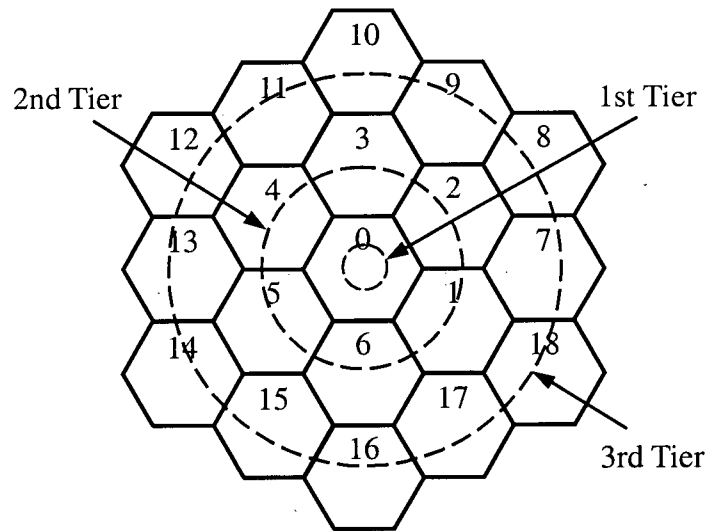


Figure 5.4 Structure of the 3-tier, 19-cell System

For these 19 cells, it is also assumed that each cell has a BS located at its center. Thus, the profiles of the 19 BS's, including the scrambling code of the BS and the number of MS's located in the cell, will be generated accordingly. The next step would

be to set up the profiles of the MS's located in each BS. The physical location of each MS is generated using a uniform distribution in the 19-cell system. The location information will determine the distance between a BS and a MS and hence the transmission path loss between the two. The location of a MS alone, however, does not decide the BS to which a MS subscribe. BS subscription is based on the strongest pilot signal, meaning that a MS will subscribe to one of the surrounding BS's with the smallest propagation loss [19]. After BS subscription, the AOA's of signals arriving at the antennas are generated according to the GBCM model in Section 3.3.1. If the simulation is for a multipath environment, each MS will be assigned with a multipath power profile created by the Hashemi model. Lastly, the scrambling and OVSF codes that are used for the coding process must be assigned to the MS's.

The WCDMA system allows mixed voice and multimedia traffics to be transmitted at the same time as mentioned in Section 2.3.2. For simplicity, it is assumed that there are only two types of traffics in the WCDMA simulator, and each user will belong to either the voice traffic or the multimedia traffic group, but not the mix of the two. The voice traffic will be transmitting at the rate of 19.2 kbps with a SF of 128 and the multimedia traffic will be transmitting at 76.8 kbps with a SF of 32.

5.3.2 Power Control

Power control implemented in the WCDMA simulator focuses on two areas. One area, known as the open loop power control, is used to compensate the path loss due to propagation and is calculated at the pre-run stage at the time of computing the propagation loss. The other area, known as the closed loop power control, is to monitor

the BER performance at run time to ensure the quality of the service.

Due to the *near-far* effect [20], it is necessary to impose tight power control over how much power will be transmitted for each user. As defined by Equations 3.2, 3.5, and 3.6, the path loss for each user is calculated according to the carrier frequency, the heights of the transmitting and receiving antennas, the distance between the transmitting and receiving antennas, and the correction factor for city sizes. It is assumed that the pilot signals will yield enough information for estimating the power loss due to propagation, and hence the open loop power control will compensate for that loss [14].

In the open loop power control scheme, the transmitted power at the beginning of a connection is determined based on the propagation path loss. An energy-to-interference threshold E_b/I_o will also be assigned to each user as the minimal required power to maintain the required BER performance, where I_o is the interference power density. This means the transmitted power for each user will be proportional to E_b/I_o , and the desired received power at the receiver will be at least the threshold value. Thus, for each capacity simulation, the transmitted power of a user is calculated from the desired received power and the path loss to allow the E_b/I_o requirement to be met. It is given by

$$P_t = (E_b/I_o)_{\text{required}} + L_{\text{path}} \quad (5.9)$$

where $(E_b/I_o)_{\text{required}}$ is the required E_b/I_o threshold and L_{path} is the path loss. The received power will then be at the E_b/I_o threshold level after experiencing propagation path loss. This open loop power control in Equation 5.9 is only used to set the initial and coarse transmitting power for each user at the pre-run stage. For uplink simulations,

$(E_b / I_o)_{required}$ is set to 7.0 dB as has been considered in [19].

Additionally, due to the difference in PG between the voice and multimedia users, the initial transmitting powers for the two groups will be set differently. The voice user group, using a larger SF denoted as SF_v that has a PG of 128, is used as the reference group and no extra transmitting power will be assigned for this group. Its transmitting power will be calculated using Equation 5.9. The multimedia user group has a smaller SF denoted as SF_m and a lower PG of 32, and thus will be assigned with extra transmitting power to compensate for the lower PG. To calculate the amount of extra power required, it is necessary to determine the difference in PG between the two groups in dB by

$$\Delta Gain = 10 \log_{10} \left(\frac{SF_v}{SF_m} \right). \quad (5.10)$$

Thus, the transmitting power for the multimedia group will be defined by

$$P_{t-m} = (E_b / I_o)_{required} + L_{path} + \Delta Gain, \quad (5.11)$$

Another important feature in power control that distinguishes the voice traffic group from the multimedia traffic group is a control mechanism called voice suppression. Studies have shown that human voice traffic is only active 35% to 40% of the time, meaning that there is no need to transmit during the inactive periods [19]. To take advantage of this fact, the voice activity is continuously monitored by digital vocoders, and transmission is suppressed for the channel whenever this is no voice activity present. In the WCDMA simulator, the voice activity percentage is set to a conservative value of

50%. For each transmitted slot from each voice traffic user, a binomial random variable will be assigned with a probability of $\delta = 0.5$. If the binomial variable for a voice traffic user is assigned with a "0", it means that this slot from this user will not contribute any interference to other users during the silent period, and this slot will be dropped from the interference calculation in Equation 5.7. On the other hand, a "1" would indicate the presence of voice activity and this particular slot will cause interference to others. For multimedia traffic users, however, it is assumed that high-rate circuit-switched service such as real-time video transmission is being employed, and the traffic activity is set to be active 100% of the time [43]. Therefore the multimedia users will always be included for interference calculations.

Furthermore, in the WCDMA system, transmissions are subject to various types of interferences including the inter-cell interference, intra-cell interference, and ISI due to the fact that all users in the system share the same bandwidth. As a result, power control must be also considered at run time to monitor the quality of transmission in order to yield the best overall performance. Since the calculation of the transmitted power in Equation 5.9 does not take into account the interference described by Equations 5.6 and 5.7, additional power control at run time is required for monitoring the interference that each MS is subject to. Each MS would be considered having its link to the BS broken if the received data has a BER greater than 0.1% [18]. Therefore the additional closed loop power control at runtime will be based on this cutoff limit.

The closed loop power control is implemented as follows. After the completion of transmitting a slot, the BER of each transmitted slot is computed for each user. If the BER is below the required 0.1%, the transmitted power would be increased by an

increment step of 2.0 dB. Each transmitted radio frame of length 10ms, as will be discussed in Section 6.1, is divided into 12 slots. Thus implementation of the close loop control will be executed at 100×12 times per second, or 1.2kHz. At this rate, the close loop power control would operate faster than any significant PL or even faster than the speed of Rayleigh fading at low or moderate mobile speeds [44].

5.3.3 Capacity Simulation Run

After the pre-run setup for the necessary parameters, simulation runs are ready to begin. Each simulation run is designed to determine the maximum number of users that the system could accommodate before saturation. To begin with, the system would have a certain number of user profiles set up as described in Sections 5.2.1 and 5.2.2 as the potential system users that will be active in a run. This pre-generated user number, denoted as the total profile number, should be much greater than the expected system capacity so that the system wouldn't be reaching its limit before the actual saturation level.

Each simulation run will determine the system capacity using the divide and conquer technique. When each simulation run begins, the system will load a certain number of users randomly selected from the pre-generated user profiles into the system for the first loop. This number is defined as the initial system user number. Chip level simulations will be performed for several slots using the transmitter model, the transmission channel model, and the receiver model described in Section 5.1. After the chip level simulations for each user, the BER results will be calculated for each user, and those whose BER is below the required 0.1% will be considered as broken links.

By counting the number of users having their links broken, the broken link percentage over the total active users loaded in the system can be established. If the broken link percentage is above the target level, which will be defined in Section 6.1, then the number of users loaded in the system will be reduced to half of the current number for the second loop. On the other hand, if the broken link percentage is below the target level, the system will load more users into the system for the second loop by a step size. Each simulated run will end when the broken link percentage is approximated to the target level within a small range. The determined system capacity will then be the current number of active users loaded in the system for simulation. By using this divide and conquer technique described above, the system capacity can be established fairly accurately.

The flow diagram in Figure 5.5 shows the sequence of the steps taken as mentioned in the previous paragraph to determine the system capacity. The start and end points are indicated with rectangular ellipses, processes with rectangles, decision points with rhombuses, and directions of flow with arrows.

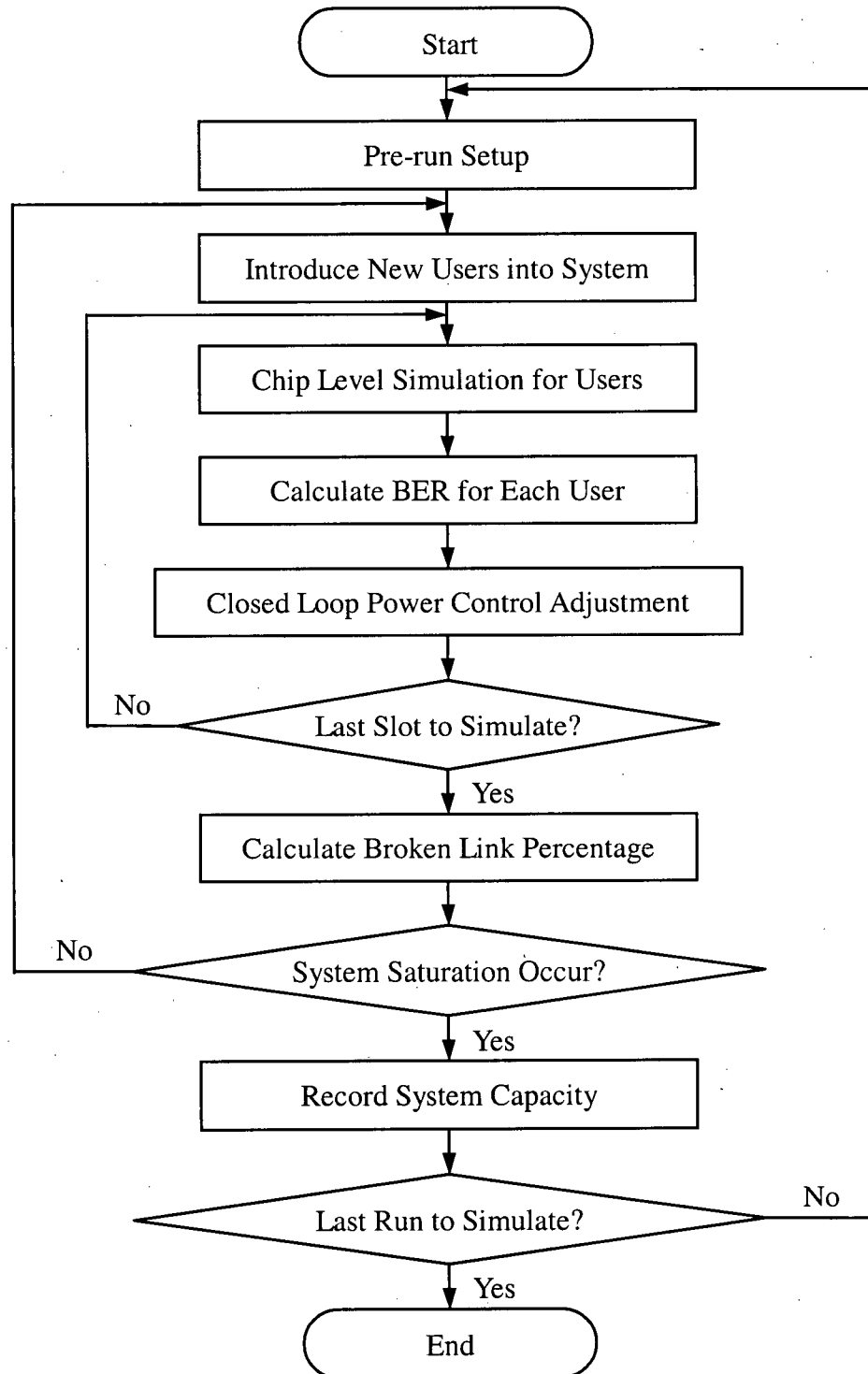


Figure 5.5 Capacity Simulation Flow Diagram

5.4 Conclusions

In this chapter, the WCDMA system simulator has been introduced. Section 5.2 describes the overall WCDMA uplink model that integrates the transmitter, transmission channel, and receiver sub-models from the previous chapters. The pre-transmission operations required to prepare data before transmission have been defined in the transmitter model. Transmission channel model characterizes the multipath and single path scenarios and classifies the desired and undesired signals in the total received signals. In Section 5.3, the system methodology is explained. At the pre-run stage, the profiles and parameters of each BS and MS are made ready for simulation. The power control that occurs at pre-run stage is the open loop power control while the closed loop power control takes place during simulation. The sequence of operations for the capacity simulations runs has also been presented.

CHAPTER 6 UPLINK WCDMA CAPACITY SIMULATION

RESULTS AND DISCUSSIONS

6.1 Introduction

In this chapter, the capacity performance results of the WCDMA system based on simulation runs using the system methodology in Chapter 5 will be presented. The simulation results include both the single path case and the multipath case. Direct line of sight is assumed for the single path case. The multipath simulations are based on the Hashemi model to simulate the multipath environments of three different geographical areas. The capacity study also considers how different numbers of antenna elements in the antenna array would affect the capacity, as well as how the smart antenna technologies would have an impact on the number of users that the system could serve. Additionally, the difference in the performances between the two transport channel codes is investigated. Specifically, the simulation results are compared for convolutional codes and turbo codes. Furthermore, the mixed traffic service provided by the WCDMA system is a point of interest. Capacity results have been simulated for mixed of voice and multimedia traffics.

This chapter is organized as follows. Section 6.2 describes the computer simulation methodologies and the simulation parameters for the WCDMA simulator implemented for this thesis. The results from the single path simulations with different system configurations are presented in Section 6.3. Section 6.4 provides the simulation results for the multipath case. Section 6.5 compares the results with the outcomes in other publications and Section 6.6 gives the conclusion of this chapter.

6.2 Computer Simulation Methodologies and Simulation Parameters

The WCDMA simulator is completely designed in software. It is written in the C++ language with the aid of the Microsoft Visual C++ to run on PC. The pseudo-random variables used in the simulation runs are generated using a modified version of the random number generator in the Numerical Recipes Software. It is designed to generate pseudo-random variables in uniform distribution.

In order to display the simulation results, the mean and standard deviation of the capacity results will be computed and tabulated. Also, the CDF's of the capacity results will be calculated and plotted for graphical presentation. CDF is defined by

$$CDF(x) = \frac{N_{result}(x)}{N_{Total}} \quad (6.1)$$

where $N_{result}(x)$ is the number of capacity results less than or equal to the capacity value x , and N_{Total} is the total number of runs for each system design. To produce a large set of random system loading conditions, $N_{Total} = 1000$ is chosen. With the sufficient number of runs, accurate results of the overall system capacity are obtained for this study.

Capacity simulations are based on the WCDMA system parameters shown in Table 6.1. In Table 6.1, the hexagonal cell radius is chosen to be 4 km as in [18][19]. The effects that varying the cell radii has on system performance have been studied elsewhere [45]. The spread factors for the voice traffic SF_v and multimedia traffic SF_m are set to 128 and 32 [46], for transmission rates of 19.2 and 76.8 kbps respectively. The broken percentages allowed before reaching system saturation are 5% and 10% for the voice and multimedia traffics correspondingly as set in [46][47]. The rationales in determining the rest of the parameters listed in Table 6.1 have been explained in the previous chapters.

SYSTEM PARAMETERS	PARAMETER VALUES
Transmitted Chip Rate	3.6864 Mcps
Radio Frame Time	10 ms
Slots per Frame	12
Number of Cells in the System	19
Hexagonal Cell Radius	4 km
Target BER	0.001
Required E_b / I_o	7 dB
Closed Loop Power Control Step Size	2 dB
Channel Coding Rate	1/3 for Convolutional Coding 1/3 for Turbo Coding
SF	128 for Voice Traffic 32 for Multimedia Traffic
Transmission Activity	50% for Voice Traffic 100% for Multimedia Traffic
Broken Link Percentage for System Saturation	5% for Voice Traffic 10% for Multimedia Traffic
Pilot Signal Length of a Slot	20%
Antenna Pattern	Omnidirectional

Table 6.1 System Parameter Values Assumed in Capacity Simulations

6.3 Single Path Results

In this section, the simulation results of the single path case are presented for different channel encoding methods, traffic mixes, and numbers of antenna elements. Figure 6.1 shows the CDF's of various traffic mix percentages for the uplink single path transmission simulation with the convolutional coding algorithm, a two-sensor

omnidirectional antenna array at the BS's, and the MRC smart antenna configuration.

In Figure 6.1, five types of traffic mix percentages are depicted where “100% voice” corresponds to the case where the system has voice traffic users only, “75% voice” represents 75% voice and 25% multimedia traffic users, “50% voice” means half voice and half multimedia traffic users, “25% voice” implies 25% voice and 75% multimedia traffic users, and “0% voice” indicates that the system has multimedia traffic users only. The title of these five particular traffic mix groups will be denoted in italicized letters for the purpose of presentation hereafter. The capacity in the graph is the saturation level for the whole 19-cell system. Table 6.2 shows the statistics of the results presented in Figure 6.1 and the average capacity per cell from dividing the system capacity by 19.

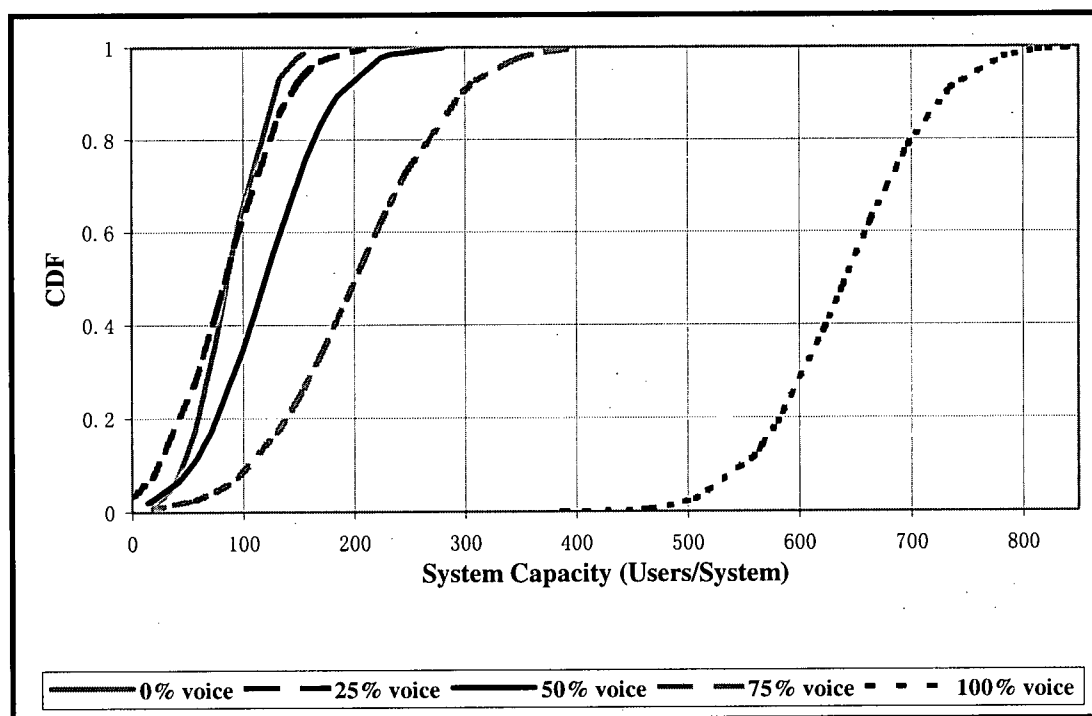


Figure 6.1 Uplink Capacity Results of a Single Path System with the Convolutional Encoder, and a 2-element MRC Omnidirectional Antenna Array

Traffic Mix %	System Capacity (Users)	Standard Deviation	Cell Capacity (User / Cell)
<i>100% Voice</i>	642	79	34
<i>75% Voice</i>	201	74	11
<i>50% Voice</i>	120	52	6
<i>25% Voice</i>	84	46	4
<i>0% Voice</i>	86	31	5

Table 6.2 Simulation Results in Figure 6.1 and the Average Cell Capacity

The results indicate that the average cell capacity for the *100% voice* traffic mix is 34 users per cell, and for the *75%*, *50%*, *25%*, and *0% voice* traffic mixes the average users per cell are 11, 6, 4, and 5 respectively. The fact that the cell capacity at *25% voice* traffic mix of 4 users per cell is lower than that at *0% voice* traffic mix of 5 users per cell reflects the difference in the broken link percentages allowed for the voice traffic and the multimedia traffic. In addition, the increase of the number of multimedia traffic users in the system makes the total capacity decrease dramatically as expected. With all voice traffic users in the system, the capacity is 34 users per cell comparing to 6 users per cell when half of the users are of voice traffic, and 5 users per cell for all multimedia traffic users. The relations between voice traffic users and multimedia traffic users will be examined later in this section.

Figure 6.2 illustrates the results of the same system configuration as the one in Figure 6.1, except that in this case, the channel encoding algorithm uses turbo codes instead of convolutional codes. Table 6.3 tabulates the statistics of the results in Figure 6.2 and the average cell capacity.

The results indicate that for the turbo coding, two-element MRC antenna system, saturation occurs at 37, 14, 9, 6 and 6 users per cell for 100%, 75%, 50%, 25%, and 0% voice traffic mix scenarios. By comparing the performances of the convolutional encoding and the turbo encoding from the results in Tables 6.2 and 6.3, the improvement of the turbo code over the convolutional code is tabulated in Table 6.4.

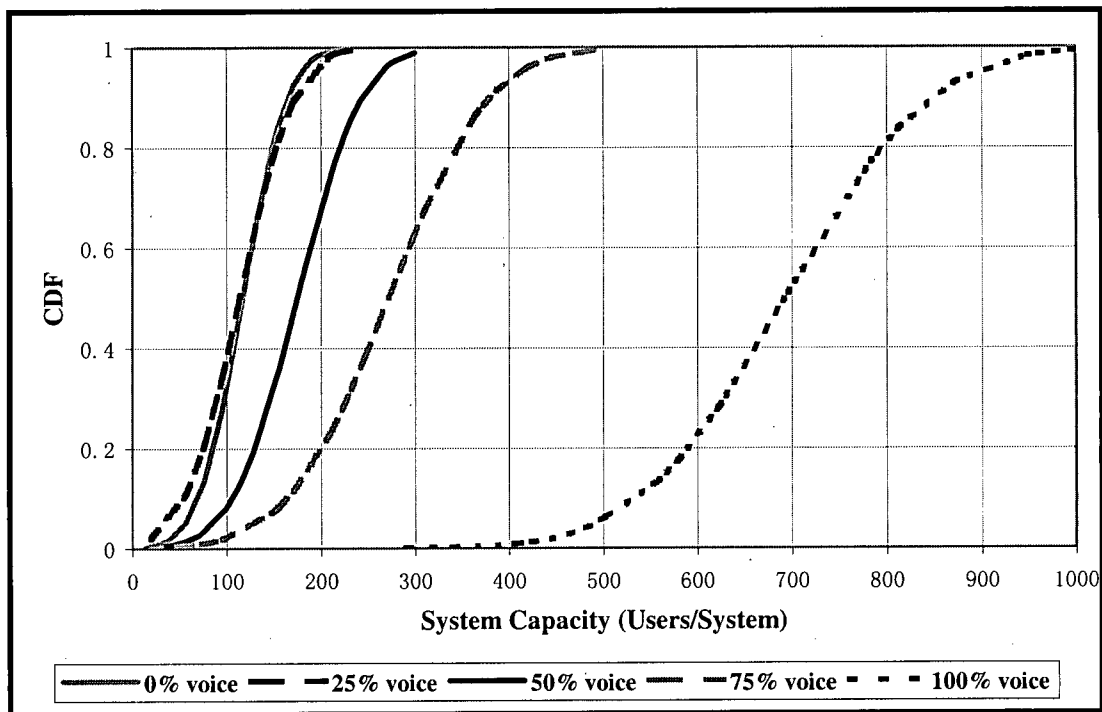


Figure 6.2 Uplink Capacity Results of a Single Path System with the Turbo Encoder, and a 2-element MRC Omnidirectional Antenna Array

From the comparisons in Table 6.4, when all the users in the system are voice users, the turbo codes have the smallest gain over the convolutional codes at 8%. For all the other traffic mix groups including the one with all multimedia users, the gains become substantial, ranging from 35% to 46%. The reason behind this would be the PN interleaver in the turbo code encoder described in Section 2.2.3.1. Consider a voice

traffic user and a multimedia traffic user both transmitting a single slot. The raw bit length for the multimedia traffic user would be four times greater than that of the voice traffic user. Since the PN interleaver of the turbo code performs as well as any other interleaver when the block size to be encoded is large, the multimedia traffic user would have a better performance over the voice traffic user when using turbo codes, as suggested in the comparisons in Table 6.4.

Traffic Mix %	System Capacity (Users)	Standard Deviation	Cell Capacity (User / Cell)
<i>100% Voice</i>	693	121	37
<i>75% Voice</i>	272	84	14
<i>50% Voice</i>	175	54	9
<i>25% Voice</i>	114	46	6
<i>0% Voice</i>	117	37	6

Table 6.3 Simulation Results in Figure 6.2 and the Average Cell Capacity

Traffic Mix %	Turbo Code Gain over Convolutional Code
<i>100% Voice</i>	8%
<i>75% Voice</i>	35%
<i>50% Voice</i>	46%
<i>25% Voice</i>	36%
<i>0% Voice</i>	38%

Table 6.4 Turbo Code Improvement over Convolutional Code
with Varied Traffic Mixes

Figure 6.3 illustrates the results of the same system configuration as described for the one in Figure 6.2, except that in this case, the antenna array has four antenna elements instead of two. Table 6.5 tabulates the statistics of the results in Figure 6.3 and the average cell capacity.

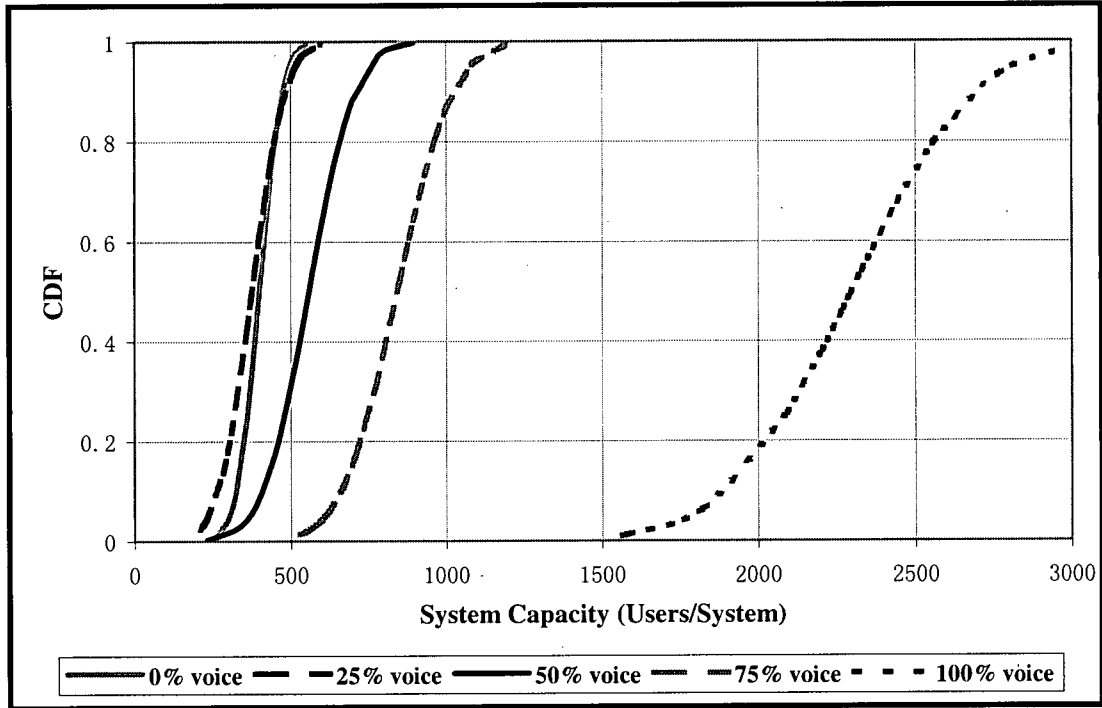


Figure 6.3 Uplink Capacity Results of a Single Path System with the Turbo Encoder, and a 4-element MRC Omnidirectional Antenna Array

The results indicate that for the turbo coding, four-element MRC antenna system, saturation occurs at 122, 44, 29, 20 and 21 users per cell for 100%, 75%, 50%, 25%, and 0% voice traffic mix scenarios. By comparing the turbo coding MRC smart antenna system performances between a four-element array and a two-element array, Table 6.6 is made.

Traffic Mix %	System Capacity (Users)	Standard Deviation	Cell Capacity (User / Cell)
<i>100% Voice</i>	2311	340	122
<i>75% Voice</i>	843	141	44
<i>50% Voice</i>	559	117	29
<i>25% Voice</i>	376	85	20
<i>0% Voice</i>	400	59	21

Table 6.5 Simulation Results in Figure 6.3 and the Average Cell Capacity

Traffic Mix %	4-element Array Gain over 2-element Array
<i>100% Voice</i>	233%
<i>75% Voice</i>	210%
<i>50% Voice</i>	220%
<i>25% Voice</i>	230%
<i>0% Voice</i>	240%

Table 6.6 4-element Array Improvement over 2-element Array
with Varied Traffic Mixes

One would think that when the number of antenna elements is doubled, the net capacity of the system is possible to double as well. However, in this simulation, the improvement of the four-element array ranges from 210% to 240% over the two-element array, which is better than expected. The additional gain comes from the soft decoding capability of the turbo code decoder.

Figure 6.4 illustrates the CDF of the turbo coding, six antenna element, MRC smart antenna system with only the multimedia traffic users, and the CDF's for a two-element array and a four-element array are repeated here for comparison. The gains of the six-element and four-element arrays over the two-element array are summarized in Table 6.7. The result for the six-element array, multimedia users only system is 37 users per cell, which represents a 492% gain over the two-element array system. This performance gain, as expected, is consistent with the conclusions drawn from Table 6.6. Therefore, according to the simulation results for the antenna array consisting of two, four, and six elements, the capacity values can be closely approximated as a linear function of the number of elements in the antenna array.

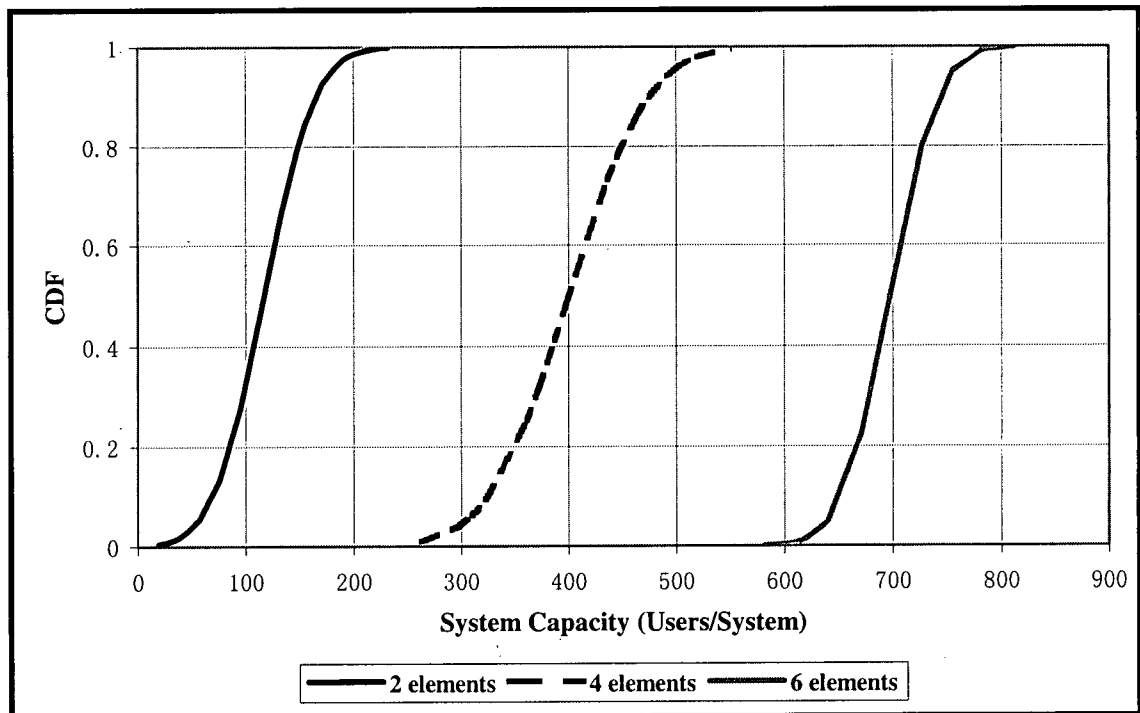


Figure 6.4 Capacity Results for an All Multimedia Traffic User Single Path System with a 2, 4, and 6 - element MRC Smart Antenna Array, and the Turbo Encoding Algorithm

Number of Antenna Elements	System Capacity (Users)	Cell Capacity (Users/Cell)	Gain over 2-element Array
2	117	6	Reference
4	400	21	240%
6	697	37	492%

Table 6.7 Simulation Results in Figure 6.4 and the Average Cell Capacity

To highlight the effects that multimedia traffic users have on the overall capacity as mentioned earlier, a graph depicting the number of voice users versus the number of multimedia users that the system could accommodate is plotted. Figure 6.5 presents this graph using the average cell capacities for different traffic mixes taken from Table 6.2 and 6.3 for comparisons.

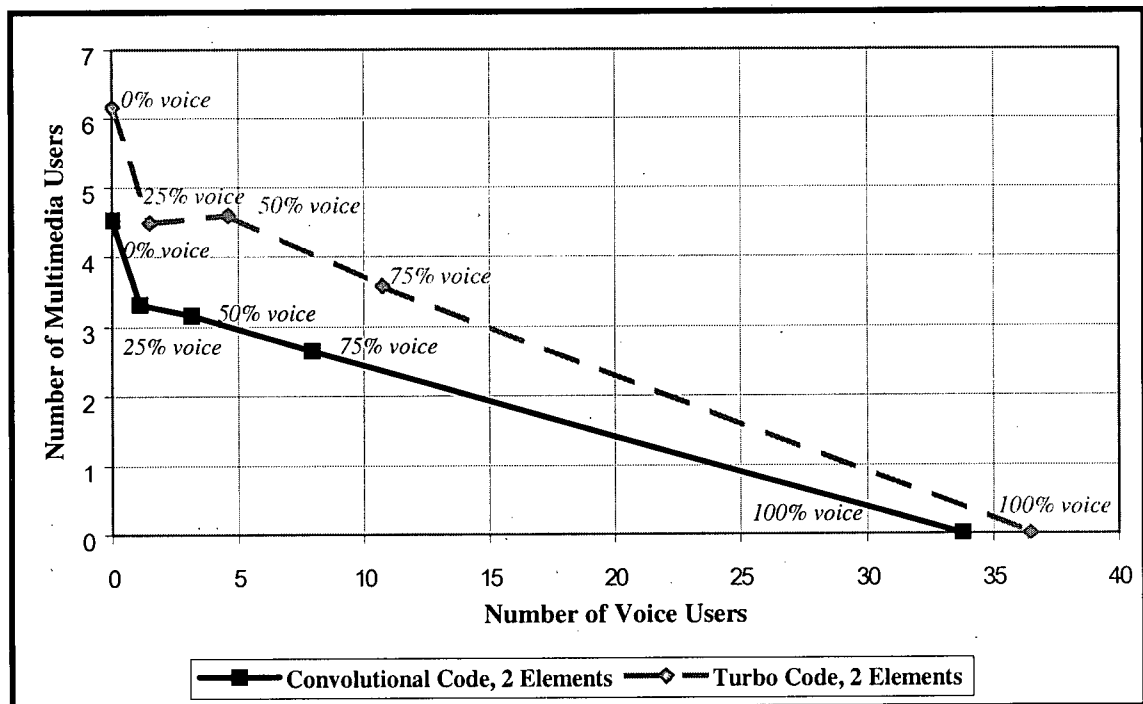


Figure 6.5 Simulation Results from Tables 6.2 and 6.3 with Different Percentages of Traffic Mix, Presented as Multimedia Users VS Voice Users Per Cell

As seen in Figure 6.5, for the convolutional code case, at the 75% *voice* traffic mix, the total number of served users decreases to about 31% with respect to the case with 100% *voice* traffic users, and at 50% *voice* traffic users it would decrease to 23%. When there are 75% and 50% *voice* traffic users in the system, the total number of users served by its turbo code counterpart would decrease to 39% and 25% of the total number of users served for the 100% *voice* traffic case. This is due to the fact that high speed data service could cause significant interference to the low rate voice service as discussed in [48]. As pointed out in Section 5.3.2, multimedia traffic users will be transmitting at a much higher power than voice traffic users in order to compensate for the low PG from the spreading code. Therefore, the high multimedia traffic factor decreases the capacity severely as the simulation results have shown here.

6.4 Multipath Results

In urban areas, single path transmissions are rather rare. Within a city, multipath propagation is almost always the case due to multiple reflections of signals. Thus multipath simulations are necessary to model city environments. Furthermore, different city sizes have different multipath characteristics. In simulating the multipath environments, the Hashemi multipath model in Section 3.5.1 will be used to emulate the multipath power profiles for downtown San Francisco as the downtown centre of a large size urban city, downtown Oakland as the downtown centre of a medium size city, and residential Berkeley as a rural city. According to the type of the geographical area to be simulated, each user in the system is randomly assigned with one of the forty thousand pre-generated power profiles from the Hashemi model, which carry multipath information for that particular area. The power profiles describe how the transmitting

power will be distributed into various multipath components.

The multipath power profiles generated for the residential Berkeley area have almost all of the transmitted power allocated in the first three of the five multipath components. Therefore, for this case, only three Rake fingers are used to capture the first three multipath components even though all five multipath components are simulated in the uplink transmission model. The performance results of a turbo encoding, two-element and four-element MRC antenna array system for the residential Berkeley area are illustrated in Figure 6.6 and summarized in Table 6.8.

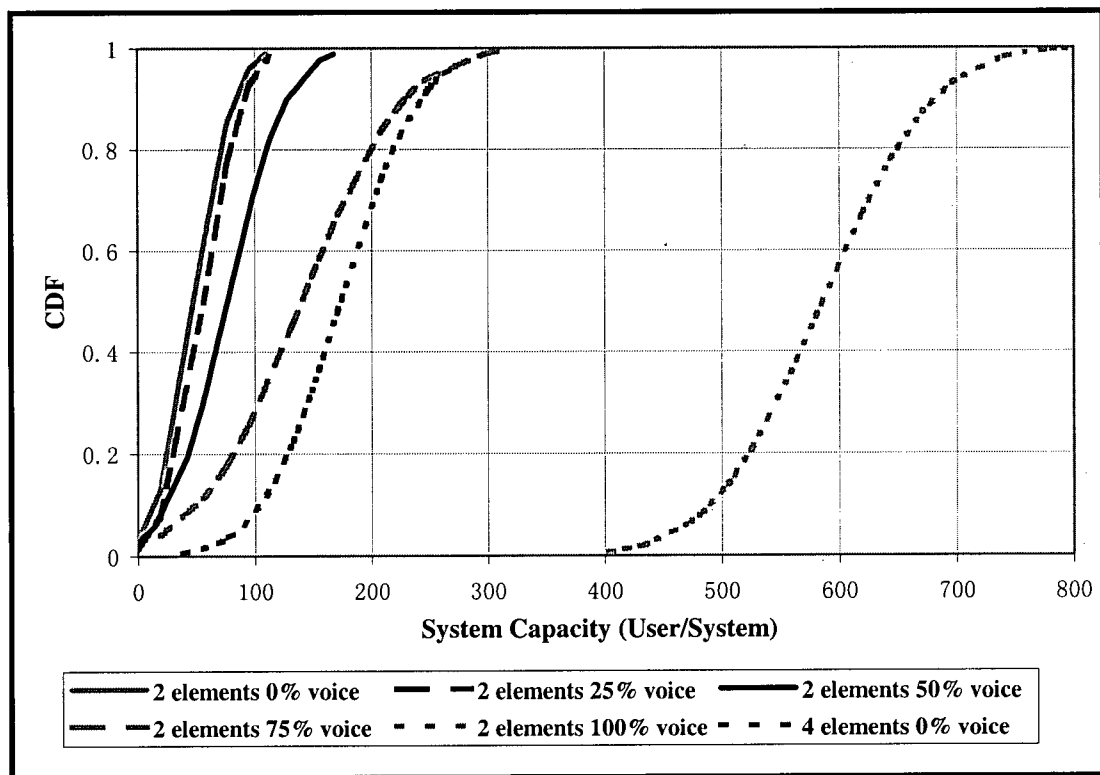


Figure 6.6 Uplink Capacity Results of a Multipath Residential Berkeley System with the Turbo Encoder and 3-finger MRC Smart Antenna

Number of Elements	Traffic Mix %	System Capacity (Users)	Standard Deviation	Cell Capacity (User/Cell)
2	100% voice	586	74	31
	75% voice	140	65	7
	50% voice	77	40	4
	25% voice	57	26	3
	0% voice	49	26	3
4	0% voice	169	50	9

Table 6.8 Simulation Results in Figure 6.6 and the Average Cell Capacity

For the two-element MRC antenna, saturation occurs at 31, 7, 4, 3 and 3 users per cell for 100%, 75%, 50%, 25% and 0% voice traffic mix scenarios, and the saturation level for the four-element MRC antenna system with only 0% voice traffic users is 9 users per cell. The gain from the four-element over the two-element antenna is around 242%. This gain is consistent with the findings in the single path case when the number of antenna elements are doubled or tripled as analyzed in Tables 6.6 and 6.7.

For the downtown Oakland area, the power profiles have power allocated in most of the first four of the five multipath components. Although five multipath components are simulated for the transmission model, only four Rake fingers are used to capture the first four multipath components. The performance results of a turbo encoding, two-element MRC antenna array system for the downtown Oakland area are illustrated in Figure 6.7 and summarized in Table 6.9. For this system configuration, saturation occurs at 32, 8, 4, 3 and 3 users per cell for 100%, 75%, 50%, 25% and 0% voice traffic mix scenarios.

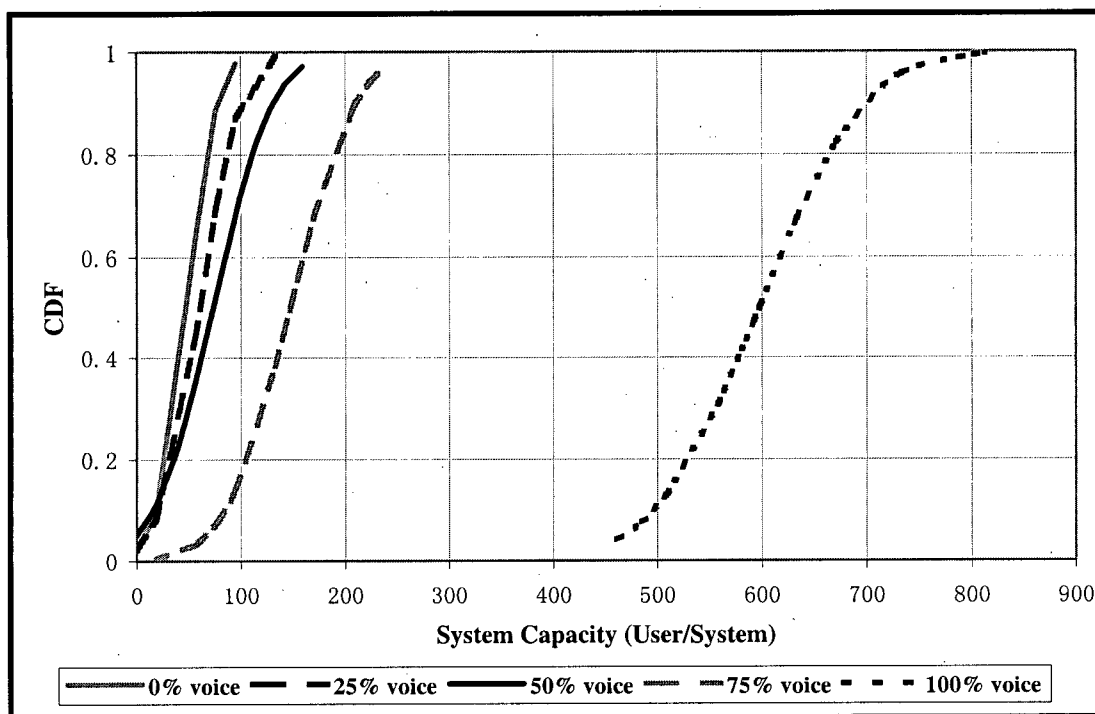


Figure 6.7 Uplink Capacity Results of a Multipath Downtown Oakland System with the Turbo encoder and 2-element 4-finger MRC Smart Antenna

Traffic Mix %	System Capacity (Users)	Standard Deviation	Cell Capacity (User/Cell)
<i>100% voice</i>	598	79	32
<i>75% voice</i>	147	49	8
<i>50% voice</i>	73	45	4
<i>25% voice</i>	61	30	3
<i>0% voice</i>	48	23	3

Table 6.9 Simulation Results in Figure 6.7 and the Average Cell Capacity

For the downtown San Francisco area, the power profiles have power allocated in all five multipath components. In order to compare the effects of capturing only a part of

the total multipath components versus capturing all of them, simulations have been performed for a system with only three Rake fingers that captures only three of the five multipath components, and also for a system with five Rake fingers that utilizes all five multipath components. For the case that captures only a part of the multipath components, the performance results of a turbo encoding, two-element, three-finger MRC antenna array system for the downtown San Francisco area are illustrated in Figure 6.8 and summarized in Table 6.10. For this system configuration, the results shows that saturation occurs at 31, 9, 6, 4 and 4 users per cell for 100%, 75%, 50%, 25% and 0% voice traffic mix scenarios

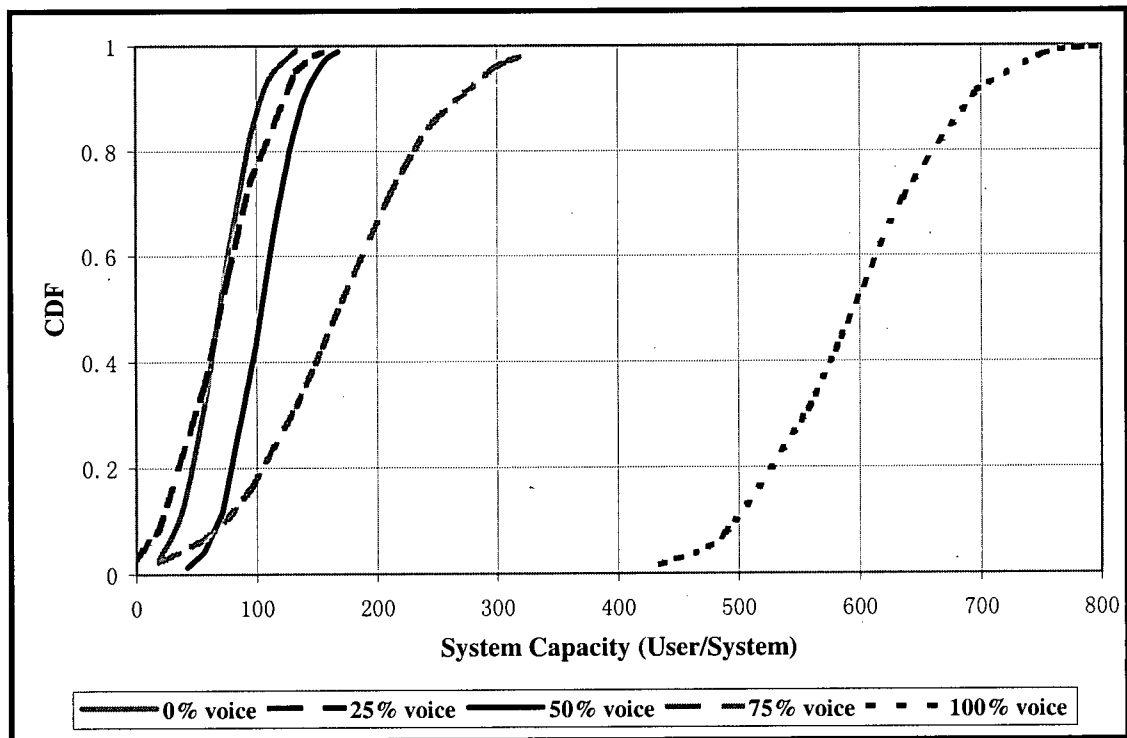


Figure 6.8 Uplink Capacity Results of a Multipath Downtown San Francisco System with the Turbo Encoder and 2-element 3-finger MRC Smart Antenna

Traffic Mix %	System Capacity (Users)	Standard Deviation	Cell Capacity (User/Cell)
<i>100% voice</i>	595	75	31
<i>75% voice</i>	169	64	9
<i>50% voice</i>	104	28	6
<i>25% voice</i>	71	38	4
<i>0% voice</i>	69	21	4

Table 6.10 Simulation Results in Figure 6.8 and the Average Cell Capacity

Figure 6.9 illustrates the simulation results for the same downtown San Francisco scenario but with five Rake fingers in the MRC antennas for the case that captures all five multipath components. Table 6.11 summarizes these results.

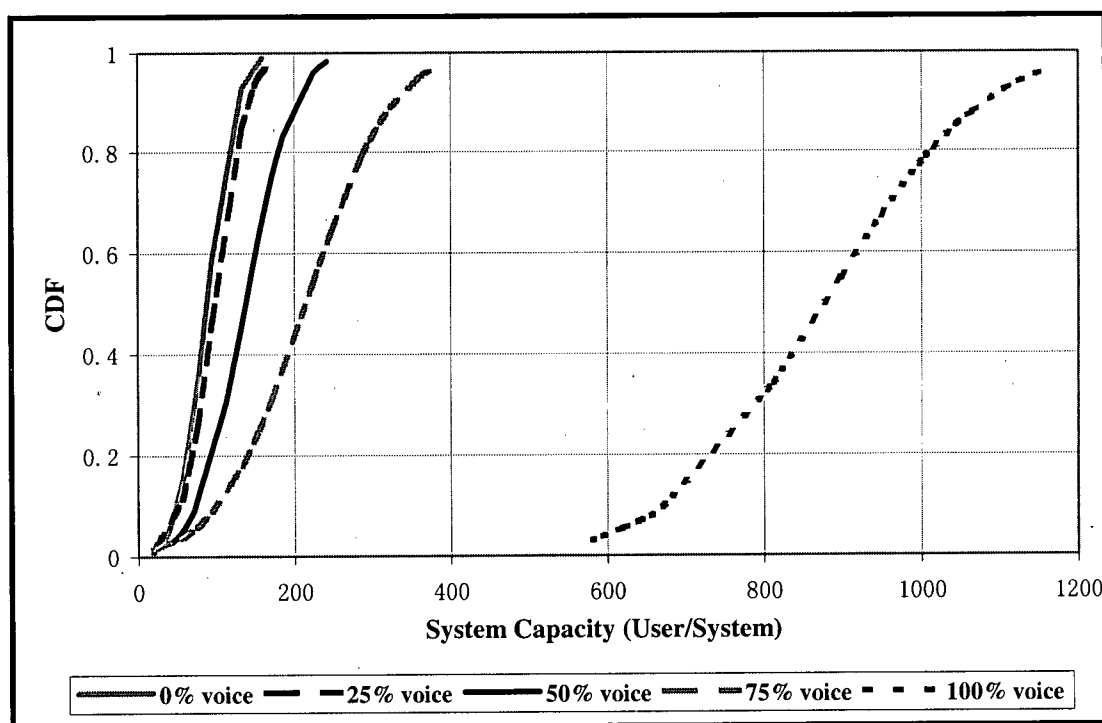


Figure 6.9 Uplink Capacity Results of a Multipath Downtown San Francisco System with the Turbo Encoder and 2-element 5-finger MRC Smart Antenna

Traffic Mix %	System Capacity (Users)	Standard Deviation	Cell Capacity (User/Cell)
<i>100% voice</i>	878	159	46
<i>75% voice</i>	214	89	11
<i>50% voice</i>	138	50	7
<i>25% voice</i>	98	34	5
<i>0% voice</i>	88	30	5

Table 6.11 Simulation Results in Figure 6.9 and the Average Cell Capacity

The results indicate that for the five Rake finger MRC antenna system, saturation occurs at 46, 11, 7, 5, and 5 users per cell for *100%*, *75%*, *50%*, *25%* and *0% voice* traffic mix scenarios. Based on the data from Tables 6.10 and 6.11, Table 6.12 compares the performance between the three Rake finger and five Rake finger configurations using the same MRC smart antenna.

Traffic Mix %	5-finger Gain over 3-finger	5-finger Gain over the Smallest Result in Table 6.8 or 6.9
<i>100% voice</i>	48%	50%
<i>75% voice</i>	27%	53%
<i>50% voice</i>	31%	85%
<i>25% voice</i>	38%	72%
<i>0% voice</i>	24%	84%

Table 6.12 5-finger Performance Gain over the 3-finger Case

From Table 6.12, the gain of the 5-finger case over the 3-finger case ranges from

24% to 48% for different traffic mix scenarios. With the power profile for the downtown San Francisco area distributing power into all five multipath components, more multipath interference will occur between users. However, based on the comparisons in Table 6.12, it is obvious that by setting up more Rake fingers with different multipath delays in the receivers, the extra multipath signals can be used as an advantage to the decoder. In this case, with five Rake fingers picking up the five multipath components, the decoder could more accurately decode data when compared with a three-finger receiver.

Furthermore, according to the data in Tables 6.8 and 6.9, the capacity results for residential Berkeley and downtown Oakland are similar, within less than two percentage of each other. This can be contributed to the similarity of the power profiles for these two areas. In their power profiles, there exists a strong multipath component carrying most of the signal power while the rest of the components contain feeble power. When examining Tables 6.11 and 6.12 for the results from the downtown San Francisco area using five Rake fingers, it is clear that downtown San Francisco has significant gains on the other two cities. The difference between the power profiles of this city and those of the other two is that the main signal power for downtown San Francisco is spread evenly into two or three multipath components whereas the signal power for the other two cities has only one dominant multipath component. Thus, when the outputs of the Rake fingers are summed together after individual processing, there is significant diversity combining gain from different Rake fingers for the downtown San Francisco case. As a result, the performance of the multipath simulation for the downtown San Francisco area is much better than the residential Berkeley and the downtown Oakland area.

The previous simulation results have all been based on MRC antennas. For comparison, the simulation results using the IRC antennas for the downtown San Francisco area are given here as well. Figure 6.10 illustrates the simulation results for the same downtown San Francisco scenario with five Rake fingers in the IRC antennas. Table 6.13 summarizes these results. The results indicate that for the five Rake finger IRC antenna system, saturation occurs at 53, 13, 8, 6, and 5 users per cell for 100%, 75%, 50%, 25% and 0% voice traffic mix scenarios. Compared to the results in Table 6.11, under the same settings except for the smart antenna technology utilized, the capacity results for the IRC antennas have noticeable gain over the MRC antennas. The detailed comparisons and discussions between the results for the MRC and IRC smart antennas will be commented in Section 6.5.

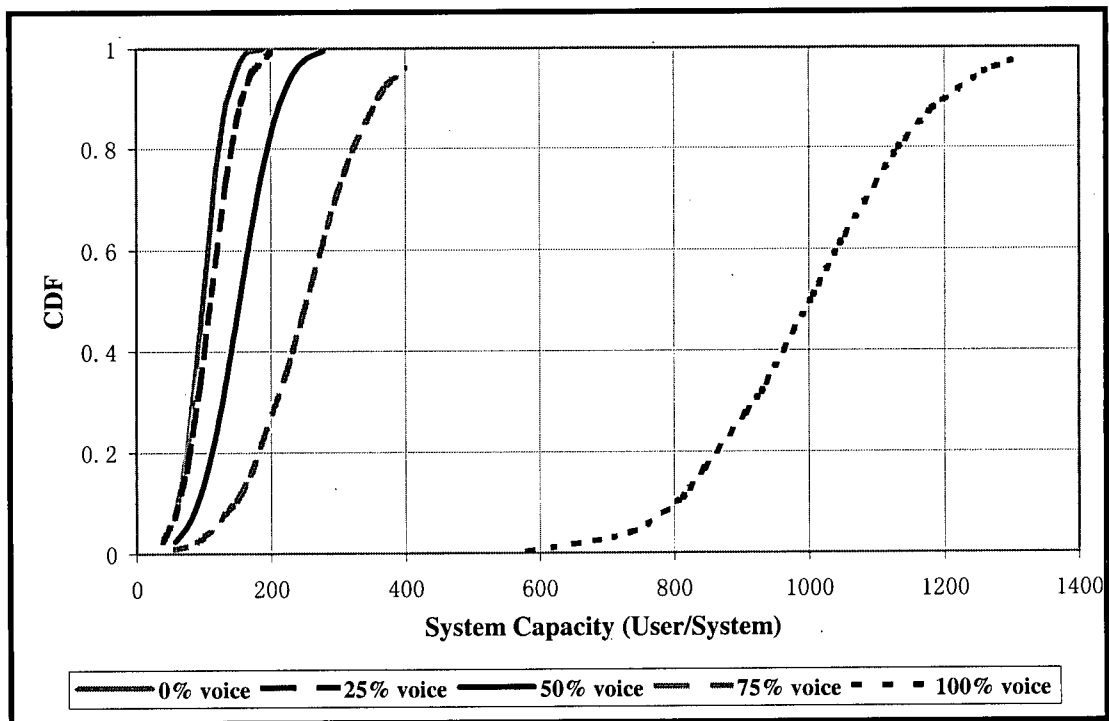


Figure 6.10 Uplink Capacity Results of a Multipath Downtown San Francisco System with the Turbo Encoder and 2-element 5-finger IRC Smart Antenna

Traffic Mix %	System Capacity (Users)	Standard Deviation	Cell Capacity (User/Cell)
<i>100% voice</i>	1003	154	53
<i>75% voice</i>	253	83	13
<i>50% voice</i>	153	49	8
<i>25% voice</i>	110	36	6
<i>0% voice</i>	99	28	5

Table 6.13 Simulation Results in Figure 6.10 and the Average Cell Capacity

Figure 6.11 plots the multimedia traffic users versus the voice traffic user graph using the data from Tables 6.8, 6.9, 6.11 and 6.13. From Figure 6.10, it is clear that the increase of the number of multimedia traffic users lowers the system capacity as mentioned in the single path case in Section 6.3. When compared to the single path case in Figure 6.5, the results for the residential Berkeley and downtown Oakland areas are not much different from the results for the single path case. This is because, as pointed out earlier, the power profiles for these two cities have one strong multipath component and several weak components. This pattern of their power profiles is very similar to that of the power profile for the single path case, which consists of only one full power component. Therefore, simulations for these two areas yield similar results as in the single path case, as opposed to the downtown San Francisco area multipath case where the gain is significantly higher.

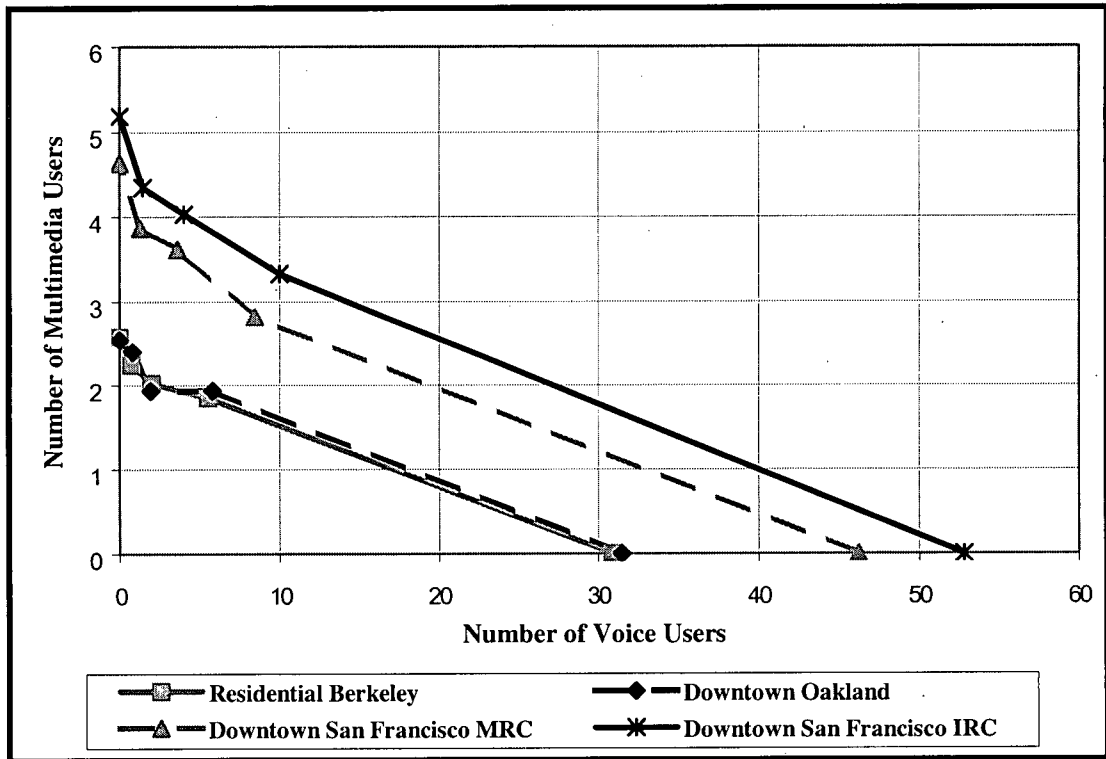


Figure 6.11 Simulation Results from Tables 6.8, 6.9, 6.11 and 6.13 with Different Traffic Mixes, Presented as Multimedia VS Voice Users Per Cell

6.5 Further Discussions and Comparisons with Other Publications

In this section, the simulation results for multipaths presented in Section 6.4 will be further discussed and compared with the results in other publications. The results using the MRC smart antenna will be rationalized first and will be followed by discussions on the results for the IRC smart antenna.

The single path results presented in Section 6.3 are used as the reference point of system performance between various system configurations to determine the differences between the convolutional and turbo channel coding methods and the assorted numbers of antenna elements. The residential Berkeley and downtown Oakland multipath cases

can be referenced to the single path case due to their similarities. The results of these cases determine the system capacity for the two-element MRC antenna configuration to be around 31 to 36 users per cell for voice only traffic, and 3 to 6 users per cell for multimedia only traffic.

As a comparison to the IS-95 system, the simulation results in Chan [19] records uplink capacity to be between 42 to 56 users per cell for the all voice traffic scenario for the single path and the downtown Oakland environments of a IS-95 system with the four-element omnidirectional MRC antenna configuration. The MRC antennas in Chan are referred to as beamforming antennas. The result obtained in this thesis of the WCDMA system is 122 users per cell for the same antenna configuration, which is much larger than the result for the IS-95 system. The difference in capacities is mainly affected by the physical layer configurations of the two systems. One of the differences is that the transport channel encoder in the IS-95 uses the convolutional encoding scheme while the WCDMA result above is obtained using the turbo encoding scheme. Furthermore, the OVSF code and the scrambling code of the WCDMA system provide good performance as well. Another difference is the failure link percentage before saturation is set to 1% for the IS-95 system whereas in the WCDMA system it is set to 5% for voice users.

The WCDMA simulation performed by Jones and Owen [17], which uses multipath profiles having one strong component and other weak components, reports the result of 20 users per cell for the all voice traffic scenario for a system with a cell radius of 4 km. The results present in this thesis are much higher than the capacity given by Jones and Owen. This is largely due to two different simulation parameters. First, the system in

Jones and Owen is composed of 37 cell sites for a 4-tier configuration compared to 19 in the system in this thesis. As the number of cells increases, the inter-cell interferences would also rise which in turn decrease the system capacity. The second reason is that the voice activity factor in Jones and Owen is set to 66% compared to 50% in this thesis. Again, the increase in the voice activity factor generates more MAI and reduces the number of users that a cell could service.

In Lee and Arnott [47], for a WCDMA system with multipath power profiles and mixed traffic services, when the number of elements is doubled, the performance gain is at 180%. This value is consistent with the results obtained in Tables 6.5 and 6.8, ranging from 210% to 240%. The higher than expected gain comes from not only the increase in antenna elements but also the transport channel decoder capability.

The followings are comparisons between the results for the MRC and IRC smart antennas. By comparing the results between the MRC and IRC antennas for the downtown San Francisco case in Tables 6.11 and 6.13, the improvement of the IRC antenna over the MRC antenna is shown in Table 6.14. From Table 6.14, the improvement by the IRC antenna over the MRC antenna ranges between 13% and 14%. For the single path, residential Berkeley, and downtown Oakland cases, simulations using the IRC antennas have also been performed. The results for those cases, however, are very similar to the results for the MRC antennas under the same scenarios, within plus or minus five percentages of each other. Those IRC results are thus not included in the graphs or the summary tables so that the MRC results would be easier to read and identify. The only exception, as presented in Table 6.14, is the downtown San Francisco case.

Traffic Mix %	IRC Gain over MRC
<i>100% voice</i>	14%
<i>75% voice</i>	18%
<i>50% voice</i>	14%
<i>25% voice</i>	12%
<i>0% voice</i>	13%

Table 6.14 IRC Antenna Performance Gain over MRC Antenna

A comparison between MRC and IRC antennas can also be found in Lee and Arnott [47]. The improvement of the IRC antennas over the MRC ones presented in Lee and Arnott ranges from 16% to 84% depending on the antenna configurations. At a first look, the improvement in Lee and Arnott is much higher than the results obtained in this thesis. To investigate the reasons behind the difference, a more in depth look of the Lee and Arnott model is required. Lee and Arnott employ a multi-cell, two-component multipath model and assume perfect channel estimation at the BS. The MRC and IRC algorithms are calculated based on known steering vectors for each user. Thus the weights calculated for the MRC and IRC adjustments would be fairly effective and the performance of these two algorithms will be at their best.

In contrast, the calculation of the MRC and IRC weights in this thesis is based on the received signals and the pilot signals. Channel estimation is obtained from the modulation of the received signals and the pilot signals under interference. Therefore the estimated weights for MRC and IRC will not be the optimal weights to make the ideal adjustments. Furthermore, in order to calculate the IRC weight, it is necessary to first

compute the inverse of the spatial interference covariance matrix in Equation 4.22. To do so, considerable AWGN values must be present in the received signals in Equation 5.3, or otherwise the inverse of the covariance matrix would become singular and the accuracy of profiling the antenna pattern could be hampered. The MRC, on the other hand, does not require the presence of the AWGN values to be included in the received signals. The non-perfect channel estimation and the existence of the AWGN make the estimated IRC weights non-optimal. Thus the IRC results are less than optimal and limited to near MRC performance for the single path case and the residential Berkeley and downtown Oakland case where the improvement is within plus or minus five percent.

For the downtown San Francisco case presented in this thesis, the improvement of IRC antennas over MRC antennas is between 12 and 18 percent, which is close to the smallest gain of IRC presented by Lee and Arnott. The reason for the leap in IRC performance can be contributed to the power profiles for downtown San Francisco where the power is evenly distributed into the multipath components for each profile. Because the maximum beam direction is not always pointing at the AOA of the desired user, the multipath signals which arrive in the vicinity of the maximum beam will not deteriorate the overall signal reception, as the other multipath components are still strong enough for the receiver to decode signals. For this reason, the desired signals will not be overwhelmed by the interference and noise signals in this case and thus the better performance.

In Chiu [18], a comparison has been done between the MRC and IRC antennas, which are referred to as the beamforming and nullsteering antennas, for a IS-95 system using also the Hashemi's power profile model. Chiu has found that the capacity of the

IRC antenna has 9% gain over that of the MRC antenna for the downtown San Francisco case while the MRC antenna outperforms the IRC antenna for all the other multipath scenarios by 8% to 14%. The reason behind these results, which have a similar trend as the results presented in this thesis, is also due to the effects that AWGN and power profiles have on IRC antennas as explained by Chiu.

To probe the improvement of IRC over MRC further, the results from Tirola and Ylitalo [38] are also considered here. Tirola and Ylitalo employ a three-component multipath, mix traffic model. MRC and IRC weights are estimated based on the received signals and pilot signals under interference as in this thesis. The results they have obtained indicate 22% improvement for the two-element antenna, I_o / N_o at 3dB, AWGN at 0dB configuration where I_o / N_o is the total interference power with respect to the power spectral density of thermal noise. With the AWGN increased to 0.05dB, the improvement of IRC over MRC drops down to 10%. This reaffirms the effects of AWGN on IRC performance seen from the simulation results as discussed earlier.

6.6 Conclusions

In this chapter, the system capacity simulation results for the WCDMA system have been presented and compared with the results from other publications. The capacity results include both single path and multipath scenarios under various antenna configurations. The results indicate that increasing the number of multimedia traffic users would significantly reduce the system capacity as expected. They also show that the relationship between the number of antenna elements and the total number of users at capacity could be modeled by a linear function. Furthermore, the performance of the

IRC receiver, when compared to that of the MRC receiver, would yield significant improvements only for the multipath environment that has the user signal powers evenly distributed in each of the multipath components.

Chapter 7 CONCLUSIONS AND RECOMMENDATIONS

7.1 Conclusions

In this thesis, the WCDMA system capacity with mixed data traffics under various antenna techniques and channel conditions have been investigated. The major contributions of the thesis are summarized as follow.

7.1.1 Analysis of the MRC and IRC Smart Antennas Performances

We have implemented the IRC and MRC antennas in the software platform of a WCDMA uplink simulator in order to examine the performances of these two smart antennas. To make the results realistic, the weight vectors in the MRC and IRC algorithms are approximated from the pilot signals and the interference-distorted received signals instead of assuming perfect weight estimation.

We have also evaluated the performances of the MRC and IRC antennas in terms of the system capacities. Compared to the MRC antennas, the results have shown that the IRC antennas have little or no improvement under the single path channel environment, or under those multipath channel environments with only one strong and several other weak multipath components. The greatest improvement for the IRC antennas occurs when the multipath channel is consisted of several evenly strong multipath components. Thus, these results have suggested that it is commendable to implement the IRC antennas in densely populated areas where there are a lot of reflectors that will evenly distribute the transmitted power into several multipath power components at the receiving site, whereas the MRC antennas provide adequate performance in suburban or rural areas.

7.1.2 Investigation of the Mixed Data Traffic Scenarios

We have studied the effect of servicing both the voice traffic users and the multimedia traffic users in the system using the WCDMA simulator. Rather than using the conventional analytical approach, the physical layer of the simulator performs actual coding and decoding operations and thus allows the realistic modelling of users engaging in different types of activities. This is achieved with the utilization of the OVSF coding algorithms at the chip level. Based on this approach, the numbers of users that the WCDMA system could accommodate with varying percentages of the voice users and multimedia users have been obtained. The results have shown that the high multimedia traffic factor decreases the capacity severely. This is due to the fact that the high speed data service, transmitting at a much higher power to compensate for the low PG, could cause significant interference to the low rate voice service.

We have also investigated the performances of the turbo codes against the convolutional codes, both of which are listed as the possible coding mechanisms for the transport network layer in the 3GPP specifications. While the turbo codes have shown superior results over the convolutional codes for the voice and multimedia users under different percentage mixes, the improvement is minimal for the voice only traffic scenario. This is due to the facts that the voice only traffic group would have a relatively small slot size compared to that of the multimedia traffic group, and that the turbo codes perform best over large sized data. Therefore, it can be concluded that the turbo codes, which require more complex encoders and decoders, would have the best efficiency when used for the multimedia traffic in the WCDMA system.

7.1.3 System Capacity Analysis and Comparisons

We have obtained the WCDMA system capacity results with the WCDMA simulator under different geographical environments. These environments are characterized by the varying power distributions in the multipath components generated using the Hashemi model based on Hashemi's empirical study. As opposed to the equal gain approach or the fixed power distribution for the user power profiles, the results obtained in this thesis reflect the effects of different types of urban environments on the system capacities. Furthermore, we have also presented the capacity results for various numbers of antenna elements and Rake fingers and compared their respective improvements.

In addition, we have designed the WCDMA simulator with modules that closely emulate the real world situation. The 19-cell system layout model is defined to include the effects of interference signals from neighbouring cells. The power control model that includes the open loop and closed loop power controls first estimates the transmitted power at the pre-run setup stage and adjusts the transmitted power at run time. The call admission control and system loading algorithms are implemented to monitor the number of users in the system based on the BER performance. All of these models are considered in the simulator in order to produce precise system capacities, which are very important in the 3G radio network planning.

7.2 Recommendations for Further Work

Although the first ever 3GPP compliant WCDMA end-to-end voice call has already been successfully made in late 2001 in a commercial 3G network, there are many areas in 3G that have yet to be explored. The followings are some suggestions for future

research that can be probed further.

Softer and Soft Handover Design in WCDMA

We have assumed that each user is served by only one BS with the strongest signal at the time of the initial subscription process. Realistically, due to the fact that MS's will traverse between sectors and cells, softer and soft handovers often take place. Softer handover occurs when a MS is in the overlapping coverage area of two adjacent sectors of a BS, and is receiving and sending two sets of signals from and to the BS whereas soft handover is defined by the same scenario but with two sectors that belong to two different BS's [20]. Challenges arise in handover algorithm designs and parameter settings in order to keep the handover probability below the desired value. Due to the fact that the extra set of signals will increase interferences in the received signals and consume the system resources, it is important to keep the handover overhead below a desired threshold.

Improved Antenna Model in the 3D Space

In this thesis, we have presented the WCDMA simulator implemented with an antenna model that is limited to the 2D plane. A more realistic model would involve the 3D space. One of the major concerns in the 3D antenna modelling is to determine the optimum antenna tilt based on the installed antenna height. The advantages of down tilting the antennas at an angle include reducing the inter-cell interference and focusing most of the transmitting power to the areas intended [16]. However, tilting the antennas too much will limit the areas that BS's can serve. Investigating the 3D aspects of the antennas is a promising project that can be added on top of the WCDMA simulator to

obtain realistic capacity results that are important for BS's installations.

Packet Data Performance and Control

We have assumed circuit-switched connections and considered only the physical and transport network layers of the WCDMA system in this research. The non-real-time packet data services, controlled by the higher layers, are also included in the 3GPP specifications. It is important to monitor the packet-switched data performance to ensure the QOS. One of the issues concerning packet transmissions is packet scheduling, which can be done in a code or time division manner. Another concern would be the configuration of the Automatic Repeat Request (ARQ) protocol where the sender makes decisions whether to send the packets at once or to defer the transaction until a later time [20]. It would be an interesting project to give an in depth look of these two issues with the goal of maximizing the system throughput.

Wideband Orthogonal Frequency Division Multiplexing (W-OFDM) in Next Generation Wireless Systems

In this thesis, we have discussed the use of OVSF codes in a multi-channel scenario in the WCDMA system. As the 3G WCDMA systems are being deployed in markets worldwide, the notions of a 4th Generation (4G) wireless system utilizing the OFDM technology are being drafted. OFDM, a form of multi-carrier modulation, works by dividing the total available bandwidth into several smaller sub-carriers spaced in such a way that the signals modulated at one sub-carrier will be zero when demodulated by the other sub-carriers. The advantages of using OFDM include minimized adjacent network interference, increased bandwidth allocation efficiency, and reduced susceptibility to

fading and multipath delays [6]. Therefore, it is essential to develop algorithms that will optimize frequency band assignments based on OFDM in the 4G systems.

Bibliography

- [1] M. W. Oliphant, "Radio Interfaces Make the Difference in 3G Cellular Systems," *IEEE Spectrum*, Vol. 37, Issue 10, pp. 53-58, October 2000.
- [2] G. Tsoulos *et al.*, "Wireless Personal Communications for the 21st Century: European Technological Advances in Adaptive Antennas," *IEEE Communications Magazine*, Vol. 35, Issue 9, pp. 102-109, September 1997.
- [3] J. S. Thompson *et al.*, "Smart Antenna Arrays for CDMA Systems," *IEEE Personal Communications*, Vol. 3, Issue 5, pp. 16-25, October 1996.
- [4] T. S. Rappaport, *Wireless Communications*, Prentice Hall 1996.
- [5] E. Dahlman *et al.*, "WCDMA – The Radio Interface for Future Mobile Multimedia Communications," *IEEE Transactions on Vehicular Technology*, Vol. 47, No. 4, November 1998.
- [6] L. B. Milstein, "Wideband Code Division Multiple Access," *IEEE Journal on Selected Areas in Communications*, Vol. 18, No. 8, pp. 1344-1354, August 2000.
- [7] P. Pirinen, "Conditional Outage Probability Evaluation in WCDMA at High Data Rates," *IEEE 6th International Symposium on Spread-Spectrum Tech. & Applications*, Vol. 1, pp. 230-234, September 2000.
- [8] T. Neubauer and E. Bonek, "Increasing Mixed Service Uplink Capacity of UMTS by Smart Antennas," *Journal of Communications and Networks*, Vol. 2, No. 4, pp. 331-336, December 2000.
- [9] R. Kohno, "Spatial and Temporal Communication Theory Using Adaptive Antenna Array," *IEEE Personal Communications*, Vol. 5, Issue 1, pp. 28-35, February 1998.
- [10] K. J. Quirk and L. B. Milstein, "The Effect of Low SNR in Phase Estimation in Wideband CDMA," *IEEE Journal on Selected Areas in Communications*, Vol. 19, No. 1, pp. 107-120, January 2001.
- [11] H. Hashemi, "A Statistic Model for Urban Radio Propagation," *IEEE Transaction on Communications*, Vol. 25, No. 7, July 1977.
- [12] J. Li *et al.*, "Computationally Efficient Angle Estimation for Signals with Known Waveforms," *IEEE Transactions on Signal Processing*, Vol. 43, No. 9, pp.

2154-2163, September 1995.

- [13] P. Muszynski, "Interference Rejection Rake-combining for WCDMA," *Proceedings of the Wireless Personal Multimedia Communications 1998 WPMC'98*, Japan, November 1998.
- [14] E. Tirola and J. Ylitalo, "Optimum Combining for Coherent Multisensor Receivers," *Proceedings of IST Mobile Communications Summit 2000*, pp. 365-370, Ireland, 2000.
- [15] H. Pinto *et al.*, "Uplink Capacity of the WCDMA FDD Mode in UMTS Networks for Mixed Services," *IEEE 52nd Vehicular Technology Conference 2000*, Vol. 6, pp. 2617-2624, Fall 2000.
- [16] J. Laiho-Steffens *et al.*, "The Impact of the Subscriber Profile on WCDMA Radio Network Performance," *IEEE 50th Vehicular Technology Conference 1999*, Vol. 5, pp. 2490-2494, Fall 1999.
- [17] P. Jones and R. Owen, "Sensitivity of UMTS FDD System Capacity and Coverage to Model Parameters," *1st International Conference on 3G Mobile Comm. Technologies*, pp. 224-229, March 2000.
- [18] D. S. Chiu, "Capacity Improvements Using Adaptive Nullsteering Antennas in IS-95 Cellular CDMA Systems," M. A. Sc. Thesis. The University of British Columbia, Vancouver, BC, Canada.
- [19] K. H. Chan, "Capacity Improvements Using Beamforming Antennas in IS-95 Cellular CDMA Systems," M. A. Sc. Thesis. The University of British Columbia, Vancouver, BC, Canada.
- [20] H. Holma and A. Toskala, *WCDMA for UMTS Radio Access for Third Generation Mobile Communications*, John Wiley & Sons, 2000.
- [21] S. H. Kim *et al.*, "A Hybrid Multi-rate Scheme for WCDMA," *Proceedings of the IEEE Region 10 Conference TENCON'99*, pp. 1224-1227, March 1999.
- [22] 3GPP Technical Specifications, "Physical Channels and Mapping of Transport Channels onto Physical Channels (FDD), Multiplexing and Channel Coding (FDD), Spreading and Modulation(FDD)," *3GPP TS 25.211-213 v3.5.0*, December 2000.
- [23] M. Guenach and L. Vandendorpe, "Performance Analysis of Joint EM/SAGE

- Estimation and Multistage Detection in UTRA-WCDMA Uplink," *IEEE International Conference on Communications 2000 ICC 2000*, Vol. 2, pp. 638-640, June 2000.
- [24] A. J. Viterbi, *CDMA – Principles of Spread Spectrum Communication*, Addison Wesley, 1995.
- [25] R. H. Morelos-Zaragoza, *The Art of Error Correcting Coding*, John Wiley & Sons, 2002.
- [26] O. Acikel and W. Ryan, "High Rate Turbo Codes for BPSK/QPSK Channels," *Proceedings of International Conference on Communications 1998*, Vol. 1, pp. 422-427, June 1998.
- [27] L. Bahl *et al.*, "Optimal Decoding of Linear Codes for Minimizing Symbol Error Rate," *IEEE Transaction Information Theory*, pp. 284-287, March 1974.
- [28] S. Akhtar and D. Zeghlache, "Capacity Evaluation of the UTRA WCDMA Interface," *IEEE 50th Vehicular Technology Conference 1999*, Vol. 2, pp. 914-918, Fall 1999.
- [29] R. Cheng and P. Lin, "OVSF Code Channel Assignment for IMT-2000," *IEEE 51st Vehicular Technology Conference 2000*, Vol. 3, pp. 2188-2192, Spring 2000.
- [30] F. Adachi *et al.*, "Tree-structured Generation of Orthogonal Spreading Codes with Different Lengths for Forward Link of DS-CDMA Mobile Radio," *Electronic Letters*, Vol. 33, No. 1, pp. 27-28, January 1997.
- [31] T. Minn and K. Y. Siu, "Dynamic Assignment of Orthogonal Variable-Spreading-Factor Codes in W-CDMA," *IEEE Journal on Selected Areas in Communications*, Vol. 18, No. 8, pp. 1429-1440, August 2000.
- [32] B. Engstrom and M. Ericson, "WCDMA System Level Performance with Fast Fading and Non-Ideal Power Control," *IEEE 50th Vehicular Technology Conference 1999*, Vol. 2, pp. 1129-1133, Fall 1999.
- [33] K. Hooli *et al.*, "Inter-path Interference Suppression in WCDMA Systems with Low Spreading Factors," *IEEE 50th Vehicular Technology Conference 1999*, Vol. 1, pp. 421-425, Fall 1999.
- [34] J. Wang and J. Chen, "Performance of Wideband CDMA Systems with Complex

- Spreading and Imperfect Channel Estimation," *IEEE Journal on Selected Areas in Communications*, Vol. 19, No. 1, pp. 152-163, January 2001.
- [35] S. Haykin, *Communication Systems*, John Wiley & Sons, 1994.
- [36] J. G. Proakis, *Digital Communications*, McGraw-Hill, 1995.
- [37] T. Haynes, *A Primer on Digital Beamforming*, Spectrum Signal Processing, 1998.
- [38] E. Tirola and J. Ylitalo, "Performance of Smart Antenna Receivers in WCDMA Uplink with Spatially Coloured Interference," *Proceedings of IST Mobile Communications Summit 2001*, Spain, September 2001.
- [39] S. Akhtar and D. Zeghlache, "CIR Based Soft Handover for UTRA FDD Uplink," *The 11th IEEE International Symposium on PIMRC*, Vol. 1, pp. 650-654, September 2000.
- [40] H. Holma *et al.*, "Simulated and Measured WCDMA Uplink Performance," *IEEE 54th Vehicular Technology Conference 2001*, Vol. 2, pp. 1148-1152, Fall 2001.
- [41] R. Hoppe *et al.*, "Fast Planning of Efficient WCDMA Radio Networks," *IEEE 54th Vehicular Technology Conference 2001*, Vol. 4, pp. 2721-2725, Fall 2001.
- [42] R. J. Piechocki *et al.*, "Orthogonal Re-spread for Uplink WCDMA Beamforming," *IEEE 51st Vehicular Technology Conference 2000*, Vol. 2, pp. 1373-1376, Spring 2000.
- [43] D. Y. Ahn and R. Tafazolli, "Interference Characteristics Analysis of Mixed Services in Wideband CDMA UMTS," *1st International Conference on 3G Mobile Comm. Technologies*, pp. 60-64, March 2000.
- [44] M. G. Kyeong and J. J. Park, "3G-class Space-time Array Transceiver for High Data Rate Service WCDMA Smart Antenna System," *IEEE International Conference on Communications 2000 ICC 2000*, Vol. 2, pp. 1025-1029, June 2000.
- [45] J. Laiho-Steffens *et al.*, "Verification of 3G Radio Network Dimensioning Rules with Static Network Simulations," *IEEE 51st Vehicular Technology Conference 2000*, Vol. 1, pp. 478-482, Spring 2000.
- [46] H. Fu and J. S. Thompson, "Downlink Capacity Analysis in 3GPP WCDMA Networks System," *3rd International Conference on 3G Mobile Comm. Technologies*, pp. 534-538, May 2002.

- [47] J. Lee and R. Arnott, "System Performance of Multi-sector Smart Antenna Base Stations for WCDMA," *2nd International Conference on 3G Mobile Comm. Technologies*, pp. 1-6, March 2001.
- [48] W. U. Pistelli and R. Verdone, "Downlink Capacity for WCDMA with Soft and Softer Handover; Advantages of Unbalanced Received Powers," *5th International Symposium on Wireless Personal Multimedia Communications*, Vol. 1, pp. 77-81, October 2002.
- [49] R. B. Ertel *et al.*, "Overview of Spatial Channel Models for Antenna Array Communication Systems," *IEEE Personal Communications*, Vol. 5. Issue 1, pp. 10-22, February 1998.